FeS_2 thin film photoelectrodes from nanostructured colloidal precursors

Graeme O'Dowd

Stephenson Institute for Renewable Energy

Department of Physics

September 2018

Thesis submitted in accordance with the requirements of the University of Liverpool for the degree of Doctor in Philosophy.

Ach, people're always telling us no' tae do things,' said Rob Anybody. 'That's how we ken what's the most interestin' things tae do!

- Terry Pratchett

Table of Contents

Abstract

Due to the overuse of fossil fuels, there has been a steady build-up of greenhouse gasses within the atmosphere. In recent years, however, we have begun to see the negative effects of this, which has led to a need to move towards carbon-neutral or renewable energy production methods, such as solar power. Earth-abundant materials with slightly reduced efficiencies can be a more cost-effective way to generate power, using sunlight, than expensive high-efficiency materials. An example of this type of material is FeS_2, however, before FeS_2 can be a viable photocathode material, three main problems need to be overcome; its instability in water, high density of defect states and a conduction band minimum below the reduction potential of H_2O.

As such this thesis aimed to firstly overcome the problem of FeS_2s conduction band minimum being below the potential of H_2O. To do this, a synthetic method capable of creating quantum-confined FeS_2 nanoparticles was developed, to increase the material's bandgap. By developing and implementing an inverse micelle synthesis FeS_2 nanoparticles, 3.5nm in diameter and with a bandgap of 1.5 eV, were created. This thesis also addressed FeS_2s high density of defect states. To overcome this problem, we investigated annealing the electrodes in different atmospheric environments. Here we found that electrodes annealed in Hydrogen and Nitrogen showed reductions in Sulphur dangling bonds, and those annealed in Sulphur showed a complete removal of any defect states. Furthermore, we aimed to increase the stability of FeS_2 in aqueous environments using deposition of protective over-layers. We found that using a 3mn protective over-layer of TiO_2 with a Pt co-catalyst increased the stability of FeS_2 significantly, with the electrode lifetime increasing from minutes up to more than three hours. These electrodes also had a solar-to-hydrogen conversion efficiency of 0.06%.

Overall, the results of this thesis show it is possible to increase FeS_2s stability in aqueous environments, with protective overlayers, and FeS_2s defect states can be repaired with post-synthetic treatments. The synthesised quantum-confined nanoparticles have a bandgap that corresponds to a theoretical efficiency of approximately 60%. However, further work is needed to combine the effects of Sulphur annealing and protective over-layers with the FeS_2 quantum dots.

Acknowledgements

Dr. Frank Jaeckel

Dr. Yvonne Grunder

Dr. Wei Li

Dr. J

I would like to thank Mr Jack, my GCSE Physics teacher, you inspired me to follow a path that led to pursuing this PhD, and I'm not sure I will ever forgive you. What got me through was routine Friday, and possibly some midweek trips to AJ's, the last decent place in Liverpool to quench the ''research thirst'' with only a £20 note. As well as the endless number of coffee breaks with Joseph Horne and helpful discussions from him and Nicole Fleck. I would also like to take this opportunity to plead with Joe on Nicole's behalf ''*Joe, mate, please stop singing unbearably catchy tunes in the lab!!!!!*'' The 'Stevy'(SIRE) had some wonderful people to socialise and science with: Thomas Whittles, Jack Swallows, Oliver Hutter, Phillip Murgatroid and Josh Fogg to name but a few. I'm not sure I could have picked a better place to do a PhD.

I would especially like to thank my family, particularly my Mum, for their unwavering support. Oh, on a side note I would also like to thank Megan Hasoon, I'm not sure what she does to help me, but she tells me it's a lot sooo… seriously though I doubt you would be reading this without her support.

List of Figures

1 Introduction

The purpose of this chapter is to introduce the overall motivation and background of the research presented in this thesis. The overall scope of this thesis is to contribute to the understanding of FeS_2 as a photoelectrochemical material for solar water splitting. As such, this introduction discusses where solar fuels research lies in the search for a potential renewable energy candidate and where the current understanding of FeS_2 sits within this field. Additionally, underlying motivations driving the research of photocathodes for solar fuel systems, in general, will also be discussed.

1.1 The energy crisis

Since the industrial revolution, fossil fuels to power energy production have steadily become one of the most important resources in the world. They are necessary for every part of a society of scale to function, and the current trend shows demand on energy production will only increase [1]. Current methods of energy production rely heavily on fossil fuels. Two main problems are starting to surface with regards to this energy production model. The first of these are geopolitical issues. Often new sources and/or current sources of fossil fuels are found in politically unstable regions. This problem only stands to become more significant due to dwindling fossil fuel supplies. The second problem is the environmental issues surrounding fossil fuels. Data collected from ice core samples and recorded average global temperatures have shown atmospheric CO_2 content and global temperatures are increasing[2]. Increasing levels of CO_2 in the atmosphere is a natural cyclical process; however, this cycles timeline has been substantially expedited by a heavy dependence on fossil fuels. Current CO_2 levels in the atmosphere have even surpassed that of levels seen in previous ice age cycles[3].

Energy production via fossil fuels has begun to be supplemented by contributions from nuclear energy. Since the 1950s the use of nuclear fission as a power production source has steadily increased around the world[4]. The main benefit of nuclear power production is its high energy density compared to coal[5]. However, the introduction of nuclear power stations is often met with a negative public opinion due to associated safety risks. Additionally, although more sustainable than coal, nuclear power production still utilises a consumable resource, Uranium[6], [7]. Another nuclear energy candidate is nuclear fusion, where two or more atoms are combined to form a different atom releasing heat energy in the process. Research on nuclear fusion is currently focused on a reaction combining Deuterium with Tritium releasing approximately 17.6 MeV of energy[8]. Whilst nuclear fusion would theoretically be one of the best solutions to the energy crisis[9], this is still an underdeveloped solution[10].

Given the above problems with nuclear power, renewable energy sources are often looked towards as the more desirable alternative to coal for the near future. Currently, the main candidates for development and implementation are hydropower, wind, and solar. In the first quarter (Q1) of 2018, renewable energy sources were responsible for 30.1% of total electricity production in the UK, up 3.1% from the previous year. The fastest growing renewable source in the UK is wind, with total percentage energy production due to solar photovoltaics(PV) and hydropower decreasing[11]. Globally the trend is comparable; as of 2015 wind power contributed to over half of the total renewable energy production in the world (Figure 1-1(A))[12]. Although globally we are seeing a shift towards more renewable sources, the increase in wind power is likely due to the fact it is a more developed and easily implemented process, rather than it being the ideal energy source. In relation to the current three main renewable energy sources, hydropower, wind and solar, solar would be the superior candidate of the three due to having the highest amount of theoretical extractable energy[13].

A

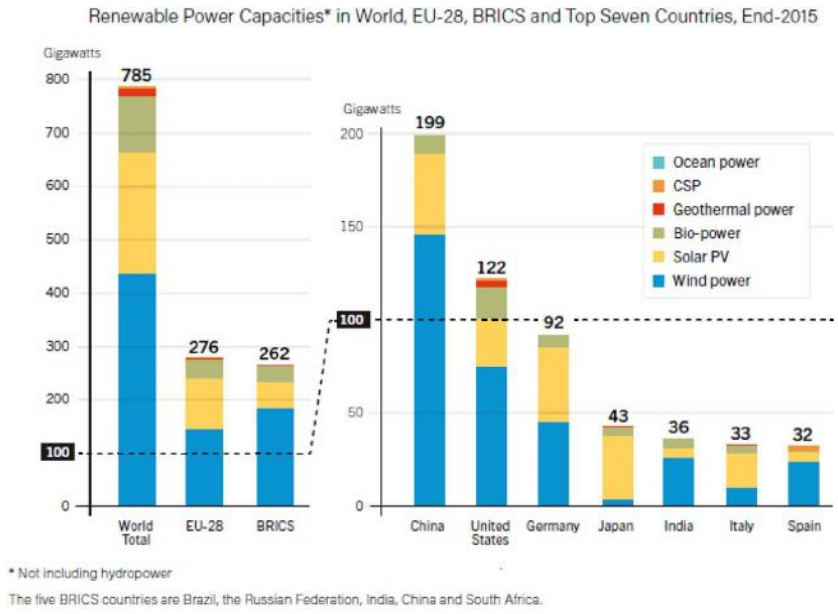

B

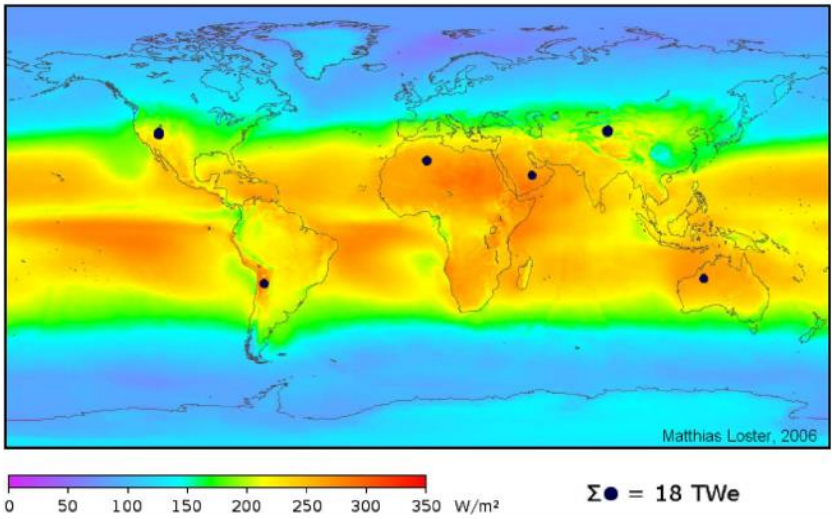

Figure 1-1(A) Comparison of renewable energy capacities in the world and the big seven countries (B) annual average solar irradiance[12]

1.2 Solar energy

Solar energy is a broad term defining any energy produced by capturing heat or light from the sun. The energy produced from solar heat energy is called solar thermal and that produced from light can be either solar photovoltaic(PV) or solar fuels. Compared to all other

renewable energy options solar energy has the greatest potential. To compare different forms of renewable energy to each other, total theoretical extractable energies can be converted to W_c. This is the theoretical power of each energy source multiplied by the efficiency of conversion to Hydrogen via water electrolysis. Current technology would allow for a total theoretical extractable energy of $250TW_c$ and $3.5TW_c$ for wind and hydropower, respectively[13]. The theoretical extractable potential of solar PV, solar fuels and solar thermal are $58\,000TW_c$, $61\,000TW_c$ and $19\,000TW_c$, respectively[13]. The highest theoretical extractible potential for a non-solar renewable energy source is wind, at $14TW_c$. Extractable energy calculations do not include having energy harvesting structures in inhospitable areas of the earth. From these values, the most obvious conclusion to draw is that solar power is the most abundant renewable power source. Figure 1-1(B) shows the average solar irradiance distribution across Earth. There are hot spots where the solar irradiance is at its maximum, but there are also points at varying longitudes and latitudes where the immediate world energy consumption could be satisfied at one location[12], shown by the black spots in Figure 1-1(B). Meeting the total energy requirements in the highlighted regions could be accomplished with a solar energy conversion system with an efficiency as low as 8%[12].

Unfortunately, solar energy has its problems, primarily intermittency, both seasonal and daily. A solution to this problem would be the use of batteries to store excess energy generated during daylight hours and in the summer months, to be used throughout times of low power generation. While the use of solar PV cells coupled to batteries would be suitable for stationary structures, such as buildings and street lamps, currently they are not fit for purpose for powering vehicles. This is because the power output of a solar panel is not enough to power a car. Ranges on battery cars are currently much less than that of fossil fuel powered cars and charge times are on the order of hours[14]. However, some circumstances are suitable for battery powered vehicles, such as for mid-range commutes. A potential solution to the problem of intermittency with solar energy could also be the use of solar fuels

instead of batteries. Solar fuels would store electrical energy in the form of a chemical bond; harnessing solar energy to power energetically ''uphill'' reactions e.g. water splitting into H_2 and O_2[15] or CO_2 into methanol[16] and into longer chain hydrocarbons[17]. These fuels can then be burnt to produce energy in the case of H_2 could also be used in a hydrogen fuel cell both of which are carbon-neutral energy sources. The benefit of solar fuels is that they are suitable for powering both stationary structures and vehicles. Even if driving ranges were diminished via the use of solar fuels, the refilling times would still be much lower[18].

Out of the three solar conversion systems available, the one that has the highest theoretical extractable energy potential and flexibility is solar fuels. The reason for the increase compared to solar PV is the fact that the solar fuels process directly converts solar energy into a chemical fuel. This reduces the number of steps between energy harvesting and chemical power, thus reducing the number of losses that occur due to energy conversions that are less than 100% efficient. As solar fuels are the most abundant energy option, it is within this context that this thesis develops FeS_2, as a solar energy absorber.

There are many architectures of solar fuel generators [19], however, all of the different types can be grouped into three main categories; particulate catalysis, photoelectrochemical cells and photovoltaic-biased cells[19]. In particulate catalysis systems, nanoparticles functionalised by ligand shells are suspended in relevant electrolyte solutions. For example, if water splitting is the goal, the particle would be suspended in water. The energy required to drive the electrochemical reaction at the nanoparticles interface is provided by the light absorbed by the particle. In the majority of cases, co-catalysts are deposited on the surface of the nanoparticles to increase activity[20][21]–[23]. Whilst systems like this provide an excellent “reactive” surface to volume ratio, there are some downsides. Firstly, unlike the following archetypes, it is not possible to apply an external bias, therefore the light-absorbing materials must have a conduction or valence band in the appropriate position to drive the

electrochemical reaction. It is also difficult to separate the reaction products as they would be produced within the same reaction vessel, potentially resulting in unwanted backwards reactions. Additionally, it is difficult to measure the photocurrent of individual nanoparticles to study the photoconductivity. Such particulate systems, however, could be more cost-effective than their electrode-based counterparts, due to the less complex engineering solutions available to particulate systems [24].

Photoelectrochemical(PEC) cells utilise a photocathode and an anode or a photoanode and a cathode, or a cell where both are photoactive. The two electrodes are electrically linked and the photogenerated bias is used to drive an electrochemical reaction at the surface of both electrodes. Semiconductors used in this situation can be monitored much more easily than in a particulate system. The photocurrents of electrodes can be monitored easily in classic three-electrode configuration systems; for example, where the photocathode/photoanode is the working electrode, Platinum(Pt) is a counter electrode and an Ag/AgCl electrode acts as a reference. The advantages of this situation are, that the conduction and valence band minimum and maximum, and hence driving force of a reaction, can be altered with an electrically applied bias[25]–[28]. The physics of this solid/liquid interface are discussed in Chapter 2 of this thesis. Another advantage is that the products from the two sides of the desired solar fuel reaction can be easily physically separated. Some of the challenges include difficulty researching stable photocathodes for the Hydrogen Evolution Reaction (HER) side of the photoelectrochemical reaction. A well-positioned conduction and valence band edge is also important. Whilst PEC cells allow for an applied bias to shift an energetically misaligned band edge, this decreases the overall energy gained by the cell. There is a subdivision of this type of cell which produces electricity and not fuel, which can be referred to as a regenerative photoelectrochemical cell (RPC). The RPC is so-called because in the majority of systems, species oxidised at the anodes surface diffuse

towards the cathodes surface where they are reduced and subsequently diffused back towards the anode and re-oxidised in a cycle [29].

The third archetype is the photovoltaic biased cell, utilising a classical PV cell to provide the electrical bias to drive an electrochemical reaction on a catalysts surface. The advantage of this solar fuel production cell is that it incorporates an already mature field that is able to produce a cell capable of highly efficient solar to energy conversion. However, the challenge is gaining an increase in the energy stored from a PV cell operating in these conditions as compared to a cell operating under standard conditions. The work researched within this thesis incorporates FeS_2 electrodes within the photoelectrochemical cell branch of solar fuel generators.

1.3 Solar fuels with a focus on water reduction/oxidation

As discussed previously, there are a number of types of solar fuel reactions, which can be driven photoelectrochemically. As this thesis concentrates on Hydrogen production, the following review of solar fuels literature will concentrate on water reduction/oxidation. The first report of a water-splitting reaction driven by the absorption of a photon was published in 1972 by Fujishima and Honda[30]. A TiO_2 photocathode connected to a Pt electrode was irradiated under UV light by a Xenon lamp and Oxygen and Hydrogen evolution was measured with a mass spectrometer. The quantum efficiency of the reaction was estimated to be around 10%. The next major publication came in the early 1990s, published by O'Regan and Gratzel[31]. The paper demonstrated a low-cost dye-sensitised TiO_2 film with a solar-to-hydrogen (STH) conversion efficiency of 12% under diffuse daylight conditions. These publications highlighted two main branches of harvesting solar energy using photoelectrochemical cells. The first, focusing on producing solar fuels using the absorbed light energy and the second focusing on electricity generation (regenerative cell).

Research on the photoelectrochemical production of solar fuels from water oxidation/reduction either focuses on an overall water splitting cell or one half of the reaction. The half-reactions studied are either reduction at a photocathodes surface[32] or oxidation at the photoanode surface[33]. Common photoanodes for the oxidation of water are TiO_2[34], WO_3[35], $BiVO_4$[36] and Fe_2O_3[37]. Whilst there are disadvantages to these materials, for example, Fe_2O_3s small hole diffusion length of 2-4nm[38], they are stable under operating conditions. With earth abundant photocathodes, however, the list is more limited as they are often very unstable when in contact with water. A well-studied photocathode is Cu_2O[21], [39], [40], with a bandgap of 2eV and a conduction band minimum above the reduction potential of H_2O. With a theoretical STH conversion efficiency of 18%, the material would be ideal, if it were not for its instability due to photocathodic decomposition[15]. Other desirable photocathodes in the Cu family are Cu(In, Ga)Se_2 (CIGS)[41] and $CuZnSnS_4$ (CZTS)[42] representing an ability to tune the bandgap within the 1-1.7eV range. These Cu based electrodes have a large absorption coefficient allowing for small amounts of the materials to be used[43]. This is an important characteristic as some of the components of the materials are rare earth metals, for example, Indium, which is very expensive. Another promising photocathode is $CuBi_2O_4$ first identified in 2007, which has a bandgap of 1.6-1.8eV[44]. This material utilises relatively cheap materials and has a theoretical maximum photocurrent density of 19.7mAcm^{-2} corresponding to a maximum STH conversion efficiency of 24%. However, $CuBi_2O_4$ suffers from poor carrier diffusion kinetics and electron-hole recombination at surface states. Often it is necessary to reduce the thickness of the film to account for the poor carrier diffusion lengths, hence also reducing the maximum achievable photocurrent density. The maximum STH conversion efficiency achieved to date is 30% using a photovoltaic cell electrolyser, utilising a triple junction PV cell as the solar absorber[45]. However, the maximum achieved STH efficiency using a photoelectrochemical cell is 18.5% in neutral pH conditions[46]. This was done using a double buried junction of GaInP/GaInAs

coated with RuO and Rh co-catalysts and a TiO_2 overlayer protecting the photocathode. Table 1-1 summarises the key metrics of the photocathode materials discussed above, as well as other earth abundant materials not discussed in the text.

The photocathodes discussed here have been limited to materials which are classified as earth abundant. CIGS has been included as, even though it incorporates Indium into its structure, it is still relatively cheap to produce with respect to its potential energy output. The abundance and cost of materials is an important factor to be considered when investigating candidates for solar fuels applications. Expensive materials are often favoured as their increased efficiency reduces the cost per Kg of produced Hydrogen. However, the same could be achieved from a material which is very cheap but has a moderate efficiency. This is because the cost required to extract and produce earth abundant cathodes cannot be outweighed by increases in efficiency above 10%[47]. For example, if theoretical energy output vs. cost to extract materials is considered, FeS_2 which has a high theoretical energy output, would be one of the most desirable candidates, due to its extremely low costs.

Material	Photocurrent density (mA cm^{-2})	Efficiency (%)	Bias (vs. RHE)	Morphology	Ref
CIGS	18	12[b]	-0.6	Thin film	[48]
Cu_2O	7	2.5[a]	0.0	Thin film	[49]
	10	3[a]	0.0	Nanowire	[50]
$CuFeO_2$	2.4	-	-0.4	Thin film	[51]
$CuBiO_4$	1.55	-	-0.5	Nanotextured	[52]
CZTS	12.5	-	-0.6	Thin film	[53]
CZTS (Cd doped)	17	4[b]	0.00	Thin film	[54]
CZTS (Se doped)	37	7[b]	0.00	Thin film	[55]
CBTS (Se doped)	5	-	0.00	Thin film	[55]
	7.5	1.6[a]	0.00	Thin film	[56]
	12.08	0.58[a]	0.00	Thin film	[57]
SbSe	12.5	-	0.00	Nanowire	[58]
	14	-	0.00	Thin film	[59]
	8.6	-	-0.43	Thin film	[60]

Table 1-1 Summary of common earth materials along with key published metrics [a] efficiency calculated using the STH equation which accounts for faradaic efficiency, [b] efficiency calculated using the HC-STH equation which does not account for faradic efficiency. – represents unreported values.

Overall, the search for a material to act as a viable photocathode can be challenging. Materials currently available for photocathodes on photoelectrochemical cells have a lot of disadvantages in common. Many photocathode materials are unstable when in contact with a solution, and a large proportion have poor charge transport kinetics. In addition to this,

surface/bulk defect states can act as trap states for the majority carriers resulting in inefficient electron-hole separation and subsequent recombination. If a material does not have at least one of these characteristics it is usually comprised of either expensive or toxic materials, or both. The ideal material would be one which is comprised of earth-abundant, non-toxic materials but does not have any of the above disadvantages, however, a material like this is not known. With careful electrode design, however, it is possible to overcome the detrimental aspects of a photocathode material. An example of this would be to remove trap states with post-synthetic treatment[61], improving stability with passivating over-layers[62] and altering band alignments with doping[63][64] or quantum confinement.

1.4 Iron Pyrite as a photocathode

Iron Pyrite is a semiconducting material with a high absorption coefficient[70] comprised of earth-abundant materials[71] and has a bandgap of 0.95eV[72]. This combination of attributes should make FeS_2(P) a highly desirable material for solar energy applications. Figure 1-2 shows the bandgap of FeS_2 compared with some of the materials mentioned in Section 1.3.

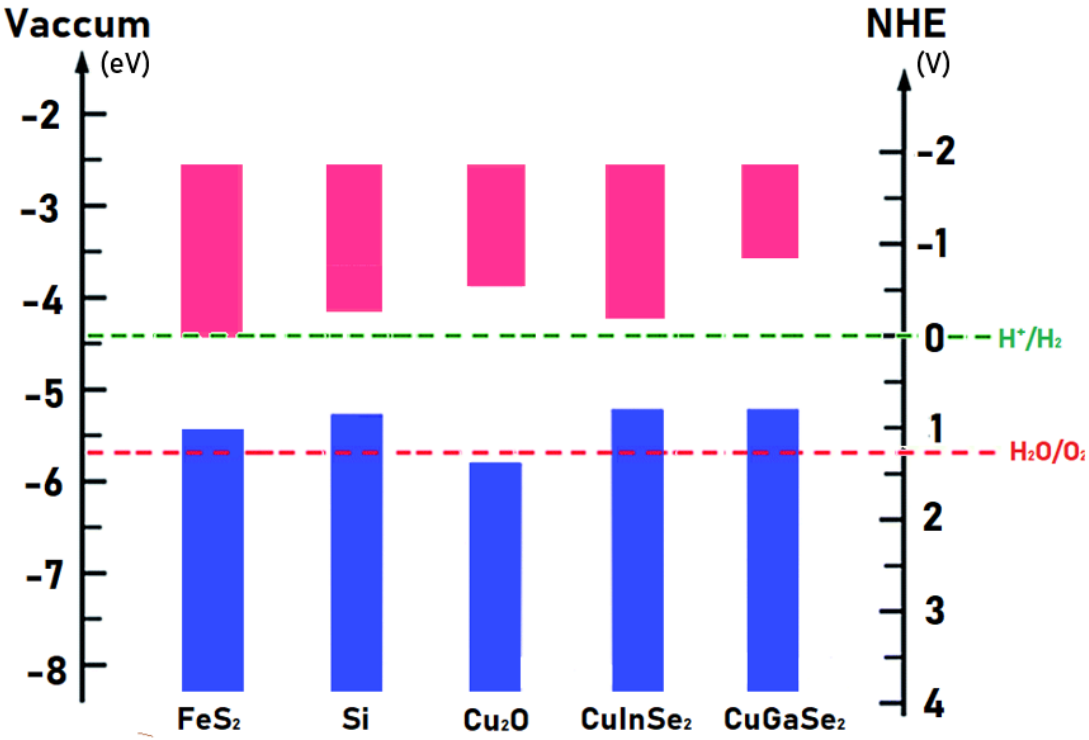

Figure 1-2 Bandgap of common earth abundant semiconducting photocathodes compared to FeS_2. Pink bars represent the conduction band and blue bars represent the valence band. The green and red dotted lines represent the potential of HER and OER reactions respectivley.

Figure 1-2 shows the bandgap of FeS_2 lies just below the redox potential for the HER compared to the other photocathode materials[73]. Due to this FeS_2will need an applied bias to drive the HER. A benefit of FeS_2s bandgap, however, is that it has the potential to absorb around 90% of the power from incident sunlight (at AM1.5). This is put in context in Figure 1-3. Figure 1-3A shows the spectrum of solar power incident upon a surface at ground level at AM1.5. Figure 1-3B shows the maximum extractable percentage of solar power as a function of bandgap with some overall solar water splitting materials as examples. A bandgap of 1.59eV corresponds to the ideal bandgap energy of a solar absorber as it represents the Gibbs free energy plus the overpotential required to drive overall water splitting reactions. While FeS_2 does not have this ideal bandgap, its 0.95eV bandgap means it can absorb 90% of

the power from the solar spectrum, and a theoretical maximum photocurrent density of 45mAcm^{-2} at 150nm film thickness[74].

Using the applied-bias photocurrent conversion efficiency, discussed in detail in Chapter 2, the theoretical maximum STH efficiency of FeS_2 would be 19.35% under the bias of 0.19V vs. Reversible Hydrogen Electrode (RHE). This is the bias used in this thesis. Mismatched band alignment can be corrected via quantum confinement, which is when the Bohr radius of the electron-hole pair (exciton) is confined spatially by the dimensions of the semiconducting material. As the dimensions of the crystal structure approach the Bohr radius this is the weakly confined regime, where the bandgap starts to widen. As the dimensions reduce

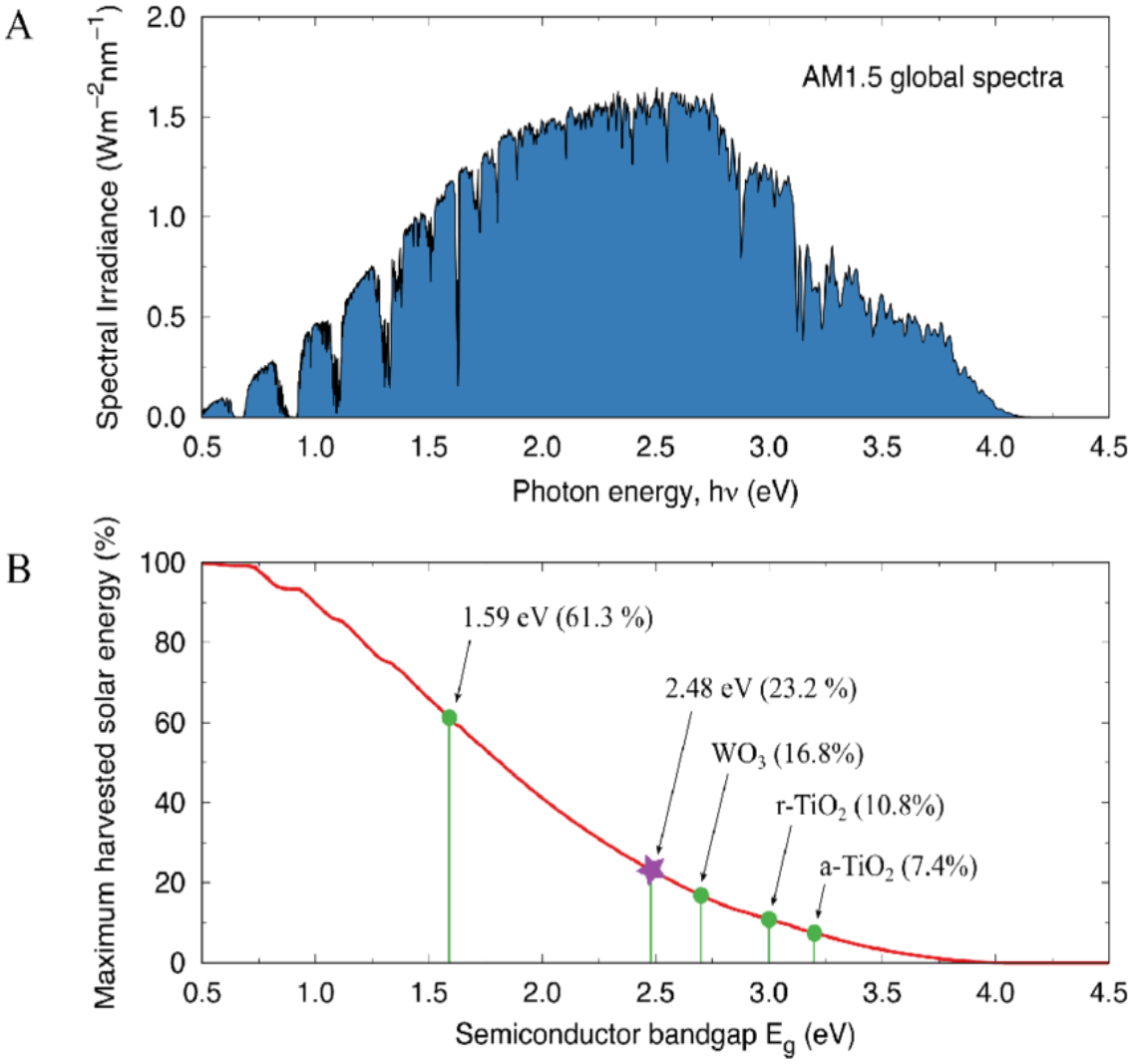

Figure 1-3 A) Solar spectrum at AM1.5 B) Theoretical maximum STH conversion efficiency plotted against bandgap. Image taken from [171]

below the exciton Bohr radius this is the strong confinement regime, where the majority of the bandgap widening takes place. Figures 1-4A and B show how the bandgap of FeS_2 varies with the dimension of a spherical particle[75]. As the diameter of the spherical particle decreases in size, the bandgap increases and the positions of the conduction band minimum and valence band maximum shift apart[76]. Figure 1-4B shows how the conduction band minimum and valence band maximum shift with respect to the potentials for water and Oxygen evolution for 6nm, 4nm and 3nm particles. An advantage of starting from a material with a lower bandgap is that the bandgap can be broadened to the desired amount. For example, a FeS_2 "spherical" particle with a 4nm diameter would have a conduction band minimum at a suitable potential to drive a HER. The bandgap of the particle would be 1.58eV which, if compared to Figure 1-3B, would correspond to a maximum theoretical conversion efficiency of approximately 61.3%. In FeS_2 the conduction band minimum varies much more than the valence band maximum due to the large difference between effective electron and hole masses.

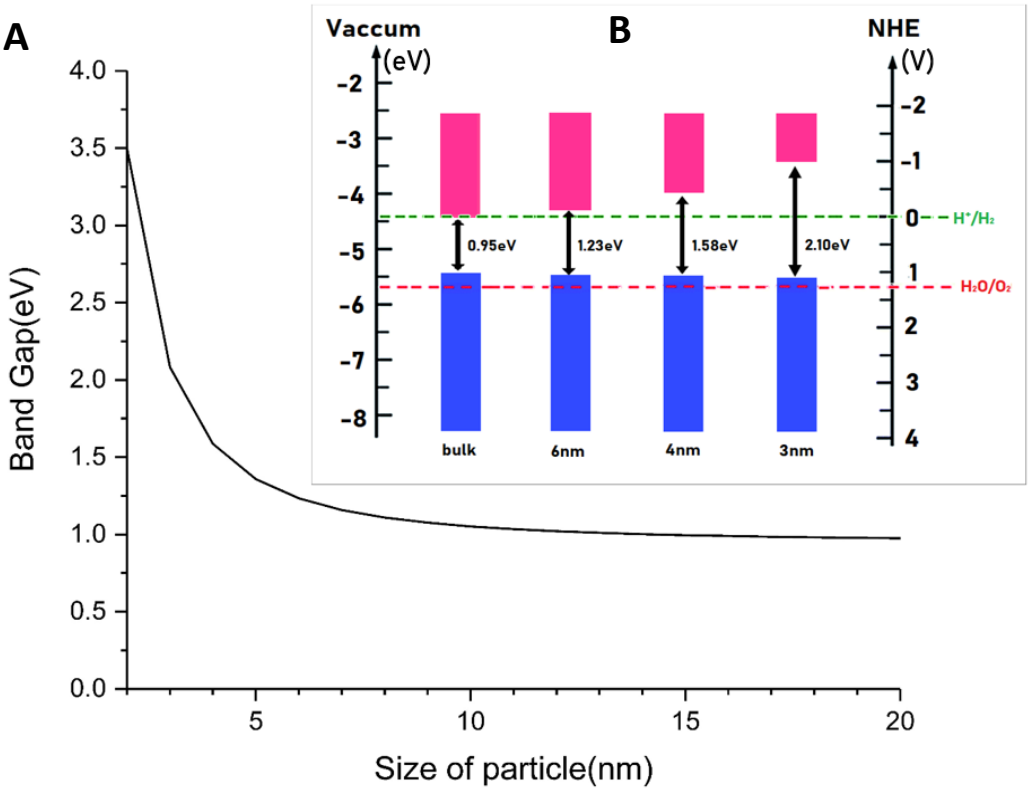

Figure 1-4 A) Theoretical bandgap of spherical Iron Pyrite particles versus diameter of the particle B) Bandgap of bulk like, 6nm, 4nm and 3nm Iron Pyrite nanoparticles. Red and green dotted lines represent the HRE and OER potentials respectively.

Further to its mismatched band alignment, FeS_2 is hindered by several crucial problems. Firstly, defect states within the bandgap act as hole traps [77] and become recombination centres for photoexcited electrons. Iron defects can also occur but result in energy states outside the bandgap[78]. The high density of sulphur defect states are predicted by ligand field theory to reside in a doubly degenerated state within the bandgap, approximately 0.2eV and 0.5eV below the conduction band minimum[79]. The energy of formation for Sulphur and Iron bulk point-like defect states ranges from 1.4 to 2.1 eV for Sulphur vacancies and from 0.3 to 1.7 eV for Iron vacancies[78]. These energies of formation are high enough that bulk point-like defects like these are unlikely to occur in huge concentrations. However, reduced co-ordination at termination sites on the surface of the crystal will cause a high

density of sulphur defect states on the surface. This will lead to a different electronic structure on the surface of Pyrite than would be present in the bulk structure.

Figure 1-5A shows a model of the topmost layers of an FeS_2 crystal lattice with predicted sulphur defect states. Figure 1-5B shows the Sulphur 2p region of an XPS spectrum with increasing take-off angle. Figure 1-5C shows XPS data from the Sulphur 2p region with different angles between the source and analyser [80]. Labels for the fitted peaks in the XPS spectrums of both Figure 1-5B and C correspond to the labels of the defect states in the model presented in Figure 1-5A. As the take-off angle and the angle between the source to the analyser is changed, the measurement becomes more surface sensitive and hence the signal from Sulphur bound to the surface becomes more prominent than Sulphur in the bulk. With this technique surface Sulphur dimers, under-coordinated Sulphur and bulk-like Sulphur atoms can be clearly distinguished.

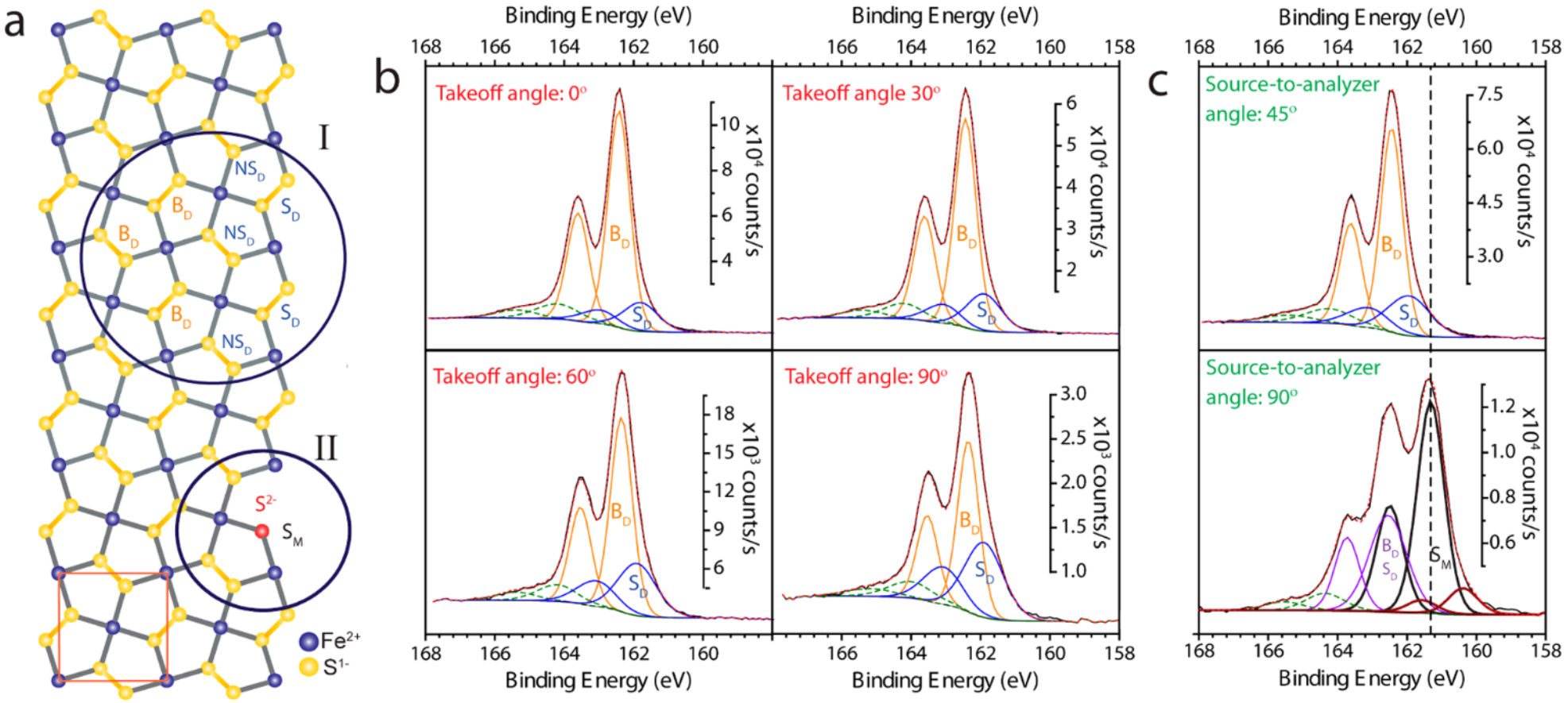

Figure 1-5 A) The simplified structure of Iron Pyrite showing the different types of sulphur bond present in the bulk and surface structure B) XPS data of FeS_2 100 crystal surfaces at different take-off angles C) XPS of FeS_2 100 single crystal surface at different source to analyser angles. Image taken from [80]

As well as impurity phases which can have different bandgaps and more metallic-like behaviour, Table 1-2 shows the two most prevalent phases of FeS_2 along with the corresponding bandgaps and standard enthalpies of formation (energy released upon the formation of a compound). The similarities in the formation energies of Marcasite and Pyrite mean it can be quite difficult to synthesise phase pure FeS_2 in either structure. As the bandgap of Marcasite is also significantly lower, the presence of this impurity would also impact a materials performance towards any water splitting reactions.

Like other photocathodes, FeS_2 also decomposes when in contact with water and/or Oxygen[81] to form Sulphate in oxygenated solutions and Ferric Hydroxide in non-aqueous solutions. Figure 1-6 displays a Pourbaix diagram showing the effect of pH and voltage on the phase of FeS_2.

Material	**Stoichiometry**	**Enthalpy of Formation ΔH_f^0(KJmol^{-1})**	**Bandgap(eV)**
Pyrite	FeS_2	-171.54	0.95
Marcasite	FeS_2	-167.36	0.34

Table 1-2 Comparison of the bandgap and enthalpy of formation of Iron Pyrite with its most common phase impurity, Marcasite.

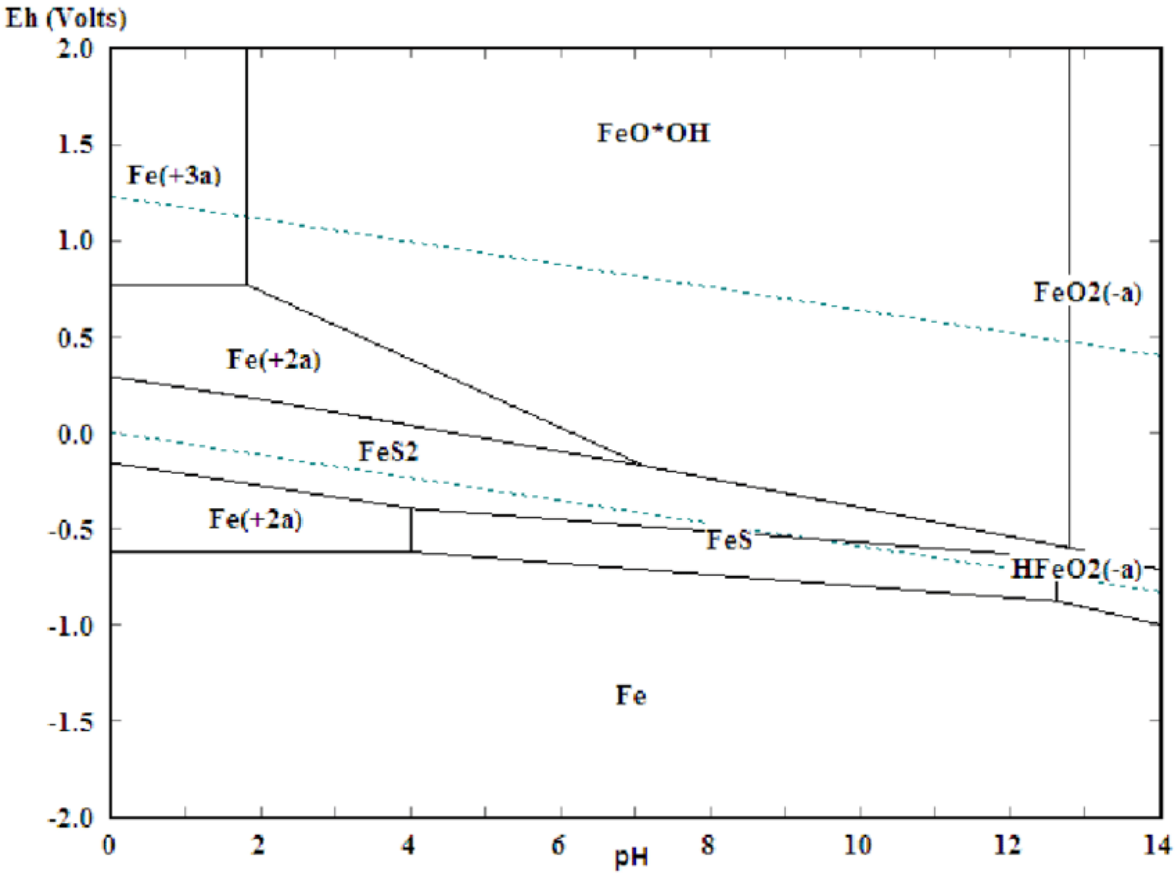

Figure 1-6 Pourbaix diagram of the Fe and S phases at different pH and voltages. Image taken from [172].

Figure 1-6 shows the stability region of FeS_2 spans from 0 to 12.5 pH, however, it has a very small stability of applied voltage. As the band diagram in Figure 1-4 shows an applied bias of approximately -0.3V to -0.6V (dependant on the catalyst) will be needed to drive water splitting reactions on an FeS_2 surface. Even at the highest stable pH for FeS_2, this would be a chemically unstable environment, with the photocathodes surface losing Sulphur and decomposing into FeS and subsequently metallic Fe. Due to the problems stated above, FeS_2 nanoparticle photocathodes are underrepresented in the literature. The only case of FeS_2(P) nanoparticles as photocathodes correlates the effect of nanoparticle size and synthesis method with photocurrent [82]. In addition to this, the paper fails to explain the extremely slow photocurrent transients highlighted within this thesis. [77] reports a detailed study of the defect state density and conductivity mechanism in FeS_2(P) single crystals (111) using

electrochemical impedance spectroscopy and Hall effect measurements. The findings indicate that the presence of a high density of sulphur defect states on the surface result in surface Fermi level pinning, inferring this as a reason for FeS_2s low photocurrent response. [83] investigated the effects of Sulphur annealing on the physical properties of FeS_2 nanocrystals, with FeS_2 defect states also being investigated to some level [83]. However, very little literature is present correlating the effect of Sulphur defect state passivation on photocurrent densities of stability. There is also no literature studying the photoelectrochemistry of FeS_2 quantum dots or any research on FeS_2 quantum dots after a single publication in 1991 [84], investigating FeS_2 quantum dots synthesised via an inverse micelle synthesis.

1.5 Introduction to semiconductors

The materials discussed in the previous section represent some of the semiconductors used as photocathode absorber layers in the literature. When atoms are “brought together” to form an ordered crystal structure, this can be thought of as setting up a periodic potential of positive charge from the nuclei of the atoms. The wavefunctions of electrons, bound to these atoms in discrete orbitals, form standing waves which constructively and destructively interfere with each other. Where the standing waves constructively interfere, there are allowed energy states, and where there is destructive interference there are disallowed energy states. These states can be filled or unfilled depending on the material [67]. At 0K, these allowed energy levels are filled in a solid up to the Fermi level (E_f). There are three main classifications of material determined by three types of band structure; metals, semiconductors and insulators. If the E_f resides within a band of energy states, and there is no separation between the valence and conduction band, the material is a metal and is a good conductor. The E_f may also reside within a forbidden energy region between electron bands, called a bandgap. In insulators this bandgap is greater than 5eV meaning there can

be little to no electron transfer across the bandgap into empty energy states and hence no conduction of electrons. A semiconductor is a material with a bandgap between 0.5 and 4eV[85]. This energy gap represents the minimum energy required to promote an electron into the conduction band and is directly related to the wavelength of light it can absorb. The origin of this forbidden energy region comes from electrons passing through the periodic potential of the crystal lattice and diffracting off the periodic structure. Diffracted electron wavefunctions cancel out at wavelengths that would correspond to energy levels within the forbidden energy region. A more detailed description of this effect can be found in[86].

Control of this bandgap is highly advantageous, as it allows control of the absorption onset of light and conduction band minimum energy levels. There are two main ways to control the bandgap of a semiconductor, doping[87] and quantum confinement[88]. As the physical reasons for the bandgap of a semiconductor lie in the periodic potential and interatomic distances of a crystal structure, it is very sensitive to doping. Fine control of the concentrations and elemental composition of these impurities result in control over the electronic properties of a semiconductor[87]. The incorporation of these dopants can not only increase the bandgap, but also introduce intra-band energy states. If these states lie just below the conduction band and donate electrons they are n-type, if they lie just above the valence band and accept electrons they are deemed p-type. Dopants can also be intrinsic to the semiconductor in the form of defect states within the crystal structure, such as Sulphur defects in FeS_2(P).

Quantum confinement effects on semiconductor nanocrystals describes a broad list of effects that cover any changes to the nanoparticles physical or electronic structure. In this thesis, the term “quantum-confined nanocrystals” is used solely to refer to the alteration of a semiconductor’s bandgap via quantum confinement. The term arises because the effects of quantum confinement are observed when the dimensions of a semiconductor are near to,

or below, the size of a semiconductor's Bohr exciton radius. Where the exciton Bohr radius is defined by equation 1-1 and corresponds to the radius of the electron-hole pair coupling.

$$\alpha_B = \frac{4\pi\varepsilon h^2}{\mu e^2} \qquad 1\text{-}1$$

Where ε is the dielectric constant of the material, h is planks constant and μ is the effective mass of the electron-hole pair. As the Bohr exciton radius is dependent on the properties of the semiconducting material, the size regime for quantum confinement can vary from 2-50nm[76]. As a semiconductor enters this size regime, quantum confinement effects increase the excitonic transition energy, causing a blue shift in the bandgap absorption energy.

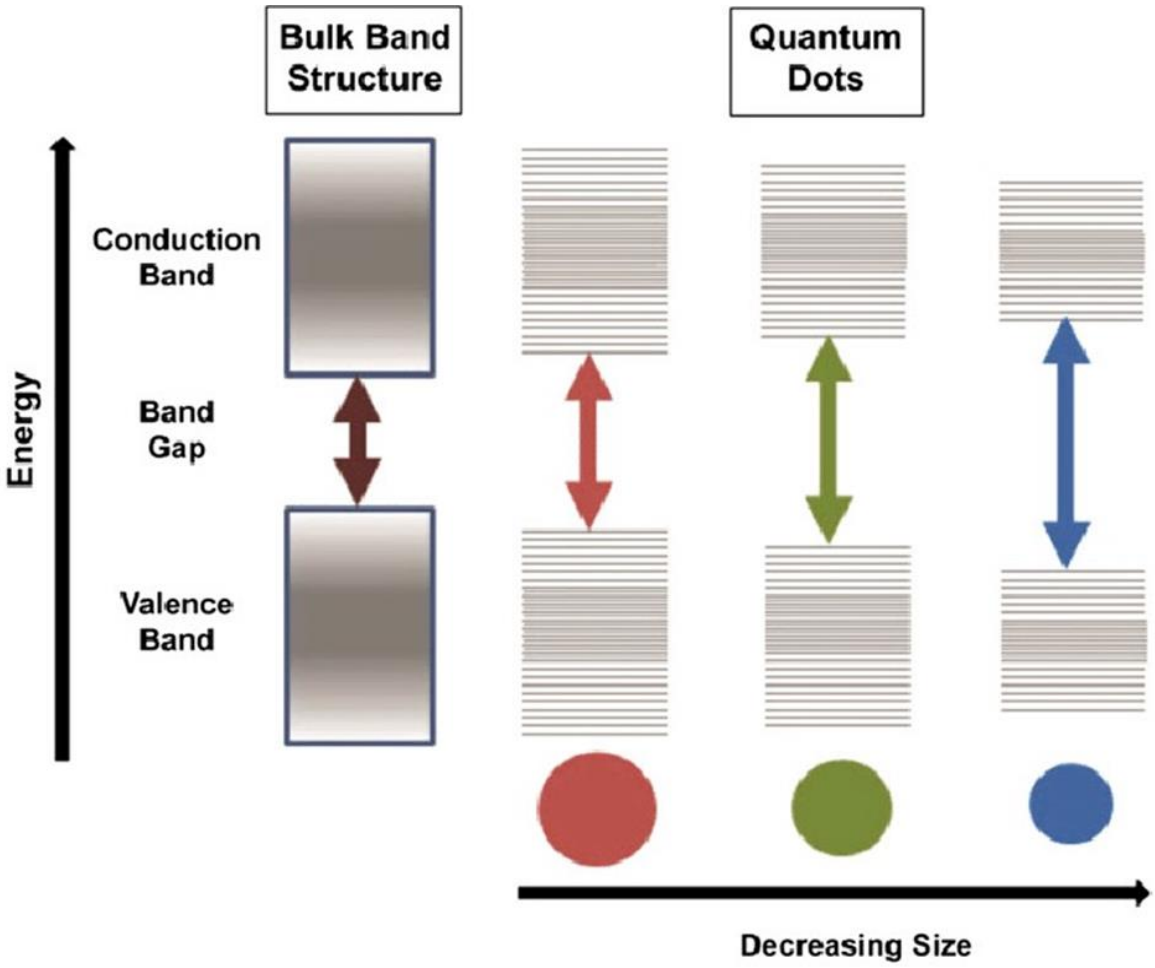

Figure 1-7 Quantum confinement effect on energy levels in semiconductor quantum dots[173]

There is also an effect on the energy bands. Instead of being continuous, as they are in a bulk material, they become discrete and like that of atomic energy levels. Figure 1-7 illustrates how this results in a discrete absorption spectrum instead of a continuous one. Like the origins of bandgaps in semiconductors, a full description of the physical origins is outside the scope of this chapter but is reviewed in [89].

1.6 Purpose of the thesis

The research presented in this thesis is overall directed to understanding the suitability and developing FeS_2 nanomaterials as light absorbers to solar fuels applications. Specifically, the ability to drive HER is investigated.

In Chapter 2, the experimental methods which are used throughout the thesis are presented to supplement discussions in later chapters. The detail with which each experimental technique is discussed is dependent on how heavily the technique is used throughout the thesis. As such, not all discussions on the experimental techniques are comprehensive.

Chapter 3 presents current research on the synthesis of FeS_2 nanoparticles and the development of synthesis for FeS_2 nanoparticles small enough to exhibit quantum confinement effects. The chapter covers the development of two synthetic routes towards quantum dots. Firstly, an inverse micelle synthesis and then a heat-up synthesis. Presented for the first time is the XPS and Raman spectroscopy of quantum-confined FeS_2 nanocrystals. Also covered are the minor modifications to a previously published synthetic route[90] used to make the nanoparticles used in electrodes for the photoelectrochemistry discussed in later chapters.

The aim of Chapter 4 was to optimise FeS_2 thin films for investigations into photoelectrochemical hydrogen evolution. Research was conducted to understand how to increase the stability of FeS_2 electrodes in an aqueous environment with applied bias. The

aim was to stabilise FeS_2 up to a point where it could be experimented with for a reasonable length of time. The motivation for this was to be able to alter FeS_2s defect states and be able to discern differences, something not possible with a rapidly decomposing electrode. To achieve this aim, different passivating over-layers of Al_2O_3 and TiO_2 were deposited onto the surface. The dependence of the thickness of passivating overlayer on the activity of the electrodes was investigated by photoelectrochemistry and Gas Chromatography. A Platinum catalyst was then deposited onto the best performing electrode. The effect this catalyst had on stability and activity was again studied with photoelectrochemistry and Gas Chromatography. The effects of annealing FeS_2 nanoparticle electrodes in different atmospheric conditions was also investigated. The aim of this was to passivate FeS_2 Sulphur defect states via these annealing processes and increase the activity of the electrodes towards the HER. The annealing environments investigated were Nitrogen, Hydrogen:Argon(5%:95%) and Sulphur. The effect of annealing environments on intrinsic FeS_2(P) defects was investigated by fitting XPS data of electrodes after annealing and generating a model.

Chapter 5 compares the photoelectrochemistry of FeS_2 thin films annealed in Hydrogen and Nitrogen atmospheres. Their stability was measured over 3 hours under illumination and Hydrogen evolution measured to calculate Faradaic efficiency. Their solar conversion efficiencies were estimated using the Applied Bias-Photoelectrochemical Efficiency (ABPE) equation, to compare to literature values. In addition, transient photoelectrochemical measurements were performed to assess the effects of annealing on majority carrier trapping and electron-hole recombination.

Chapter 6 of the thesis summarises the work presented over the three data chapters along with the further work that could be carried out as a direct continuation of the research presented here.

2 *Experimental Procedures and Background*

Multiple techniques within this thesis are utilised in the same way across all three research chapters and much of the same background theory is shared. To avoid discussing the same experimental process multiple times across chapters, the core experimental methods and concepts are discussed here. This chapter will cover the principles of the photoelectrochemistry of thin films, and the standard experiments used within this thesis. Following the same structure, Transmission Electron Microscopy (TEM), Energy Dispersive Spectroscopy (EDS), X-ray Diffraction (XRD), Ultra Violet-Visible Absorption Spectroscopy (UV-Vis), Attenuated Total Reflectance Fourier Transform Infra-Red Spectroscopy (ATR-FTIR), Raman Spectroscopy, X-ray Photoelectron Spectroscopy, Inductively Coupled Plasma-Optical Emission Spectroscopy (ICP-OES), Gas Chromatography-Thermal Conductivity Detector(GC-TCD) will be discussed, to appropriate degrees of detail. Preparatory methods will also be discussed including; synthesis of nanoparticles, methods for annealing electrodes, Planinum(Pt) deposition methods on electrodes and Atomic Layer Deposition (ALD) of overlayers on electrodes.

2.1 Photoelectrochemistry of thin films

To understand the processes occurring at the interface of a nanoparticle-electrolyte junction, like those discussed in this thesis, it is first important to understand the basic principles of a semiconductor electrolyte interface (SEI). The theory of the SEI was developed by Gerisher, Pleskov, Memming and Bard in the 1960s to understand a single crystal semiconductor-electrolyte interface.

2.1.1 "Ideal" semiconductor in contact with an inert electrolyte

Few semiconducting materials can be described as ideal, where the surface is perfectly flat with a negligible surface state density. However, it is first easier to describe the interface of

an “ideal” semiconductor in contact with an inert electrolyte containing no redox species in the absence of light. In this unique situation, if the potential of a semiconducting electrode is varied with respect to a reference electrode it behaves much like a capacitor. In this example, the electrodes are in, what is called, a three-electrode system. In this system there are three electrodes; working, reference and a counter electrode, sometimes called the auxiliary electrode. The working electrode is the material being studied, in this case, the semiconductor. A reference electrode is a material with a known potential with which to reference the potential of the working electrode. A counter electrode acts as the other side of the cell with a potential opposite to that of the working electrode. As the potential in this system is increased, positive charge will build up, and as it is decreased, negative charge will build up. The potential at which there is no net charge distribution across the semiconductor side of the semiconductor-electrolyte interface is called the Flat Band Potential (V_{FB}). The band diagram of an n-type semiconductor is shown in Figure 2-1, where electron donors sit energetically just below the conduction band, being ionized at room temperature, to donate electrons to the conduction band.

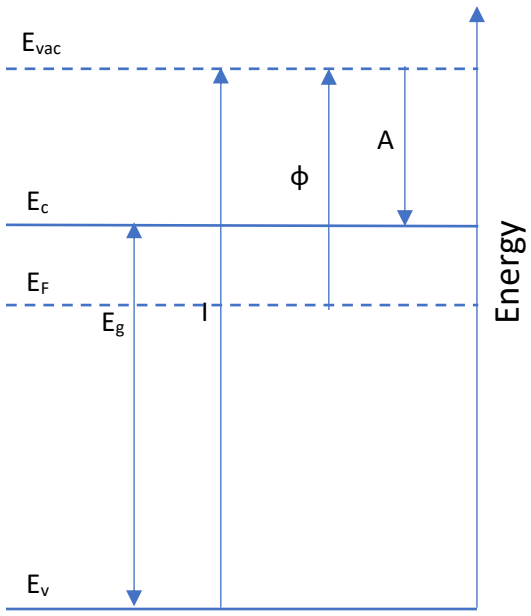

Figure 2-1-Energy level diagram for a n-type semiconductor. E_c is the conduction band minimum, E_v is the valence band maximum, E_f is the fermi level, I is the ionisation energy, ϕ is the work function, A is the activation energy, E_{vac} is the vacuume energy minimum and the energy at which electrons are ejected from a material.

In this example, the flat band potential is the potential at which the number of electrons in the space charge region is the same as the number of ionized donor atoms (D^+). At V_{FB} there would be no electric field across the semiconductor because there would be no excess of charge. However, if the case is considered where the potential is varied positively with respect to the flat band potential, electrons are withdrawn via the electrode contacts and the density of ionized donors (D^+) will outweigh the electron density. In this scenario the material is in a depletion condition and a positive space charge layer is formed at the surface. The width of this space charge region, W_{sc}, depends on the permittivity of the material, the dopant density and the size of the potential difference across the region, shown by equation 2-1, where W_{sc} is the width of the space charge layer, N_d is the number of donor atoms, ε_0 and ε are the permittivity of free space and the material, respectively, and $\Delta\emptyset_{sc}$ is the potential drop across the space charge region.

$$W_{sc} = \left(\frac{2\Delta\emptyset_{sc}\varepsilon\varepsilon_0}{qN_d}\right)^{\frac{1}{2}} \qquad \textbf{2-1}$$

This space charge region sets up an electric field which varies linearly as a function of depth into the ideal semiconductor, corresponding to a parabolic variation of electrical potential.

The variation of potential across the width of the space charge region results in a shift in the energy levels of the electrons and holes in the region, resulting in band bending shown in Figure 2-2[91]. Any change in charge density in the semiconductor is compensated for by an equal and opposite change in the charge density in the electrolyte side of the junction called the ionic charge (Figure 2-2). The physical length scale of this charge distribution at the semiconductor electrolyte interface is called the Helmholtz double-layer, the length of which is dependent on the charged species in the electrolyte. The Helmholtz layer is not shown in Figure 2-2 because it is several orders of magnitude smaller than the space charge layer. The

more positive, or negative, the applied potential is than the flat band potential, the greater the band bending and larger the double layer.

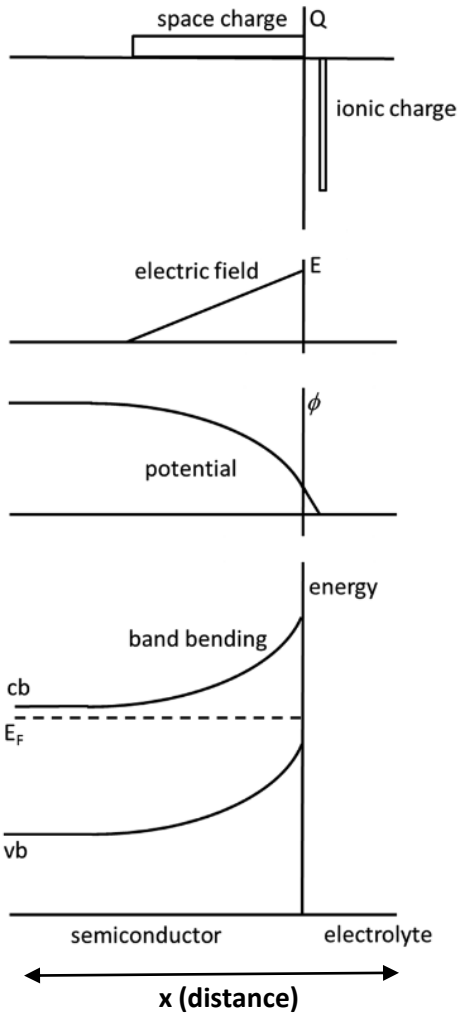

Figure 2-2 Diagram showing a) how the space charge layer is compensated for by ionic charge on a crystals surface, b) distribution of electric field in the space charge region and c) the band bending in the space charge region. In this figure Q is charge, E is electronic field, Ø is potential energy, cb is conduction band, E_F is fermi energy and vb is the valence band.

2.1.2 "Ideal" semiconductor in contact with a redox-electrolyte

If an "ideal" semiconductor was immersed into an electrolyte containing a redox couple, there would be electron transfer across the surface. The electron transfer would continue until the Fermi levels in the semiconductor and the electrolyte are the same and an equilibrium is established. The potential at this point is called the open circuit potential and is equal to the difference between the reduction and oxidation potentials of the redox couple within the system. Electron transfer across the semiconductor-electrolyte interface, in a naive way, can be thought of to proceed if the energy of the electron in the solid is greater than that of the reduction energy of the species in the solution. In the 1960s, Gerishier developed a theory to describe this process using electronic energy levels. At the core of his argument is the concept that an electrolyte is made up of molecules with fluctuating energy levels. The conceptual origin of this is the fluctuation of a solvent shell around the solvated ions in an electrolyte. In addition to this, there are also interactions with molecules outside this inner sphere solvent shell, via Coulomb interactions. The sphere of influence of these Coulomb interactions is called the outer sphere. The motion and vibration of these molecules, due to thermal excitation, causes the energy level of the ion, observed from the frame of reference of the electrode, to fluctuate. For a semiconductor, charge transfer will take place either via the conduction band minimum, valence band maximum or surface states. Electron transfer across the surface occurs physically via tunnelling; this requires the energy of the molecule in the solution to be at the same energy as the electron/hole in the material. Even though the energy levels of the molecules in the electrolyte are continually fluctuating, the ionic reorganization that causes these fluctuations is very slow compared to the tunnelling process. It can, therefore, be assumed that the energy of a molecule is constant through the transfer process, this assumption is a part of Debye-Huckel theory[92].

2.1.3 Nanostructured semiconductor surface-electrolyte interface

The nanostructured electrodes discussed here can behave slightly differently to the ideal case discussed previously. The main difference is the reduced size of the material and the occurrence of band bending. If the size of the nanoparticle is smaller than the Debye length, which is dependent on dopant concentration, then it is not possible to form any considerable amount of band bending. The Debye length in a semiconductor is the distance over which the electrostatic force of a minority carrier is screened. The size of the Debye length is inversely proportional to dopant density, therefore the higher the dopant density, the smaller the Debye length. The relation of Debye length to the potential difference at the surface of a semiconducting particle to its surface (band bending) is shown by equation 2-2[91]

$$V_{BB} = \frac{KT}{6e}\left[\frac{r-(r_o-D)}{L_D}\right]^2\left[1+\frac{2(r_0-D)}{r}\right] \qquad \textbf{2-2}$$

Where L_D is the Debye length in a semiconductor and is inversely proportional to dopant concentration. The radius of the semiconducting particle is r_0 and r is the distance from the centre of the particle. D is the depletion length, shown by equation 2-3[93].

$$L_D = \left(\frac{\varepsilon_r \varepsilon_o KT}{e^2 N_d}\right)^{\frac{1}{2}} \qquad \textbf{2-3}$$

Where K is Boltzmann's constant, T is temperature, N_d is dopant concentration, e is the charge on an electron and ε is the dielectric constant.

2.1.4 Hydrogen evolution reaction

The hydrogen evolution reaction mechanism proceeds one of two ways on the surface of an electrode[94]. Both pathways start with the Volmer reaction, shown by equation 2-4[95].

$$H^+ + e^- \rightarrow H_{ads} \qquad \textbf{2-4}$$

The reaction pathway then follows either the Heyrovsky reaction, where the absorbed Hydrogen bonds directly to a hydrated proton, shown by equation 2-5[95]

$$H_{ads} + H^+ + e^- \rightarrow H_2 \qquad \textbf{2-5}$$

alternatively, it proceeds via the Tafel reaction, where two adsorbed Hydrogens diffuse along the electrode surface and combine as shown by equation 2-6[95].

$$H_{ads} + H_{ads} \rightarrow H_2 \qquad \textbf{2-6}$$

2.1.5 Conversion efficiencies

Energy conversion efficiency is an important metric when determining how fit for purpose a photoelectrochemical cell is towards water splitting for solar energy conversion. Faradaic efficiency (*FE*) is one of the most useful parameters of the efficiency of a photoelectrochemical cell, as it takes into account how much of the current across the electrode or photocurrent density is due to water splitting. It is the ratio of the generated Hydrogen to the amount that is theoretically possible. Equation 2-7 modified from [38], expresses this relationship.

$$FE = \frac{2 \cdot Hydrogen\ produced (N_A)}{number\ of\ electrons\ passed\ over\ electrodes\ surface} \qquad \textbf{2-7}$$

Strictly speaking, the Faradaic efficiency (FE) is determined by the photocurrent only, however, in this thesis, the overall current passing over the interface is used. Any increases to FE would signal a decrease in electrons going to unwanted reactions, such as reactions between the electrolyte and photocathode. While there are other metrics used as benchmarks for efficiency such as Incident Photon to Current Efficiency (IPCE) these are not

suitable in the case of this thesis. This is because they rely on the knowledge of the amount of photocurrent produced due to illumination, and it was not possible to separate current density due to photocurrent from that due to side reactions. For these reasons, only the metrics discussed above will be used to compare the efficiencies of electrodes in Chapter 5 of this thesis.

The overall solar-to-hydrogen conversion efficiency is given by equation 2-8, where $\mathrm{j_{photo}}$ is the photocurrent of the photocathode, $\mathrm{V_{redox}}$ is the voltage of H_2/H reduction vs RHE, $\mathrm{V_{bias}}$ is the voltage of applied bias vs RHE and $\mathrm{P_{light}}$ is the power of the incident light.

$$Efficiency_{STH} = \frac{j_{photo}(V_{redox} - V_{bias})}{P_{light}} \qquad \textbf{2-8}$$

However, this is only valid if the Faradaic efficiency is unity and if this is not the case the equation is altered to the form in equation 2-9, giving the Applied Bias-Solar-to-Hydrogen conversion efficiency (AB-STH).

$$AB - STH = \frac{|j| \cdot FE \cdot (V_{redox} - V_{bias})}{P_{light}} \qquad \textbf{2-9}$$

2.1.6 Typical photoelectrochemical experiments

All photoelectrochemical experiments were conducted under inert conditions in cells degassed using Argon (Ar). To degas a cell a needle is inserted into the working electrolyte through a septum, while another is inserted through a septum into the headspace. Ar is bubbled through the cell for 30 minutes, sparging the electrolyte and purging the headspace simultaneously. Once a cell is degassed, it is transferred to the photoelectrochemistry equipment in a dark room and connected to a potentiostat. The cell is left for five minutes either in the dark or under illumination to reach equilibrium before starting the relevant experiment. The reason for this waiting step is due to the extended photocurrent decay and onset times, discussed in Chapter 5.

There are two types of photoelectrochemical experiments performed and discussed in this thesis; Chronoamperometry (CA) and Linear Sweep Voltammetry (LSV). Both are performed in dark and under constant illumination. In addition, CA is also performed under chopped illumination. Unless otherwise stated the working electrolyte for all experiments is a 0.1M phosphate buffer solution at pH7.

In a typical CA experiment under steady-state illumination conditions, after the equilibration steps, a bias of -0.19V vs. RHE is applied to the working electrode. The bias is held for three hours after which the Hydrogen evolution is measured by sampling the headspace with a GC-TCD. For experiments under chopped light conditions, the core experimental method stays the same with minor variations. For the equilibration step, the electrode is kept under constant illumination for five minutes, after this the bias of -0.19V vs. RHE is applied. The lighting from the lamp is then chopped on and off using optically dense card inserted into the light pathway periodically.

In a typical LSV experiment, after the equilibration steps, the voltage is varied from 0.61V to -0.39V vs. RHE at $10mVs^{-1}$, either under illumination or dark conditions. This measurement could then be either repeated continuously on the same electrode as a gauge of stability or stopped after one cycle.

2.2 Electron microscopy

Electron microscopy is an extremely versatile tool for the investigation of nano and micron sized materials, not only for images of structure but also for detailed chemical analysis. This section will cover a brief overview of the operating principle of an electron microscope as well as sample preparation. Energy Dispersive X-ray Spectroscopy (EDS) will also be included in detail.

There are two forms of electron microscopy, Scanning Electron Microscopy (SEM) and Transmission Electron Microscopy (TEM), the latter has a scanning operation mode as well as transmission mode. The main components in a TEM are; an electron source and column, electronics for focusing and deflecting the beam, a high vacuum system and control software. Optical microscopy (OM) and Electron Microscopy (EM) share the same basic principles. Where OM uses convex and concave lenses made of glass to refract and focus the light, EM uses carefully calibrated electromagnetic lenses to focus electrons. The resolution of a microscope is its ability to resolve two objects close to each other and is proportional to the wavelength of the probe used, as defined by the Rayleigh Criterion[96]. Switching to electrons therefore increases the resolving power of a microscope, for electron microscopes this resolving power is around 50 pm [97]. This improvement is because the resolution limit of a microscope is proportional to the wavelength of the probe, demonstrated by equation 2-10[98].

$$R = \frac{0.61\lambda}{NA} \qquad \textbf{2-10}$$

Where R is the resolution limit, λ is the wavelength of the probe (i.e. visible photons for a light microscope) and NA is a dimensionless factor called the numerical aperture.

Visible light has a wavelength from 400-700nm, whereas electrons have a De Broglie wavelength of 3.70 pm (at 100 KeV). In this example, the resolution limit would improve by 5 orders of magnitude. The entire length of the electron column must be held under vacuum because of the use of electrons as the probe. If the column was under ambient pressure, the electrons would only travel around $3.35 \times 10^{-8} m$ whereas in a high vacuum it will travel around 1530 miles before scattering. The latter of the two is the one that is necessary to perform any useful measurements on reasonable timeframes.

SEM is like TEM in that it also consists of the same four main components. However, the column is considerably shorter as only the lenses above the specimen, necessary to focus the electron beam into a fine spot, are needed. The electron beam is raster-scanned over the sample in a rectangle, the signals from each point are stored, and a greyscale image is created. Usually, the signal intensity used to create this image is from the secondary electrons, the origin of which is shown simply in Figure 2-3A. Due to the small penetration depth, these electrons will have the best spatial resolution of all possible signals. The specimen no longer needs to be thin, as it is for TEM, and as a result, the acceleration voltages do not need to be as high, typically ranging from 1-30KeV depending on the desired scientific information.

Scanning Transmission Electron Microscopy (STEM) is an amalgamation of the principles of TEM and SEM. STEM, like TEM, is used to observe thin samples and looks at the beam of electrons transmitted through the sample. The primary advantage over TEM is that as the electron beam is raster-scanned over the sample, it generates spatially correlated secondary signals, such as characteristic X-rays which can be used to create elemental maps. Interactions between this raster-scanned beam, the sample and its atoms produce a signal which is used to build a virtual image by correlating beam position with intensity and creating a greyscale image. SEM and STEM are two very similar techniques, however, STEM has a higher spatial resolution. The reason for the increased resolution is due to the increased energy of the electrons which relates to resolution as discussed above.

2.2.1 Energy dispersive spectroscopy

X-rays were discovered in 1895[99] and scientists soon realised that the wavelength of X-rays emitted by excited atoms was firmly related to atomic structure. When an X-ray photon is absorbed by an atom an electron is excited into a higher energy orbital. When the electron relaxes back into a lower energy state it releases a photon with a wavelength corresponding

to the energy difference of the two states. As each chemical element has a different energy level structure, the nature of elements can be deduced from the emitted photon wavelength. In the early 1920s, most of the “patterns” from the stimulated emission of X-rays from elements were recorded. In 1949, Raymond Castaing developed the first static beam electron microprobe, the groundwork for modern X-ray microphysics [100]. However, measurements were time-consuming until Fitzgerald et al. developed the first Li-drifted Silicone detector (Li)Si in 1968 [101]; a development that allowed the recording of an entire energy spectrum at the same time. The field briefly switched to high purity Germanium detectors (HPGe) with a higher efficiency. The increased efficiency translated into increased special resolution by allowing for a narrower electron beam. Current detectors use Si drift detectors (SDD). These use a similar operating principle to the (Li)Si detectors of the 1960s with drastic design changes to increase sensitivity, such as developments in converting the current to voltage using a Field Effect Transistor (FET) integrated on the chip instead of externally [102]. In 1995, John Frial at Princeton developed Position-Tagged Spectroscopy (PTS) meaning an entire spectrum could be stored at every pixel, paving the way for high-resolution elemental mapping.

2.2.2 Operating principle of energy dispersive spectroscopy

Electrons are emitted by an electron gun and travel through several electron-optical elements, dependent on the microscope, before interacting with the sample. During that interaction, some or all of the kinetic energy of these electrons is transferred to the sample, resulting in several analytical signals. Figure 2-3A depicts these signals[103].

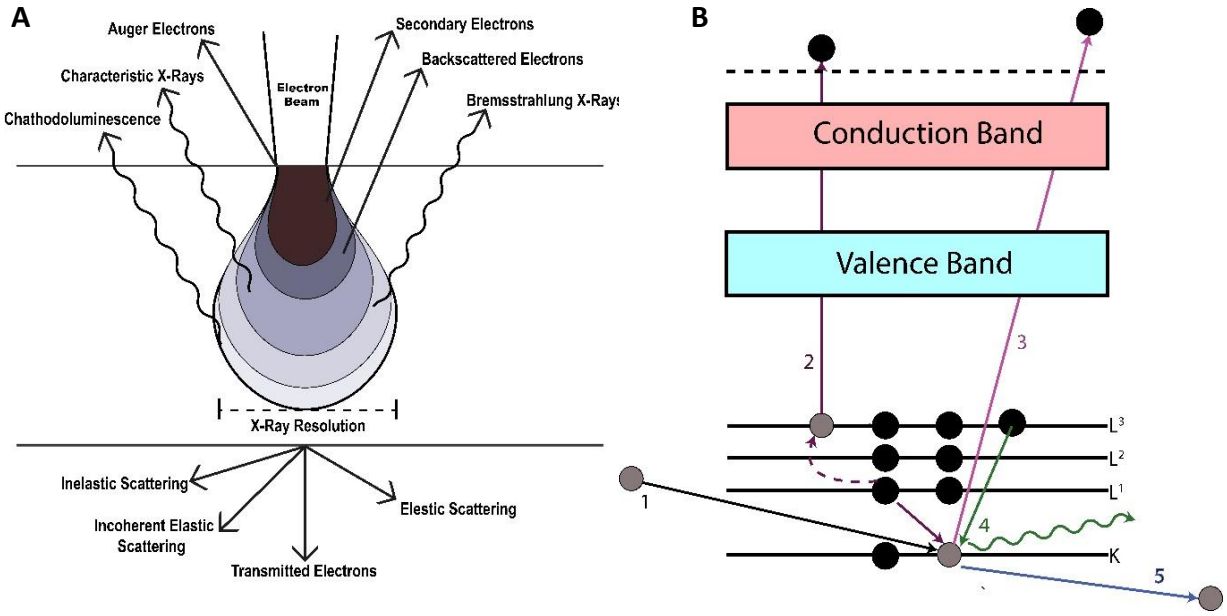

Figure 2-3(A) depicts the types of analytical signals created by the interaction of an electron beam with a sample in an electron microscope. (B) Energy diagram showing the excitation/relaxation mechanisms caused by the collision of electrons with atoms in a sample. Pathway 1: Incoming primary electron. Pathway 2: Auger electron emission. Pathway 3: Secondary electron emission. Pathway 4: Photon emission (characteristic X-rays). Pathway 5: Inelastic scattering.

Secondary electrons are ejected out of atoms after interacting with primary electrons from the electron beam. Their excitation pathway is described by Pathway 3 in Figure 2-3B. Typically these electrons escape the atomic potential well with less than 50 eV. As a result, they are only detected if they originate near the surface of the sample [104]. The area the

primary beam interacts with, and scatters, within a sample is depicted as the onion shape shown in Figure 2-3A. The highest number of secondary electrons are generated in the darkest section of this onion-shaped area by the primary electron beam. This means that secondary electrons also have the highest spatial resolution of the different analytical signals. Shallow depth of detection and narrow special resolution make secondary electrons the best for high-resolution SEM images.

Backscattered electrons result when primary electrons from the electron beam scatter off the nucleus of an atom within a sample. Inelastic scattering interactions result in relatively low energy loss. As a result, the emerging backscattered electrons are of higher energy than secondary electrons. This means they can originate from deeper in the sample than secondary electrons and still be detected. The spatial resolution from these electrons is much less than that of the secondary electrons. However, these electrons are sensitive to the atomic mass of the nuclei they have interacted with. Therefore some compositional information, as well as low-resolution topographical information, is gathered from them.

Auger electrons can be emitted when an electron in an atom excited by primary electrons relaxes into a lower energy state, emitting an X-ray. This X-ray is then absorbed internally, within the atom, by an electron at a higher energy state which is then ejected from the atom. This process is depicted in Figure 2-3B as Pathway 2. The emitted electron has an energy equal to the difference between the absorbed X-ray and the binding energy of the ejected electron. These electrons have two unique characteristics that set them apart from all other analytical electron emissions from a sample. Firstly, they have a very low kinetic energy and therefore can only come from between one and three atomic layers deep in the sample[104]. Secondly, they have an energy characteristic of the atom they originate from and carry chemically-specific information.

Characteristic X-rays are generated when an electron is ejected via interaction with a primary electron, as shown in Figure 2-3B Pathway 3. An internal electron from a higher energy state then relaxes down into this core vacancy, emitting a photon in the process. The energy of the emitted X-ray is equal to the energy difference between the inner and outer energy shells of the atom, and hence holds element-specific information[104].

Primary electrons from the beam can also be scattered inelastically in a material and, in the process, giving up all or very little of its kinetic energy. The energy emitted by this process is predominantly Bremsstrahlung radiation (Figure 2-4) and can have a continuous energy distribution[105]. This wide energy distribution is the primary cause for the background signal observed in EDS measurements. Due to the structure of atoms, a near miss is more likely than a direct collision. Therefore, there is a region of relatively higher energy in the continuum due to lower energy photons tapering off at higher energies.

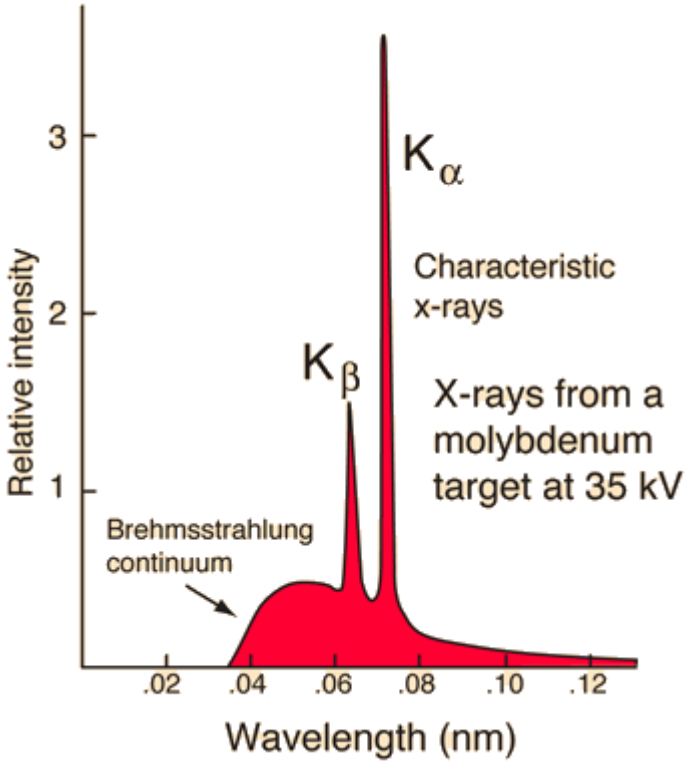

Figure 2-4- Example X-ray spectrum of a molybdenum target

2.2.3 Sample preparation for electron microscopy

For preparing nanoparticles from a solution for SEM, carbon tape is attached to the top of a mushroom stub made from Aluminium. The nanoparticle solution is then drop-cast onto the carbon tape and allowed to dry. For higher boiling point solvents, it might be necessary to dry the stub further in a vacuum, to remove all the solvent, as SEM is a Ultra High Vacuum (UHV) technique. For samples on larger substrates, like Transparent Conducting Oxide (TCO) slides, the slide is stuck to a mushroom stub using carbon tape. Silver paste is used to connect the sample electrically to the mushroom stub to help prevent charging of the sample surface. The samples surface is then coated with a thin conductive overlayer, usually Chromium, to further avoid charging of the sample.

Preparation of STEM/TEM nanoparticle samples is done by drop-casting from a dilute solution of nanoparticles onto a Carbon film on a Copper (Cu) support grid. To prepare samples for cross-sectional STEM, for elemental analysis, the process is slightly more involved. First, the sample is coated with a large over-layer of Chromium, at least 100nm thick. Pt is then deposited with an electron beam, to help provide contrast to where the sample ends and provide support. A section of the sample with the substrate is subsequently removed via Focused Ion Beam (FIB) milling and attached to a Cu support. In FIB milling a focused beam of ions, generally Gallium (Ga) atoms, are directed at a sample and used to ablate off material. This technique can be used to do depth profiling, taking off one surface layer at a time, or to cut out a section of a thin film for study.

Electron transparent lamellae TEM specimens of a cross-section of the annealed films were produced using the lift-out method[106] using an FEI Helios NanolabTM 600i DualBeam Ga FIB-SEM. To reduce the thickness of damaged surface layers, films were subjected to a 5KeV low energy surface wipe. STEM measurements were performed using a probe side, CEOS GmbH, aberration-corrected JEOL 2100FCs microscope, operating at 200KeV. Bright Field

(BF) and High Angle Annular Dark Field (HAADF) images were recorded in tandem and EDS maps were acquired using an EDAX T-Optima 60mm^2 windowless detector with EDAX TEAM software.

2.3 X-ray diffraction

2.3.1 Operating principle

X-ray diffraction (XRD) is a powerful technique which can be used for determining the crystal structure of an unknown material. The measurements can be quick and hence are commonly the first step in confirming whether a synthesis has yielded desirable products. However, there are some limitations to this method. Unless measurements are being conducted at a synchrotron beamline, it is generally not feasible to perform analyses in inert conditions, posing a problem to any Oxygen-sensitive materials. There is also a lower limit of detection for XRD to measure any impurity phases; this is typically around 0.01% at a synchrotron[107] and around 1-2% with standard lab equipment. Therefore, even though XRD is a valuable technique for materials characterisation, it should always be used in tandem with other analyses.

The two modes of operation for XRD characterisation used in this thesis are Powder XRD Bragg-Brentzano (BB) and Grazing Incidence XRD (GIXRD). The two methods are shown schematically in Figure 2-5A for GIXRD and Figure 2-5B for BB. In GIXRD mode, the impinging X-rays from the source are aligned to interact with the sample at a grazing angle of incidence of around 5 degrees. A standard process would be to optimise this angle to achieve the highest possible desired signal by varying the angle and observing the intensity of a known peak. Once this angle has been optimised it is fixed, and the right-hand side of the system is rotated around the desired range of angles (2Θ) to collect a scan. GIXRD measurements can take much longer to complete than BB due to the decreased signal. In Figure 2-5, the axis labelled ‘S’ bisects the angle between the axis of incidence and the axis of reflection equally.

This axis is moved left and right as the detector moves. The concept of this 'S' axis aides in the description of BB. Unlike GIXRD, the angle between the axis of incidence and reflection is kept the same. Therefore 'S' is continuously kept normal to the surface of the sample while the source and detector move around to scan the required values of 2Θ. In addition to this, the sample is rotated at a constant rate as to not bias towards one specific angle of reflection. This rotation allows for preferential orientation of the crystal lattices to be ascribed to a crystal structure and not a measurement anomaly. Without rotating the sample, the increased intensity from certain XRD reflections could instead be due to the preferential orientation of particles when drying on a sample plate.

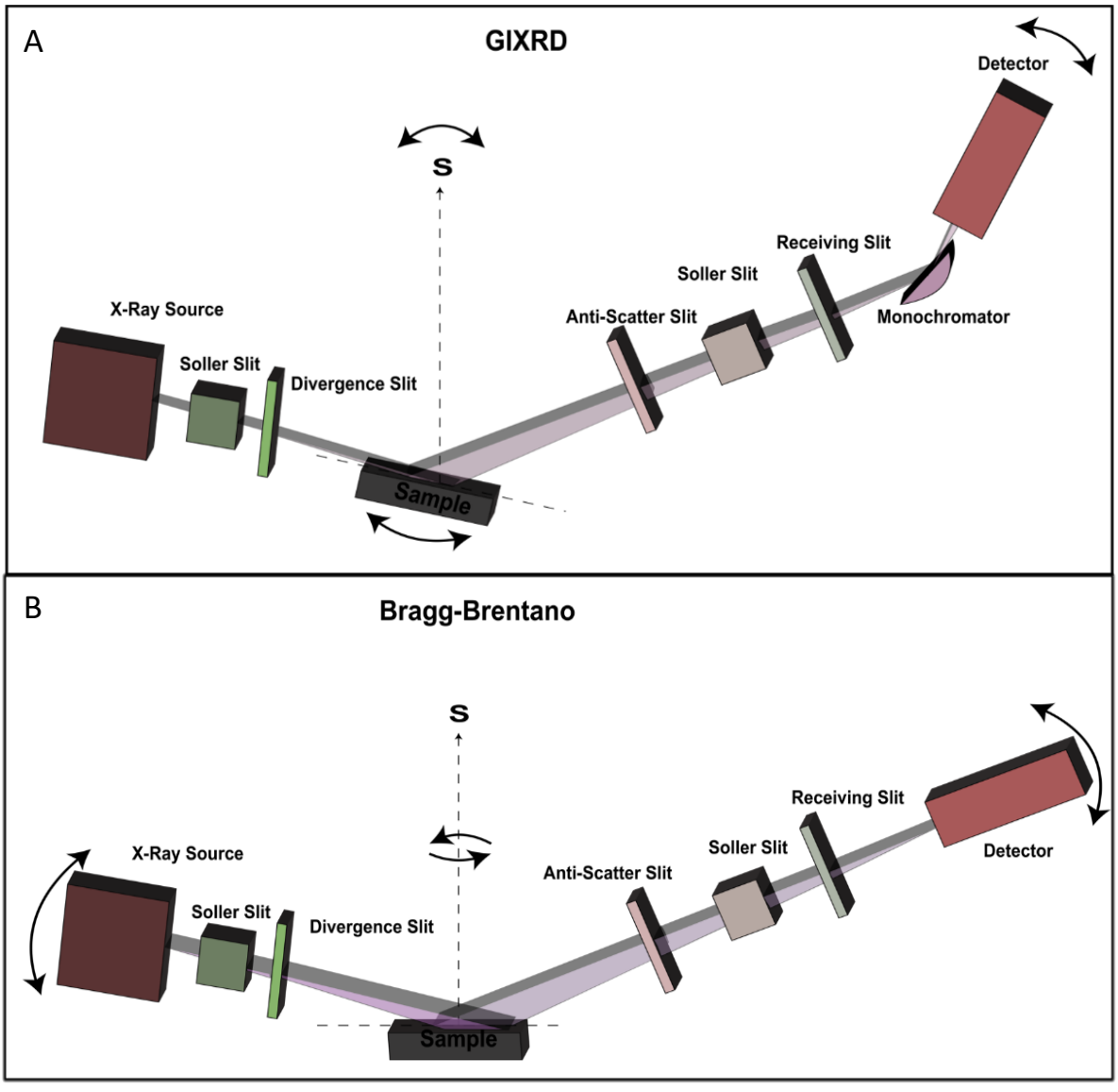

Figure 2-5 Schematic of (A) GIXRD mode and (B) BB mode.

2.3.2 Sample preparation

Sample preparation for BB can be done in one of two different ways. Firstly, nanoparticles can be drop-cast from solution onto a glass XRD plate and allowed the appropriate amount of time to dry. Secondly, a powder can be formed comprising of the nanoparticle material by drying the solution in a vacuum.

2.4 Spectroscopic techniques

"Spectroscopic techniques" covers a vast array of analysis methods and strictly speaking covers all techniques that monitor how electromagnetic (EM) radiation interacts with a sample. This section will cover Fourier Transform Infrared Spectroscopy (FTIR), Ultraviolet-Visible Spectroscopy (UV-VIS), Raman Spectroscopy, X-ray Photoelectron Spectroscopy (XPS) and Inductivley Coupled Plasma-Optical Emission Spectroscopy (ICP-OES) in varying degrees of detail, appropriate to their degree of importance in the thesis. EDS whilst also a spectroscopic method essential to this thesis, it is more suited to a discussion alongside (S)TEM and SEM which can be found in Section 2.2.1.

2.4.1 Ultra violet-visible absorption spectroscopy (UV-Vis)

UV-Vis spectroscopy is a technique which analyses how a beam of light in the UV visible range is attenuated after passing through, or being reflected by, a sample. During a measurement, the wavelength of light incident on a sample is scanned between two desired points and the absorption at each wavelength recorded. When a sample is exposed to photons that correspond to an allowed transition, electrons are excited to a higher energy state. If the sample is a semiconductor and the wavelengths are scanned from long to short, the onset of this absorption usually corresponds to the bandgap of the material. This is the minimum energy required to excite an electron from the materials valence band to its conduction band. As well as contributions from absorption, in UV-Vis there are also scattering

contributions. These are not included in this thesis as they are negligible for colloidal particle systems.

2.4.1.1 Sample preparation

In this thesis, all samples were measured using UV-Vis in transmission mode instead of reflectance. To prepare samples of colloidal nanoparticles for measurement, diluted nanoparticle solutions were transferred into a cuvette made of optical grade quartz with a known path length. An identical cuvette filled with only solvent was used as reference for baseline measurements. UV-Vis measurements of these films were carried out by using a clean Indium doped Tin Oxide (ITO) slide as the background measurement, and the films were measured as prepared.

2.4.2 Fourier transform infra-red spectroscopy (FTIR)

For FTIR, infrared (IR) light from a source is passed through a Michelson interferometer along the optical path where it interacts with the sample producing an interferogram which contains information about how the sample has absorbed each frequency of IR light. A Michelson interferometer contains a beam splitter, a moving mirror, and a stationary mirror. The incoming light is split by the beam splitter and reflected by both the moving and stationary mirrors to be recombined by the beam splitter. The moving mirror causes changes to the optical path length compared to the stationary mirror, resulting in changes to the phase difference of the recombined light beam causing interference light. The absorption of interference light by the sample is recorded in an interferogram along with the changes in optical path length. Using a Fourier Transform, the interferogram consisting of light

absorption and optical path length is converted to a spectrum containing the absorption of the different frequencies of IR light by the sample.

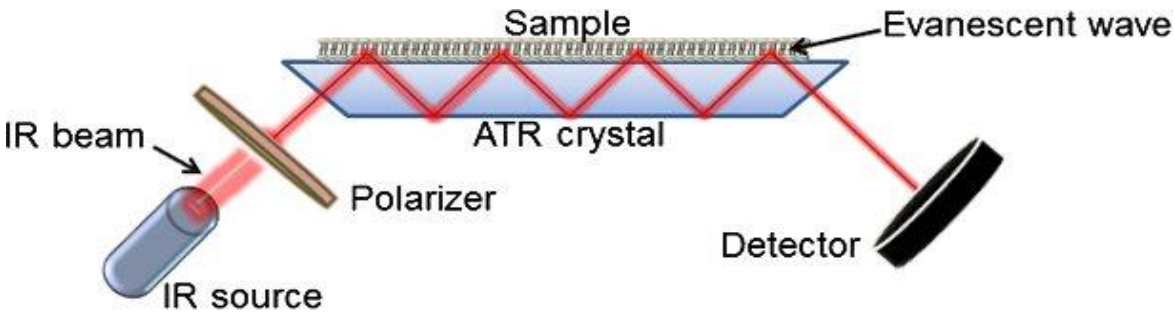

Figure 2-6-Beam path of infrared beam in an ATR-FTIR experiment, showing the evanescent waves at the core of the analysis technique [174].

There are multiple modes of measurement for FTIR, the method used in this thesis is called Attenuated Total Reflection (ATR). The advantage of ATR is that samples can be measured directly in their solid or liquid state without the need for further preparation. The main principle of the method is depicted in Figure 2-6. An infrared beam from a Michelson interferometer is passed through a crystal with a high refractive index and is internally reflected within this crystal. Where the beam interacts with the crystal sample interface, an evanescent wave is formed which penetrates 0.5-2uM into the sample. The beam is then converted to an absorption spectrum as described above. This evanescent wave effect only happens if the crystal has a higher refractive index than the sample, hence the need for a crystal with a high refractive index. If the sample has a higher refractive index, the IR beam will be lost in the sample. The penetration of this evanescent wave into the sample is directly related to the sensitivity of the measurement. Therefore, solid samples are usually mechanically forced into contact with the crystal by a clamp.

2.4.3 Raman spectroscopy

2.4.3.1 Operating principle

When light is incident upon a molecule or crystal structure the majority of the light that is scattered does so elastically. This process is known as Rayleigh scattering, and the photons have the same energy as they did before being scattered. However, a tiny fraction of scattered light (0.001%) is scattered inelastically in a process known as Raman scattering, discovered by V.C. Raman in 1928[108]. In Raman scattering there are two main processes, Stokes and Anti-Stokes scattering (Figure 2-7). For Stokes Raman scattering, a photon excites a phonon from the ground state to a virtual energy state that depends on the energy of the exciting photon. Loss of energy by interaction with a vibrational/rotational or other low energy state causes the electron to relax into an energy state higher than it originated. This energy level discrepancy causes the scattered photon to have lower energy and carries information about the vibrational state that it interacted with. In Anti-Stokes Raman Scattering, a phonon is excited from an already excited state which, after being excited to the virtual energy state, drops back down to the ground state causing the scattered photon to have higher energy. Relative intensities of these two processes depend on the vibrational/phonon population of the states within the sample. As the phonons within the sample are excited thermally, the populations can be calculated using Boltzmann statistics, however, at room temperature the number of phonons expected to be excited is low. For this reason, it is Stokes scattering that is predominantly used. The energy shift due to Stokes scattering is related to the vibrational/rotational energy of the bond with which the excited phonon interacted. As bond vibration/rotational energy levels are specific to the crystal structure and chemical environment, Raman scattering can be used to determine what molecule or crystal structures are present within a sample and how pure they are.

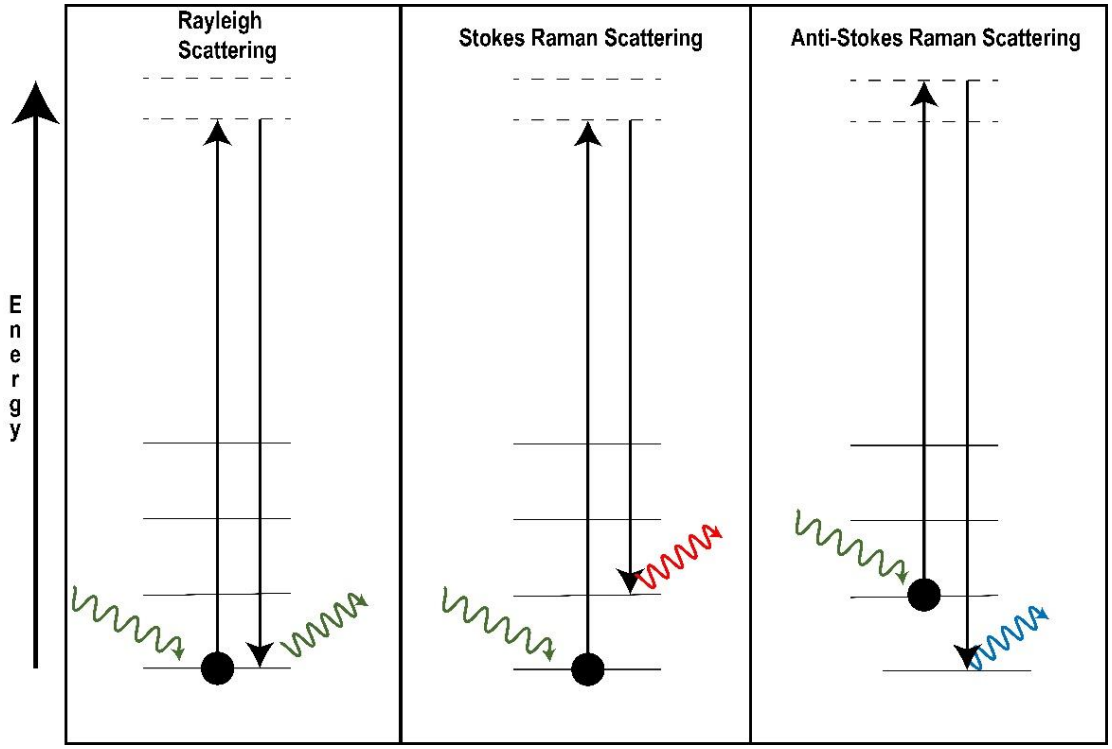

Figure 2-7- Schematic description of the differences between Rayleigh, Stokes and Anti-Stokes scattering in the context of energy levels.

2.4.3.2 Sample preparation

Sample preparation for standard Raman spectroscopy measurements is a simple process. Solutions are drop-cast onto glass slides and allowed to dry. Powders are adhered to a glass slide with either Carbon tape or vacuum grease. The glass side is then loaded into the equipment and fixed in place.

2.4.3.3 Notes on measurement techniques

While measuring some samples, especially oxidation sensitive materials, such as FeS_2, it is important not to set the laser power too high. With very little power it is possible to observe peaks due to a Fe oxide which can cause inaccurate conclusions regarding the purity of a sample. Unfortunately, this need to use low laser powers causes a very low signal to noise ratio. To compensate for this, acquisition times must be adjusted to around 30 seconds for each spectrum acquisition and accumulated 50-150 times to observe adequate signal to

noise ratio. Another option to long, low power scans is to conduct measurements in gas-tight cells to avoid oxidation at higher laser powers. The latter was the method which was adopted for the measurement of FeS_2 quantum dots in Chapter 3 of this thesis.

2.4.4 X-ray photoelectron spectroscopy (XPS)

Materials that appear to be in a pure desirable phase in bulk analysis techniques can have a completely different composition at their surface. XPS is sensitive to the top 1-5nm of the surface of a material, due to the low inelastic mean free path (IMFP) of electrons in solids. This makes XPS a valuable technique when information about the elemental composition and chemical nature of the surface of a material is needed.

2.4.4.1 Operating principle

In XPS a sample is irradiated with a beam of monochromatic X-rays at energies dependent on the emission source (i.e. Mg Kα 1253.6eV). The sample absorbs the X-ray photons and emits photoelectrons from its core-shell structure. 1-10μm is the typical penetration depth of an X-ray photon with the energy of 1000eV, generating photoelectrons in materials up to this depth. However, a limiting factor to the flux of photoelectrons that make up the XPS signal is the IMFP in a material. IMFP is the distance a beam of electrons can travel before its intensity is reduced by $\frac{1}{e}$ of its original value, and is defined by equations 2-11 and 2-12 below.

$$\gamma_E = \frac{143}{E^2} + 0.054 \cdot \sqrt{E} \qquad \textbf{2-11}$$

Where γ is the mean free path, d is the distance travelled in the material and E is energy.

$$d = ln\left(\frac{I}{I_0}\right) \cdot \gamma_E \qquad \textbf{2-12}$$

As shown in equation 2-11, the IMFP is independent of the material and only dependant on the energy of the beam of electrons. This dependence gives rise to the to “the universal

curve" that describes the penetration depth of electrons as a function of energy, shown in Figure 2-8.

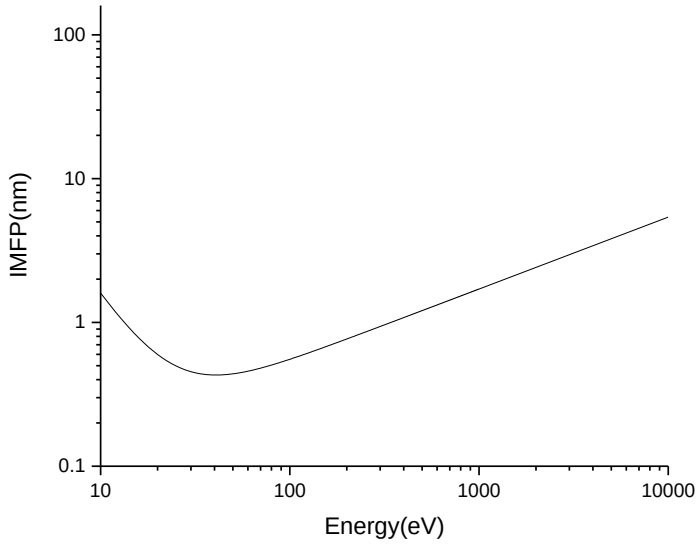

Figure 2-8-Graphical representation of the IMFP of electrons, based on equations 2-11 and 2-12

Figure 2-8 shows, over a range of 1000-1500eV, the IMFP of inelastically scattered electrons is approximately 1-2nm. This means the majority of the signal in XPS comes from the first couple of atomic layers of materials making it a very surface-sensitive technique.

After escaping the material, electrons have a kinetic energy described by equation 2-13.

$$KE = hv - BE - \emptyset_s \qquad \textbf{2-13}$$

Where KE is the kinetic energy of the photoelectron, hv is the energy of the incident photon, BE is the binding energy of the atomic orbital of the atom the electron originates from and $\emptyset_s$ is the sample work function. The binding energy is the difference in energy between an energy state in a material and its Fermi energy. The work function $(\emptyset_s)$ of a sample can be thought of as an energy barrier that prevents an electron at the Fermi level from escaping into free space. The two main components of this energy barrier are the bulk component

and the surface component. The bulk component is caused by the density of states in a material. The surface component is due to an additional potential step caused by the redistribution of charges at the surface of a material.

When a sample is connected electrically to a spectrometer, the Fermi levels of sample and spectrometer align. As a result of the alignment of the Fermi levels, the binding energy of the photoelectrons emitted from the sample can now be referenced to the work function of the spectrometer ($\emptyset_{sp}$). This alters equation 2-13 to equation 2-14.

$$KE = hv - BE - \emptyset_{sp} \qquad \textbf{2-14}$$

Therefore, if the work function of the spectrometer is known, it can be used in conjunction with the kinetic energy of observed electrons to calculate the analytically more significant binding energy.

The simplified experimental set up for inducing emission, collecting and analysing the energy of photoelectrons is shown in Figure 2-9. Firstly, a sample is irradiated with X-rays of known energy causing the emission of photoelectrons. The mechanism of this process is shown in Figure 2-9B by the blue arrow. Another scenario for electron emission is the emission of an Auger electron depicted in Figure 2-9B by the orange arrow. The electrons are then passed through a collector with a variable aperture and an electron lens to focus the electron beam. The electrons then pass through a hemispherical energy analyser to hit an electron detector. The energy of these electrons is calculated by changing the voltage applied to the hemispherical analyser and changing the pass energy.

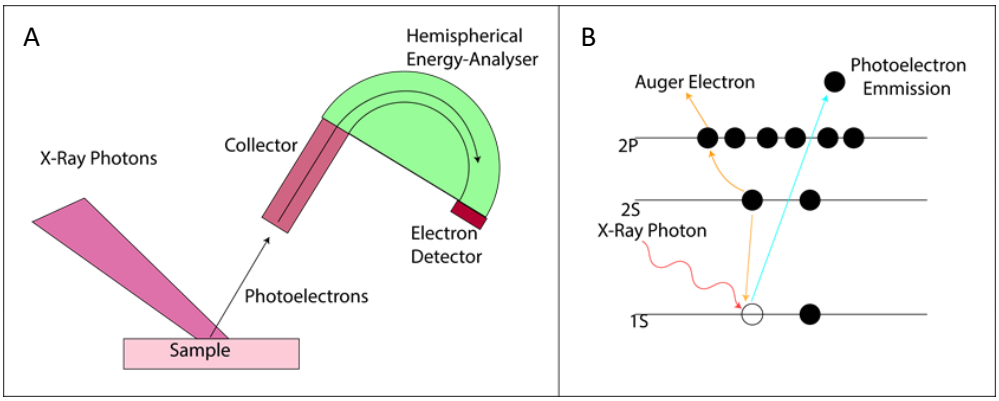

Figure 2-9 (A) Simplified schematic of the main components of an XPS analysis machine. (B) Energy diagram showing the processes for photoelectron emission (blue) and Auger electron emission (orange). Red represents the incident X-ray photon.

Using equation 2-14 described above, this value can then be used to calculate the binding energy of the electron and hence ascribed to a transition from a specific element. XPS is not just useful for determining the presence of specific elements within a sample, it is also capable of differentiating between elements of the same type in different chemical environments. When different elements are bonded to each other, the electron density around the nucleus of the atom is changed. This disruption to electron density can cause shifts in the binding energy of core electrons which, along with tabulated values, can be used to determine the specific types of element the element under investigation is bonded to. Shifts in binding energy are also true for different crystal structures of the same material, such as Iron Marcasite and Iron Pyrite. Both have the chemical structure FeS_2, however, they have different bonding structures and hence different electron densities around the nuclei of the atoms that make up their structure. As the binding energy is also sensitive to the coordination chemistry of elements, it may also be used to detect the presence of surface states in the material.

2.4.4.2 Sample preparation

Samples for XPS need to be mounted in such a way as to avoid surface charging. Nanoparticles from a synthesis are drop-cast onto carbon tape which is adhered to a Silicone (Si) substrate which is then attached to an XPS sample plate. For the analysis of FeS_2 thin films on ITO substrates, the electrode was attached directly onto an XPS sample holder, and a tantalum strap was welded to the sample plate across the sample.

2.5 Inductively coupled plasma-optical emission spectroscopy (ICP-OES)

ICP-OES atomises a liquid solution and injects it into an Argon (Ar) plasma. The elements in the solution are excited in the plasma, and the optical emission from the subsequent decay is observed. This spectrum is compared to emissions from solutions with known concentrations of different elements. From this, it is possible to determine the relative concentration of different elements in a solution. All ICP-OES measurements were performed using the chemistry sample analysis service at the University of Liverpool.

2.5.1 Sample preparation

To avoid nanoparticle solutions blocking the capillary tubing in the ICP-OES, the samples need to be digested in acid before submission for measurement. FeS_2 thin film electrodes were prepared by digesting the active electrode material in Piranha solution overnight. This solution was diluted to 5% acid in ultrapure water before submission. Quantum dot samples were first dried under vacuum before being digested in Piranha solution for five minutes and then diluted to 5% acid in ultrapure water for submission.

2.6 Gas chromatography-thermal conductivity detector (GC-TCD)

Gas chromatography is a method for separating out a mixed gaseous phase into its constituent parts. Here, only the implementation of gas chromatography used in this thesis is described. When a sample is injected into the gas chromatograph, a “carrier gas”, in the case of this thesis Ar, pulls the injected sample through a column. Inside the column is a “stationary phase” of material. Gasses in the sample interact with this phase causing them to elute at different rates, known as the retention time (RT). After the sample is separated out into different gasses, these gasses pass separately into the TCD. There are two essential principles in play for the detector as shown in Figure 2-10. Firstly, the TCD contains Tungsten filaments that are heated up to approximately 250°C at R_3 and R_4. When a gas elutes from the column into R_3, the change in thermal conductivity caused by the gas results in a temperature change, in turn changing the resistance of R_3. Due to this change in resistance, the resistors, in the form of a Wheatstone bridge, output a voltage. This voltage output changes with the amount of gas present and therefore can be used, if calibrated, to determine the exact molarity of gas in a sample, down to ppm concentrations.

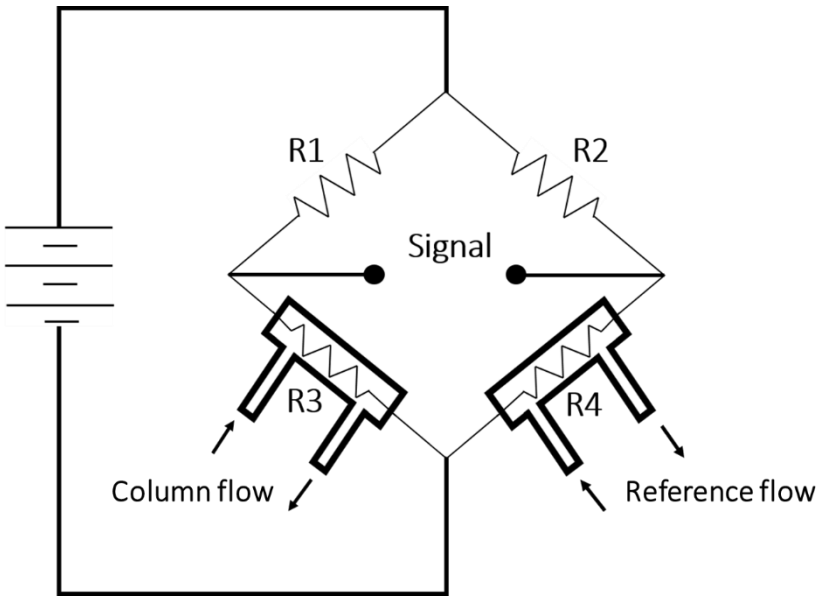

Figure 2-10-Simple schematic of a TCD in a GC employing a Wheatstone bridge circuit.

2.7 Spin coating of FeS_2 thin films

A dynamic spin coating method was used to prepare the FeS_2 nanoparticle thin films. 200µL of concentrated (50mg/ml) FeS_2 solution was dynamically deposited from a pipette onto an ITO film, spinning at 2000 RPM for 30 seconds, to coat the ITO slide with a rigid wet film of FeS_2 nanoparticles. The RPM was then increased to 4000 RPM to dry the film which resulted in a 100-300nm thick, porous nanoparticle thin film.

2.8 Synthesis of FeS_2 nanoparticles

A hot-injection synthesis modified from [124] was used to synthesise the FeS_2 nanoparticles. A solution of 254mg of $FeCl_2$(Sigma Aldrich 99.999%) was prepared in a three-neck round bottom flask with 10 g of Octadecylamine (Sigma Aldrich, technical grade, 90%) and degassed at 100°C using a Schlenk line. In a separate two-necked flask a solution of 460mg of Sulphur (Sigma Aldrich 99.99%) in 5ml of Diphenyl Ether (Sigma Aldrich Diphenyl Ether, ≥99%, FG) was degassed at room temperature using a Schlenk line. After degassing, both flasks were heated up to 220°C under an N_2 atmosphere and the Sulphur precursor was injected rapidly into the three-necked flask. The system was kept at 220°C for two hours to allow the nanocrystals to grow to the desired size. After completion of the synthesis, the content of the three-necked round bottom flask was allowed to cool to 80°C, and 10 ml of Chloroform was injected. 25 ml of the crude solution was mixed with 20 ml of a 50/50 mix by volume of Methanol and Chloroform and the nanocrystals purified by centrifugal precipitation, at 5000 RPM. The product was then collected in 1.8 ml of Chloroform and 0.2 ml of Dimethylformamide for spin coating, corresponding to approximately 50 mg/ml of nanoparticles in solution.

2.9 Atomic layer deposition (ALD)

TiO_2 was grown using an Oxford Instruments OpAL reactor using Titanium Isopropoxide as the Ti source and water as the co-reactant. Growth was carried out at a growth temperature of 200°C. The Ti source was held in a stainless steel bubbler at 70°C and was introduced into the reactor with the assistance of 50 sccm (standard cubic centimetre/minute) of bubbled Argon. The water was held at room temperature and was delivered using a vapour draw. Samples were loaded and unloaded at a reactor temperature below 50°C. Growth was carried out using 120 cycles of, 1.2 seconds Ti source dose followed by a 10 second purge followed by a 30 ms H_2O dose and then another 10 second purge. All ALD films were grown by Dr Richard Potter at the University of Liverpool Engineering Department.

2.10 Pt deposition

Pt was deposited electrochemically in a three-electrode cell from a solution of 0.1 mM Hexachloroplatinate (H_2PtCl_6) in deionised water at 0.3V vs. RHE for 15 minutes in the dark at pH 3.5[109]. Where an FeS_2 electrode was the working electrode, a Pt wire was used as the counter electrode and an Ag/AgCl (saturated KCl) electrode as the reference. An electrochemically inert tape was used to protect all electrical connections and limit the Pt deposition to a 1 cm^2 section of the electrode. The deposition was limited to this area as it would be the only area of the electrode used for photoelectrochemical experiments.

2.11 Annealing electrodes in different atmospheres

2.11.1 Hydrogen and Nitrogen

Annealing FeS_2 electrodes in Hydrogen and Nitrogen atmospheres was conducted using a Borosilicate purge tube with vacuum-tight seals for purging the headspace. For Nitrogen annealing, the purge gas was initially passed through a liquid nitrogen condenser to remove trace water and Oxygen. The headspace was purged for two hours before heating to 220°C

at 5°C per minute and then holding for six hours before cooling at the same rate. Hydrogen annealed electrodes were annealed at 150°C at a flow rate of 75 ccm of 5% H_2 95% Ar by volume. Hydrogen was flowed through the headspace for two hours before heating at 5°C per minute up to 150°C and then held for one hour before cooling at the same rate. A schematic of the set up for the reaction is shown in Figure 2-11.

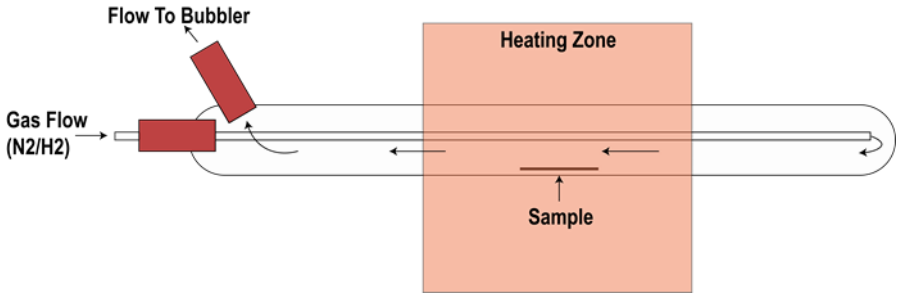

Figure 2-11-Schematic representation of the purge tube designed to anneal electrodes in an inert atmosphere.

2.11.2 Sulfur

Annealing Pyrite electrodes in a sulfur environment followed a method adapted for sulfurising FeS_2 single crystals published by [110]. 0.1 mg of sacrificial FeS_2 nanoparticles, synthesised by the method described in Section 2.7, were inserted into the bottom of a quartz tube. The samples were then loaded 30cm from the end of the quartz tube. The atmosphere was purged with three pump purge cycles using Ar and then evacuated down to 10^{-5} mbar.

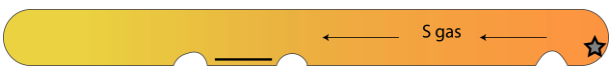

Figure 2-12-Design of a typical vacuum-sealed tube to anneal FeS_2 (P) electrodes in a Sulphur atmosphere. The gradient from orange to yellow depicts a temperature gradient from hot (orange) to cold (yellow). The star represents a Sulphur source.

The purged and evacuated tubes were then loaded into a tube furnace and heated at 2.5°C per minute until the temperature reached 650 °C on the sacrificial pyrite side and 300 °C on the electrode side. This temperature gradient was held for 48 hours before cooling to room temperature at the same rate. Figure 2-12 is a schematic of the reaction showing the temperature gradient. Samples were then retrieved by scoring the tube at the desired point and carefully snapping it open.

3 Synthesis of FeS_2 Nanocrystals

FeS_2 nanostructures have been synthesised using a variety of conventional synthesis routes, from sol-gel synthesis to chemical vapour deposition and hot injection routes. These can synthesise nanomaterials from spherical nanoparticles particles (0D) to sheets (2D), wires (1D) and macroparticles (3D). The following chapter will discuss the synthesis of FeS_2 nanoparticles. The methods outlined in the literature review will be limited to the synthesis of nanoparticles (0D) as this is what is discussed in this thesis.

A synthetic method widely used for FeS_2 synthesis, predominantly 0D structures, is the hot injection synthesis. This has been driven predominantly by solar PV research interests and is by far the most successful method for making FeS_2 nanoparticle inks. The core principle in the context of FeS_2 synthesis is as follows. Flask A contains a Fe salt, e.g. $FeCl_2$, and a solvent and/or a coordinating ligand. Flask B contains Sulphur and/or a coordinating ligand. Both flasks are heated up to an elevated temperature to facilitate the Fe salt to form monomers and the Sulphur to dissolve. Subsequently, one flask is injected into the other, generally flask B into flask A, hence the term, “hot injection”. Following these injection steps, particles nucleate rapidly, and the reaction is left to allow the nanoparticles to grow to the desired size. The first example of FeS_2 nanoparticles synthesised in this way was by Yu Bi[111]. FeS_2 nanoparticles were synthesised by combining Oleylamine, $FeCl_2$ and Trioctylphosphineoxide (TOPO) in one flask which was heated to 170°C to form Fe monomers and then raised to 220°C. Sulphur was mixed with Oleylamine in another flask and injected into the flask containing Fe. The reaction was allowed to proceed for two hours and nanoparticles collected. This resulted in monodisperse phase pure cubic FeS_2 nanoparticles. Figure 3-1A shows XRD of aliquots from the synthesis collected at zero and six minutes and 3-1B shows Raman spectroscopy at zero, two, four, and six minutes. The XRD shows that after six minutes, the FeS_2 nanoparticles are crystalline and phase pure. Peaks present in the Raman

spectroscopy at zero minutes indicates the presence of amorphous FeS_{1-x}. The Raman spectroscopy peaks at six minutes show the formation of FeS_2, confirmed by XRD (Figure 3-1A). This means the growth mechanism for FeS_2 during reactions in this form go through an intermediate amorphous, FeS_{1-x}, stage which is then subsequently sulphurised.

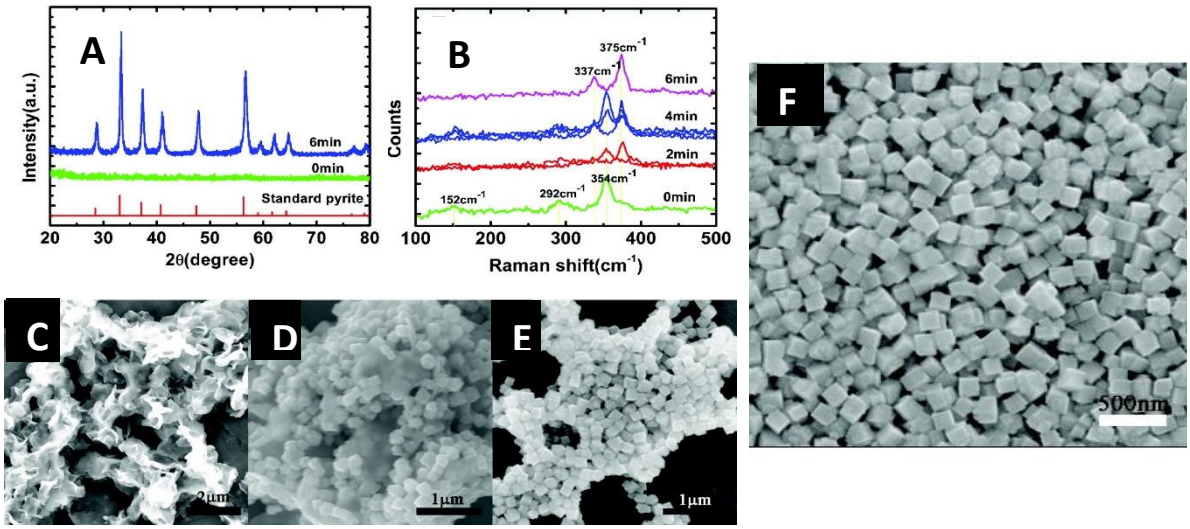

Figure 3-1 A) XRD of aliquots of a synthesis after zero and six minutes B) Raman spectroscopy of aliquots of FeS_2 synthesis after zero, two, four and six minutes, C-E) SEM of aliquots of FeS_2 synthesis after two, four and six minutes respectively, F) SEM of aliquots of FeS_2 synthesis after two hours [111].

Fe solution		**S solution**		**Fe/S molar ratio**	**Temperature of injection**	**Size(nm)**	**Shape**	**Ref**
Salt	***Solvent***	***Salt***	***Solvent***					
$FeCl_2$	OLA/TOPO	S	OLA	1:6	220	60-200	Cubes	[111]
$FeCl_2$	ODA	S	DE	1:3.8	220	70	Sphere	[113]
$FeCl_2$	HAD	S	HAD	1:6	200-220	30-50	Cubes	[114]
$FeCl_2$	DMSO	$Na_2S_2O_3$	DI Water	1:5.2	139	2-9	Sphere	[115]

Table 3-1- Comparisons of different FeS_2 nanoparticle syntheses via hot injection employing different solvents. Oleylamine (OLA), Trioctylphosphineoxide (TOPO), Octadecylamine (ODA), Hexadecylamine (HAD), Dimethylsulphoxide (DMSO), Diphenyl Ether (DE). Adapted from [112].

There are many types of hot injection syntheses for making FeS_2 nanocrystals, the majority of which utilise OLA as the Fe and S solution solvent[111], [116], [117]. Table 3-1 shows the hot injection synthesis utilising different solvent selections.

Another common synthetic route towards FeS_2 nanoparticles is to use a Hydrothermal or a Solvothermal route. The difference between these routes is the solvent used; Hydrothermal synthesis uses water as a solvent, whereas Solvothermal uses an organic solvent. Generally, there is a preliminary reaction such as reacting $FeCl_3$ with Diethyl Dithiophosphate Ammonium Salt to form the precursor Iron Diethyl Phosphate. A sulphur source is then added to this in the presence of a surfactant, and the mixture is sealed in an autoclave. In this example demonstrated by[118], the precursor solution is held at 200°C for between 4-48 hours in an autoclave. Table 3-2 summarises the key parameters for Hydrothermal and Solvothermal reactions for the synthesis of FeS_2 nanocrystals. One of the most important factors in synthetic routes of this type is the surfactant as without it, nanoparticles formed in reactions would aggregate to form microparticles.

Method	Fe source	S source	Surfactant	Reaction temperature(°C)	Reaction time(hr)	Size(nm)	Shape	Ref
Hydrothermal	$FeCl_3$	Diethyl Dithiophosphate Ammonium Salt	CTAB	200	4-28	150	Cubic	[118]
	$FeCl_2$	S powder	Gelatin	200	48	20	Spheroid	[119]
	$FeCl_3$	Na_2S	PEG-400	120	48	10-100	Spheroid	[120]
Solvothermal	$FeCl_3$	S powder	DMF	190	3-22	5.5	Spheroid	[121]
	$FeCl_2$	Sulphur powder	PVP	180	-	14-18	Spheroid	[122]
	$FeSO_4$	$Na_2S_2O_3$	N/A	200	-	20-500	Spheroid	[123]

Table 3-2- Table showing key metrics for Solvothermal and Hydrothermal synthesis of FeS_2 nanoparticles. Hexadecyltrimethylammonium Bromide (CTAB), Polyethylene Glycol (PEG), Dimethyl Formamide (DMF), Polyvinyl Pyrrolidinone (PVP) [112].

A solid-state technique for the formation of FeS_2 nanoparticles is Metal-Organic Chemical Vapour Deposition (MOCVD) and standard Chemical Vapour Deposition (CVD). In reactions like this, vapours of Iron and Sulphur are reacted with each other on a glass or Silicon substrate. Marcasite and Hematite phase impurities are common in these methods [16]. [17] reported production of phase pure Iron Pyrite by reacting $FeCl_3$ and di-tert-butyl disulphide in the presence of CoS_2 as the substrate. The substrate was also varied whilst keeping the conditions the same. A quartz substrate resulted in Haematite and Marcasite phases, whilst Borosilicate resulted only in Marcasite phases. This shows the substrate is just as important as the precursors and reaction temperatures. CoS_2 is a material which has a Pyrite crystal structure and hence may have encouraged FeS_2 formation in a Pyrite crystal structure.

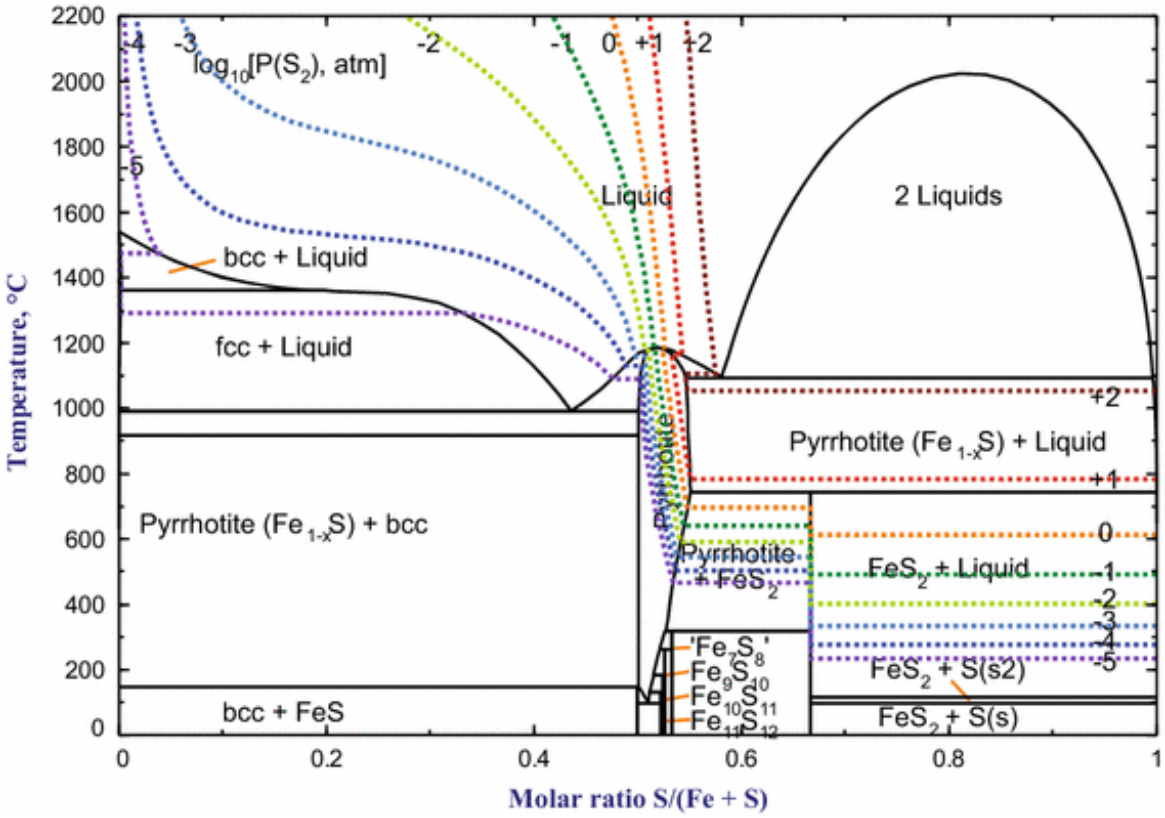

Figure 3-2: Fe-S phase diagram showing the main crystallographic phases of the Fe and S system [175].

The Fe-S system has many crystallographic forms, with the main phases being, Pyrrhotite ($Fe_{1-x}S$), Greigite (Fe_3S_4), Troilite (FeS), Pyrite (FeS_2) and Marcasite (FeS_2). The temperatures of formation and Fe atomic percentage are shown in Figure 3-2. Pyrrhotite is mostly formed under high temperature, low Sulphur partial pressure situations. Greigite, Marcasite and Troilite are formed under low Sulphur partial pressures and low temperature conditions. The main phases can be distinguished from each other using Raman spectroscopy (Figure 3-3) and XRD (Figure 3-4).

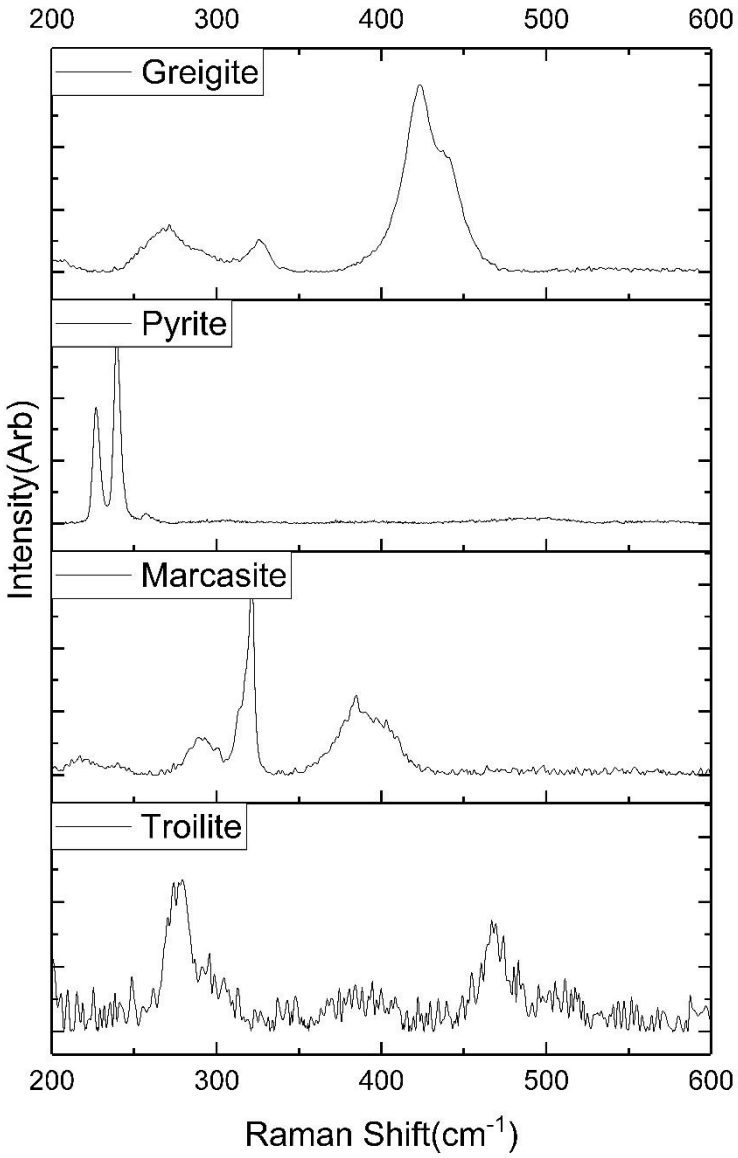

Figure 3-3- Raman spectroscopy of Pyrite, Greigite, Marcasite and Troilite. All reference spectra taken from RRUFF database.

Figure 3-3 and 3-4 show the Raman and XRD signals for the main phase impurities of FeS_2. However, Pyrrhotite is excluded due to the number of crystal structures it has.

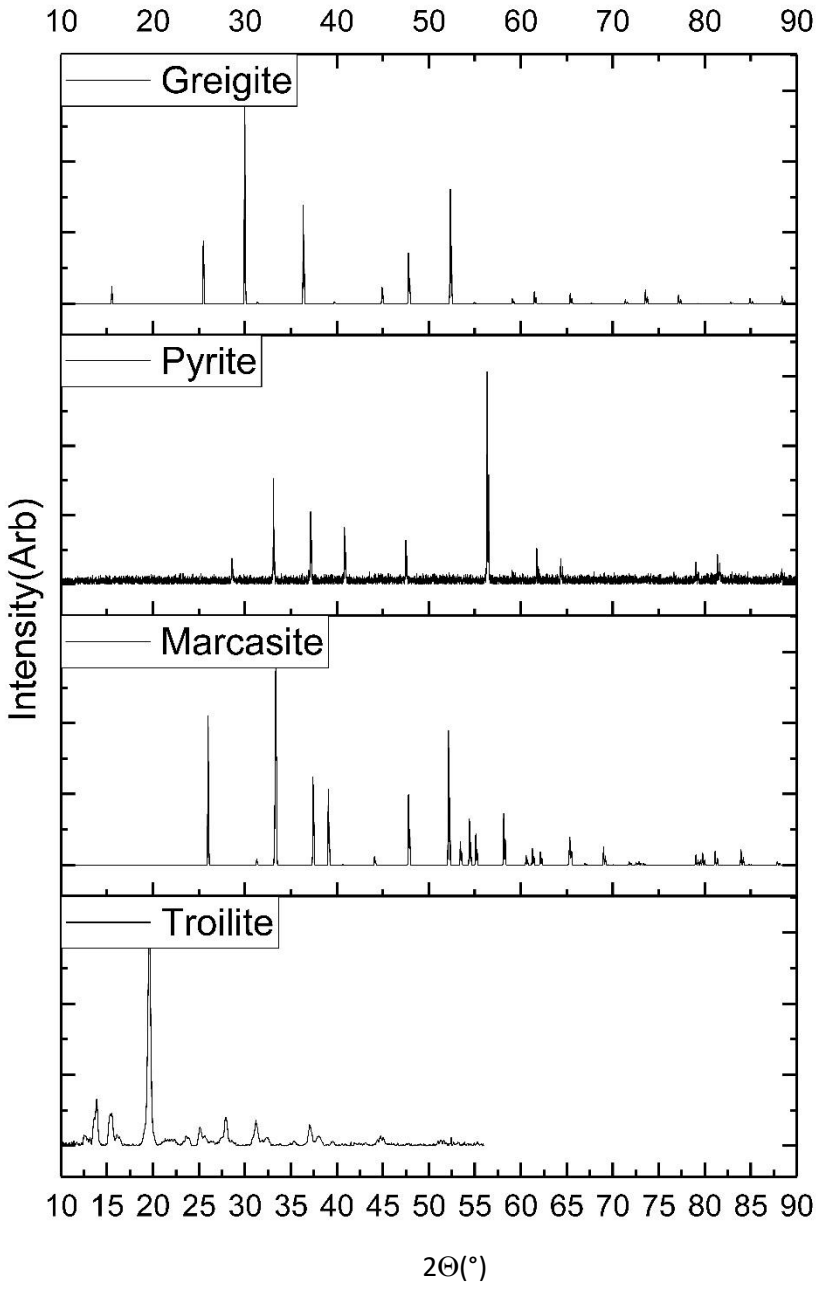

Figure 3-4- Raman spectroscopy of Pyrite, Greigite, Marcasite and Troilite. All reference spectra taken from RRUFF database.

When comparing the signals from the XRD and Raman of Pyrite to Greigite, Marcasite and Troilite, there are distinct differences between all of them. This means determining the phase purity of FeS_2 in Pyrite is relatively easy.

This chapter discusses synthetic methods used to produce 20nm FeS_2 particles used in experiments in Chapter 4, photoelectrochemical measurements in Chapter 5 and also a synthesis for FeS_2 quantum dots. Three synthetic routes are discussed, hot injection, heat up synthesis, and an inverse micelle synthesis. The hot injection synthesis was used to produce 20nm particles, and the heat up synthesis and inverse micelle synthesis to produce quantum dots.

3.1 Synthesis of FeS_2 nanoparticles

Chapter 2.8 contains a detailed method for the synthesis of FeS_2 nanoparticles[124] via a hot injection synthesis route. FeS_2 thin film electrodes presented in Chapters 4 and 5 are all synthesised using this modified synthesis. The modifications made were, increasing the molar amount of Fe and S precursors and increasing the Fe/S ratio. Increasing the molar amounts of precursors, increased the particle yield of the synthesis to make it more efficient at producing FeS_2 nanoparticles. Increasing the Fe/S ratio was done to decrease the chance of forming undesirable Sulphur deficient phases of Iron and Sulphur. Figure 3-5A shows the powder XRD of nanoparticles from the hot injection synthesis, compared to a reference spectrum (AMSCD). The relative intensity of the experimental data is normalised to the reference data represented by the blue bars. This is done by equating the intensity of the (200) peak in both data sets, as it is relatively the most intense peak for the FeS_2 Pyrite phase. This is because it contains the highest density of electrons and hence exhibits the strongest diffraction due to its higher scattering cross-section. The (100) diffraction is not present as the signal interferes destructively with the (200) reflections due to FeS_2s body-centred cubic structure. Comparing the intensity of the (210) peaks with that of the reference data

indicates that there is some preferential growth in this crystal orientation (Figure 3-5A). The XRD shows the nanoparticles are phase pure with an undetectable amount of impurities, the detection limit being approximately 1-2Wt%.

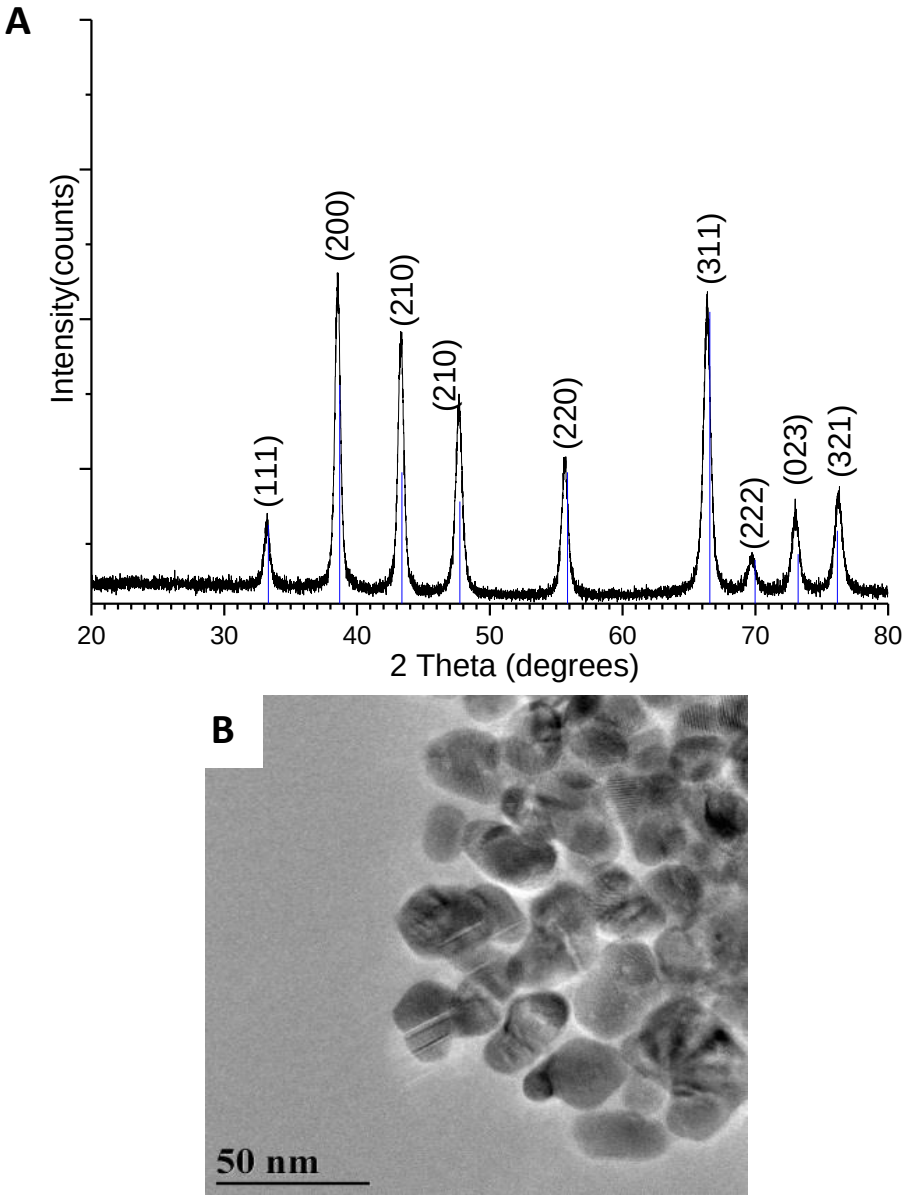

Figure 3-5(A) XRD of a typical FeS_2 nanoparticle synthesis, labelled with crystal orientations and reference bars in blue. (B) Transmission Electron Microscopy of FeS_2 nanoparticles retrieved from a hot injection synthesis.

Figure 3-5B shows a TEM image of FeS_2 nanoparticles retrieved from a typical hot injection synthesis. The aggregation of nanoparticles on the Carbon film coated Copper grid makes large-scale statistics on nanoparticle size difficult. However, the average nanoparticle size can be determined by manually measuring individual nanoparticles. The average nanoparticle size using this method was found to be (19±2)nm. The Scherrer equation[125] shown below (Equation 3-1) confirms this, with a value of (15.6±0.7)nm for crystal grain size.

$$\tau = \frac{k\lambda}{\beta Cos(\theta)} \qquad \textbf{3-1}$$

Where τ is the average size of a crystal grain (in this situation a nanoparticle), k is a shape factor which is generally equal to unity, λ is the wavelength of the diffracting X-rays, β is the full-width-half-maximum (FWHM) of the diffraction peak being analysed and Θ is the diffraction angle.

All FeS_2 nanoparticle films presented in Chapters 4 and 5 are prepared using nanoparticles synthesised with this method.

3.2 Synthesis of FeS_2 quantum dots

One of the main problems with FeS_2 as a material for Hydrogen generation is the alignment of its conduction band minimum, relative to the Hydrogen reduction potential in H_2O at pH 7. One solution to this, is to apply a potential to make up the difference in energy. However, another way to solve this problem would be to shift the conduction band minimum through the alteration of the FeS_2 nanocrystals themselves. This can be achieved via doping, but another option is to decrease the size of a nanoparticle into the quantum confinement region. The size of the particle required to enter this regime is different for different materials, however, for FeS_2(P), it is approximately 3-4nm. Quantum confinement occurs as the charge carrier in a material, excitons in the case of a semiconductor, is spatially confined. This concept is discussed in more detail in Chapter 1.5. Utilising the quantum confinement

effect, a semiconductor's bandgap can be increased from its minimum bulk bandgap. Using this effect, FeS_2s bandgap can, with a suitable synthesis, be varied from 0.95eV to 2.4eV. This shift in the bandgap for FeS_2 would make it possible to drive a Hydrogen evolution reaction without the need for an applied bias. In addition to this, it would also be possible to deposit thicker layers of protective overlayers on FeS_2 photoelectrodes, which would make the electrodes more stable.

3.2.1 Heat-up synthesis

A candidate for a possible quantum dot synthesis was determined to be a heat-up synthesis published by [115] but required modifications to produce nanoparticles less than 4nm in diameter. The ligand to Fe molar ratio was increased, as increasing the ligand concentration in a reaction has been reported to reduce the size of nanoparticles obtained from a synthesis [126]. The synthesis implemented a heat-up method for the reaction and is a non-injection synthesis. In a synthesis of this type, precursors are mixed in a relevant solvent and then heated to induce monomer formation and subsequent nucleation and growth. Compared to a hot injection method, a heat-up synthesis does not have the disadvantages of mixing time and challenging temperature control. One difficulty with a heat-up synthesis is that it is more difficult to separate the nucleation and growth steps [127], something which is considered to aid mono-disperse nanoparticle growth. However, with careful selection of precursors, it is possible to achieve this. For these reasons, a modified heat-up synthesis was selected.

The materials used in the synthesis were $FeCl_2{\cdot}4H_2O$ and $Na_2S_2O_3{\cdot}5H_2O$(STP) as Iron and Sulphur sources, respectively. The solvent for the synthesis was Dimethyl Sulfoxide (DMSO), and the ligand was Thioglycolic Acid (TGA). The method for the synthesis required additional steps to those published in the original literature[115]. The $FeCl_2{\cdot}4H_2O$ was mixed with DMSO and TGA and degassed via the freeze-pump-thaw method to completely remove Oxygen. In the freeze-pump-thaw method, a sample is frozen before a vacuum is applied to degas the

sample. After 30 minutes, the sample is purged with inert atmosphere as it is allowed to thaw. This process is then repeated at least three times. This is a method for degassing volatile solvents. After degassing, the STP was dissolved in water and degassed with Argon by bubbling for 30 minutes. The STP was then added dropwise, one drop every 30 seconds, to the three-neck flask. The slow addition was necessary as the precursors reacted exothermically causing a temperature rise and if the temperature rose above 20 °C at this stage, black precipitates, which are not FeS_2, form. To regulate the temperature, the three-neck flask was routinely rubbed with Acetone, which dissipates heat through evaporation. After the STP was completely added, the temperature was increased to 139 °C and refluxed for two hours. Upon completion of the reaction, the heating mantle was removed, and the solution allowed to cool to room temperature.

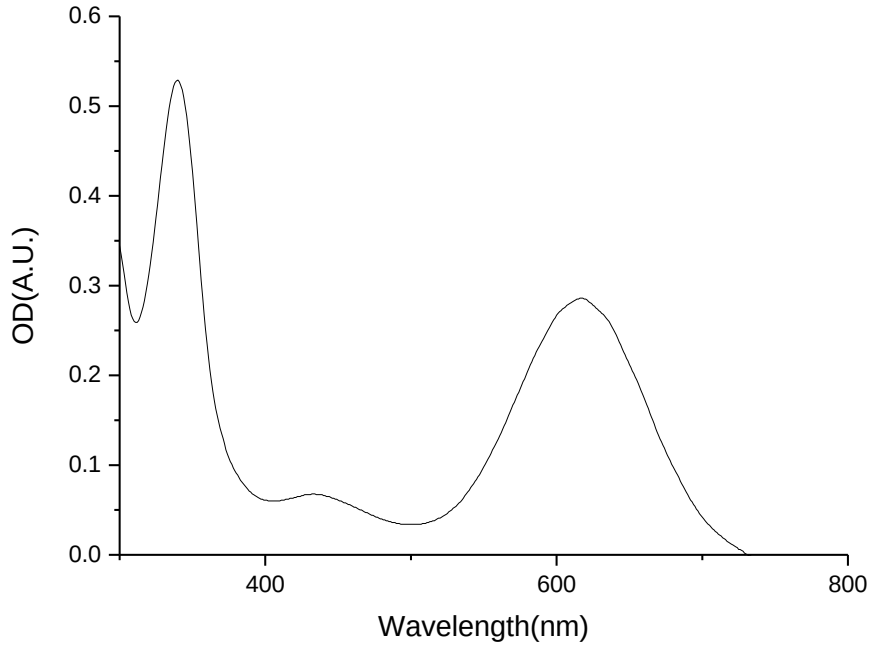

Figure 3-6- UV-Vis spectroscopy of a heat up synthesis material diluted in DMSO

Figure 3-6 shows the UV-Vis spectrum of the solution collected from the synthesis diluted in DMSO. The positions of the peaks present in the spectrograph match that of FeS_2 quantum

dots[84]. However, the relative amplitudes of the peaks have changed considerably. In addition to this, the low background contribution indicates that the material is highly dispersed in the DMSO. Unfortunately, unlike in the published version of this synthesis, it was not possible to purify the material via centrifugation as the decreased size of nanoparticles meant they would not precipitate with centrifugal force alone. In addition to this, the decreased size also resulted in an increased sensitivity to Oxygen. This meant long periods of centrifugation were not possible, as was using a non-solvent to aid precipitation. Centrifuge tubes incorporating a membrane to filter out the nanoparticles was also not possible as one that was chemically stable in contact with DMSO could not be found.

3.2.2 Inverse micelle synthesis

Wilcoxon et al. [128] published a paper in 1996 reporting to have synthesised FeS_2 quantum dots using an inverse micelle synthesis. An inverse micelle synthesis utilises a simple precipitation reaction which is spatially confined and stabilised by the micelles. In a “micelle”, oil droplets are stabilised by surfactants with polar head groups and non-polar chains. The non-polar chains form a shell around an oil droplet, and the polar head group stabilises this structure in water. An “inverse micelle” is the exact opposite of this, where a water droplet is stabilised in a non-polar solvent. These inverse micelles can stabilise water droplets as small as 1nm under the right circumstances. The size of the water droplet can be varied by increasing the molar amount of water relative to the molar amount of surfactant. Other variables that affect the size of an inverse micelle are the concentration of surfactant, type of non-polar solvent, the concentration of ions in the polar phase and type of surfactant[129].

Preliminary investigations of the inverse micelle synthesis used Bis(2-Ethylhexyl) Sulfosuccinate Sodium salt (AOT) as the surfactant, ultrapure water as the polar phase, Diethyl Ether as the non-polar phase, Li_2S as the Sulphur source and $FeCl_2{\cdot}4H_2O$ as the Iron

source. To optimise the parameters for FeS_2 quantum dot production, the water to surfactant ratio was varied for different AOT concentrations. Figures 3-7A and B show the results of UV-Vis results of the obtained material from these experiments.

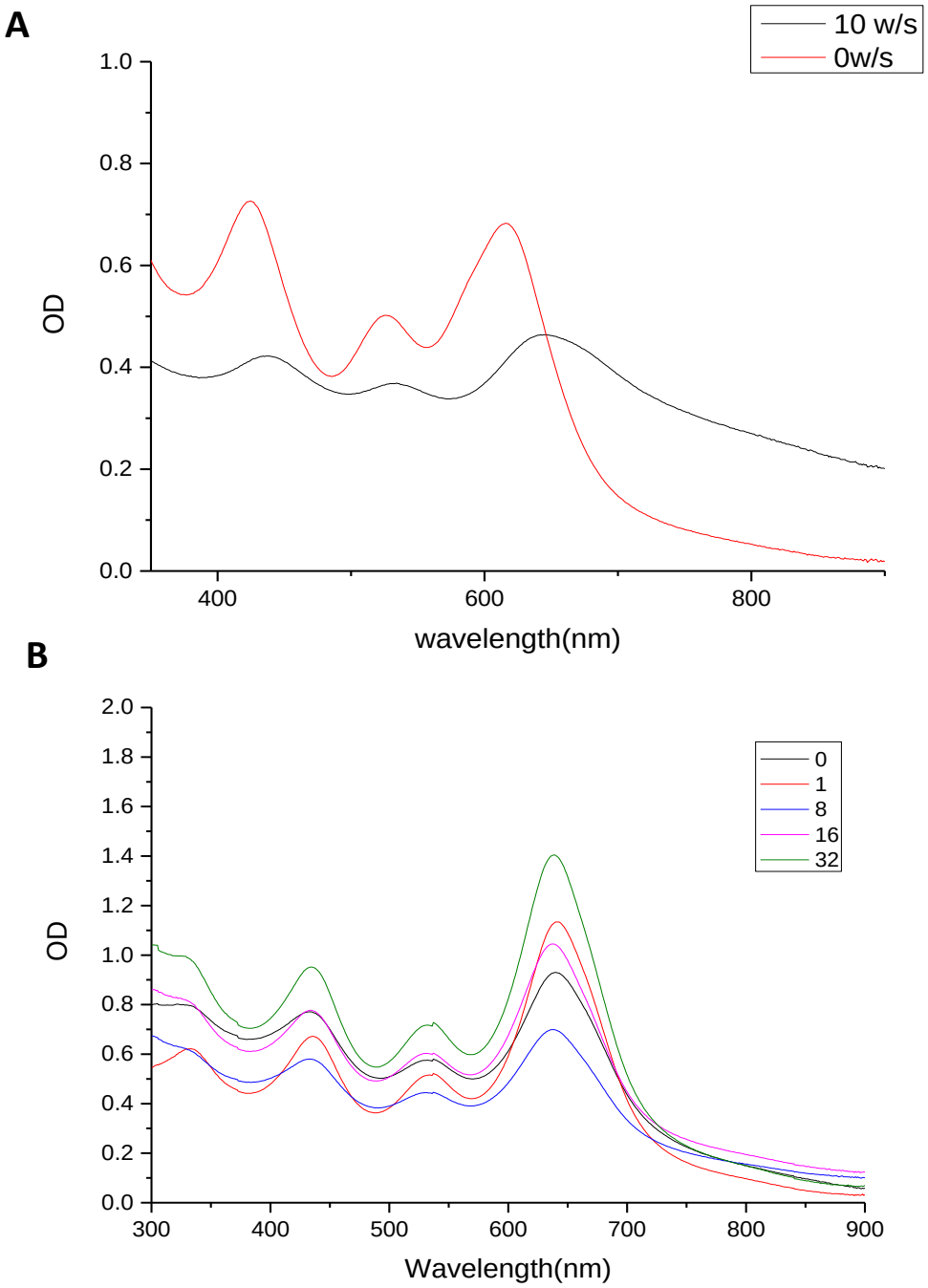

Figure 3-7- UV-Vis spectroscopy of FeS_2 quantum dots synthesised in an inverse micelle synthesis at different water to surfactant ratios (w/s) at a constant surfactant concentration, (A) 0.4M and (B) 0.1M.

UV-Vis results are crucial for characterisation of quantum dot materials because, as explained above, the bandgap and therefore optical absorption will change with particle size. Figure 3-7A shows the results obtained by varying the water to surfactant ratio (w/s) at constant Fe and S concentration at an AOT concentration of 0.4M. The absorption spectrum at 0 w/s matches that of FeS_2 nanoparticles at approximately 3.5nm. Increasing the w/s to 10 has only a slight effect on absorption and therefore little effect on nanoparticle size. Figure 3-7B shows how the absorption spectrum changes for varying w/s at an AOT concentration of 0.1M. There is very little difference in the size of the FeS_2 nanoparticles with a variety of water concentrations at lower AOT concentrations. The concentration of $FeCl_2{\cdot}4H_2O$ within the inverse micelle was also varied while keeping the AOT concentration and w/s constant at 0.1M and 0, respectively.

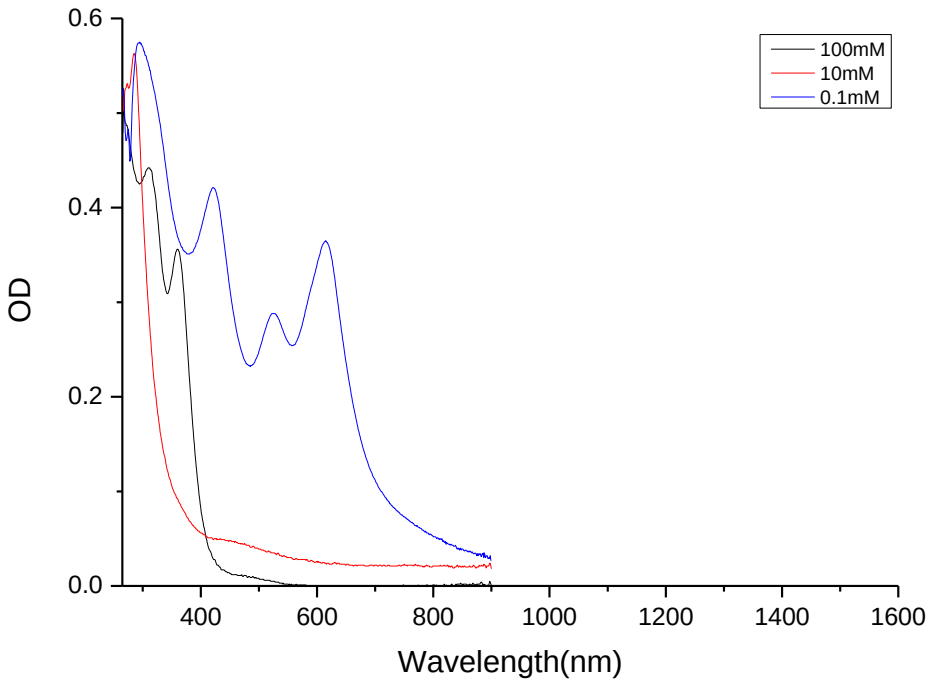

Figure 3-8-UV-Vis spectroscopy of nanoparticles synthesised by inverse micelle synthesis comparing different concentrations of $FeCl_2{\cdot}4H_2O$.

The UV-Vis spectroscopy presented in Figure 3-8 shows that with decreasing concentration of $FeCl_2 \cdot 4H_2O$ the nanoparticles bandgap increases, and therefore size decreases. This is because in this size regime the absorption spectra, and hence the bandgap, is directly related to nanoparticle size. Previous to this, other research has suggested that w/s should have the most substantial effect on size control [129]. However, the UV-Vis spectroscopy corresponds with what would be expected for FeS_2(P) quantum dots. The sizes of the synthesised quantum dots are directly related to the observed bandgap, 0.1mM is approximately 3.5nm, 100mM is 2nm and 10mM is 1nm. However, there were multiple problems with the implementation of the current method. During experimentation, experiments with the same concentrations of precursors and injection methods resulted in different analytical results. This problem proved predominantly to be linked to the temperature inside the glove box, as at times the ambient temperature in the glove box was above the boiling point of the solvent. To improve the control over temperature, the synthesis was adapted to be carried out using a Schlenk line, however, there were difficulties with moving the synthesis to the Schleck line. Firstly, being outside a glove box meant the water content of the Diethyl Ether could not be kept below 5ppm. Secondly, degassing the solvents was also now necessary. Due to the boiling point of Diethyl Ether, it cannot be dried and degassed in a vacuum. It can also not by sparged by bubbling Argon through, as it would evaporate at an unknown rate and affect the concentrations of dissolved precursors. The oil phase was therefore changed to Octane, whose higher boiling point made it more suited for use with Schlenk line techniques. The method for a typical synthesis is as follows. AOT was added to 50ml of Octane to make up a 0.25M AOT inverse micelle solution. The solution was stirred for 20 minutes until the AOT was fully dissolved in the Octane. The solution was then degassed using freeze-pump-thaw techniques. After degassing, 500µl of the degassed 0.1M $FeCl_2$ solution was injected into the three-neck flask. The solution was stirred vigorously overnight to allow for the uptake of the $FeCl_2$ solution into the micelle. After this, 500µl of the degassed 1M Li_2S solution was added

dropwise to the inverse micelle solution. The precipitation reaction proceeded for two hours until all the Fe was used up. The sample was purified by first precipitating the nanoparticles from the solution by injecting a 50/50 mix of Acetone and Methanol. The precipitated nanoparticles were then transferred via a cannula to a degassed centrifuge tube and washed with degassed triple distilled water, using a centrifuge. The sample was then dried under vacuum for two hours to obtain the sample as a powder and analysed using UV-Vis, TEM, XPS and Raman. Figure 3-9 shows the Sulphur 2p region of an XPS measurement of the synthesised FeS_2 quantum dots. The model used for the component analysis of the 2p region is the same as that developed in Chapter 4 to analyse the bulk nanocrystals. The peaks at binding energy of 162.6 eV and 161.3 eV correspond to states where an Fe atom in the top atomic layers of the nanocrystal is bound to a single Sulphur atom. The peaks at 163.1 eV and 161.7 eV correspond to the states of Sulphur bound to Sulphur but under-coordinated by an Fe atom. The broad feature at 163.7 eV corresponds to that of elemental Sulphur bound to the Pyrite crystal lattice. This could either be Sulphur which has had an electron donated to it by a departing Sulphur atom, or Sulphur not coordinated at all by Fe. Finally, the peaks at 162.3 eV and 163.5 eV correspond to that of bulk-like FeS_2 in Pyrite crystal structure. As would be expected for quantum dots, the majority of the signal comes from the surface states. The signal corresponding to the Pyrite bulk is buried below these surface state signals.

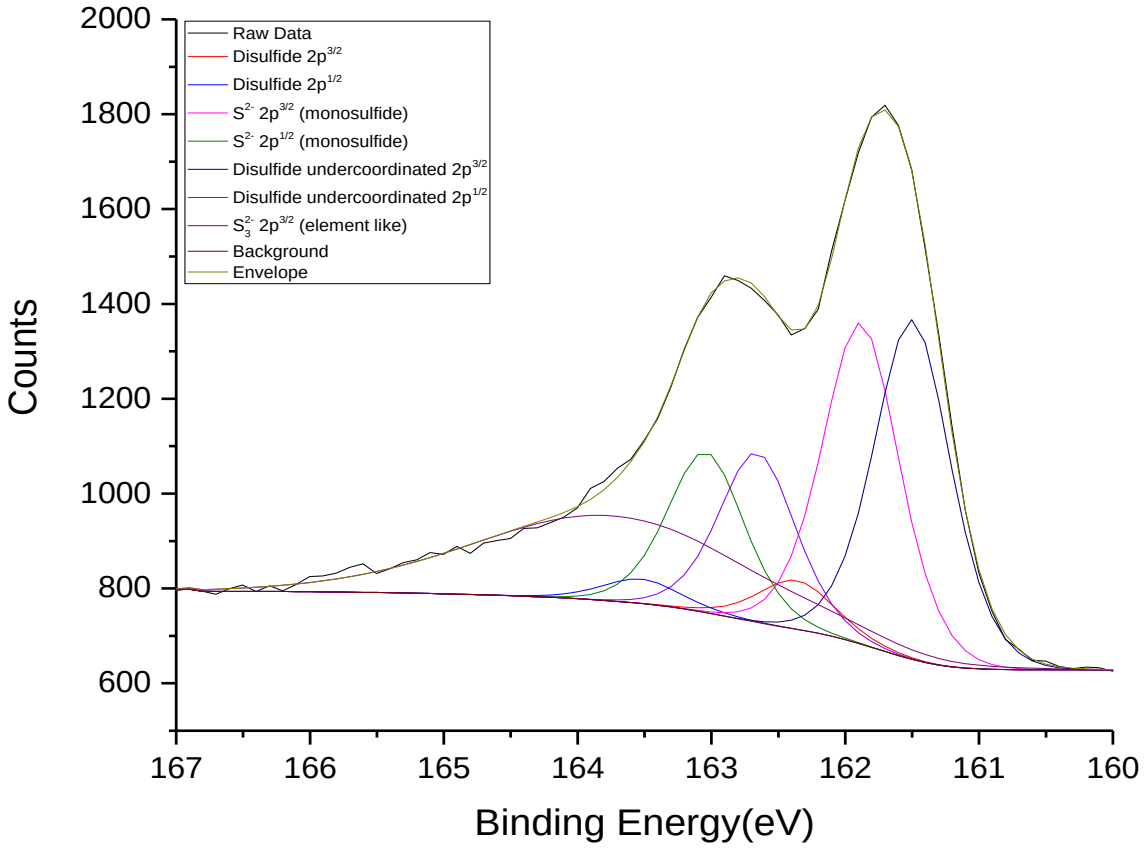

Figure 3-9 XPS spectrum of Sulphur 2p region of FeS_2 quantum dots synthesised with an inverse micelle synthesis using a Schlenk Line.

Figure 3-10 compares the Raman spectroscopy of the FeS_2 quantum dot powder from the inverse micelle synthesis with a bulk sample. The vibrational states associated with the bond vibrations in FeS_2(P) are still present, however, they have been shifted to a higher energy. This shift is an effect of the quantum confinement of the phonons in the crystal structure. However, as the transitions uniformly shift to higher energies the relative separation of the peaks remains the same. The phase purity is also evident due to the lack of peaks corresponding to Marcasite or any other Fe-S stoichiometry.

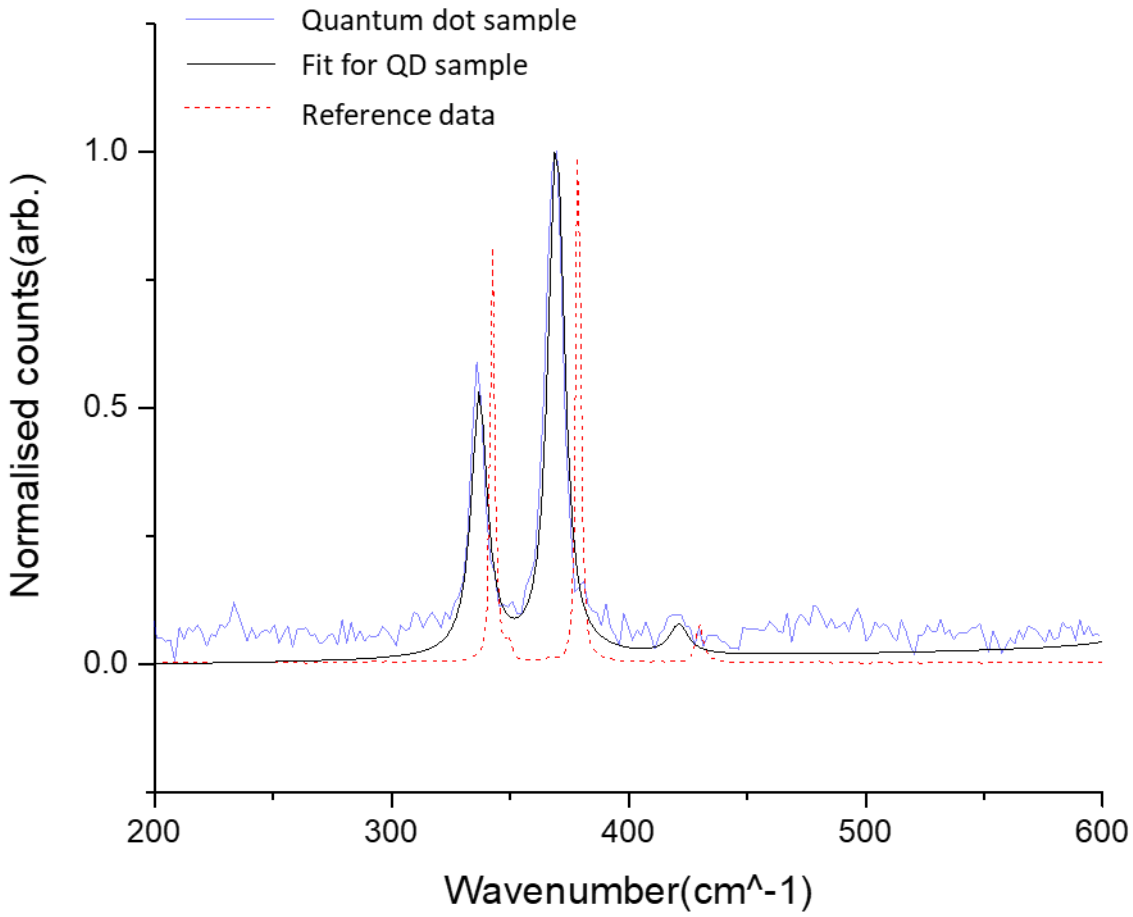

Figure 3-10 Raman spectroscopy of sample collected from FeS_2 inverse micelle synthesis compared to a bulk standard.

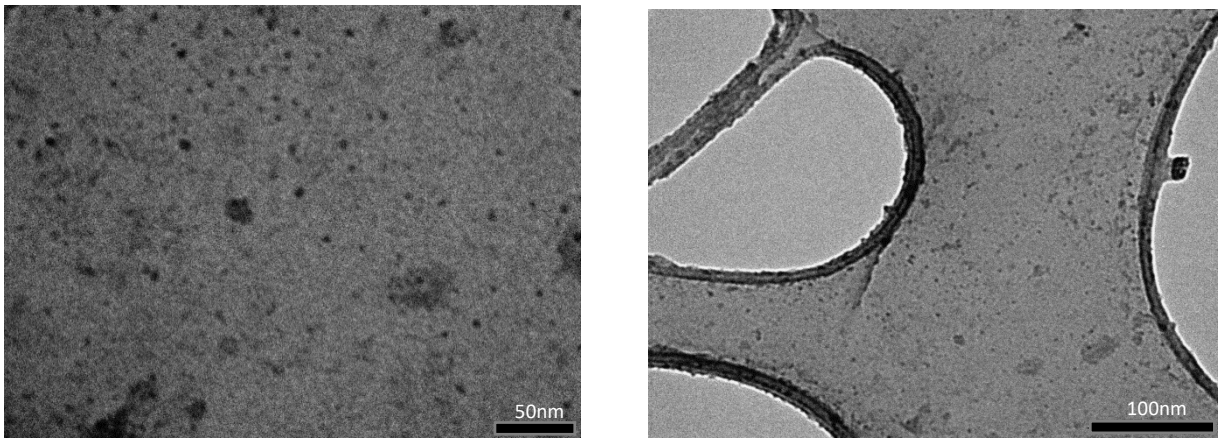

Figure 3-11 Low resolution TEM of FeS_2 quantum dots synthesised by an inverse micelle synthesis using the Schlenk line.

Figure 3-11 shows the TEM of the sample obtained from the inverse micelle Schlenk line synthesis. The TEM sample was prepared by dispersing the FeS_2 nanoparticle powder in ethanol and drop-casting onto a Carbon film coated Copper TEM grid. The images show monodispersed small particulates alongside larger pieces of amorphous material. The average size of the smaller particulates was (3.5±0.2) nm.

3.3 Future work and conclusions

In this chapter, I have presented the developmental route followed towards a synthesis for FeS_2 quantum dots and have characterised these with XPS and Raman for the first time. The XPS studies of the FeS_2 quantum dots identify a large majority of FeS_2 Sulphur surface states with some bulk Pyrite like structure. This corresponds with what would be expected for Pyrite quantum dots, as nanoparticles of this size would display mostly surface like behaviour.

The two methods for synthesising FeS_2(P) quantum dots presented in this chapter were both successful, although both had some disadvantages. The advantage of the heat-up synthesis method presented was that it could be done as a one-pot synthesis. There were also no mixing regimes to be considered as the solution was homogeneous before heat was applied to start the reaction, unlike a hot injection synthesis. Compared to the inverse micelle synthesis the heat-up synthesis also had a higher yield of Pyrite nanoparticles. However, the solvents used in the synthesis made processing the nanoparticles very challenging. The inverse micelle synthesis whilst more complicated to carry out was much easier to process. Raman results in conjunction with UV-Vis show FeS_2(P) nanoparticles with a bandgap of approximately 1.6 eV. The TEM results show nanoparticles approximately 3.5 nm in size and XPS results confirmed a Pyrite like material which was predominantly surface like. A material with a bandgap of 1.6 eV would make for an almost ideal semiconducting material, for solar

fuels applications, as discussed in Chapter 1.4. A material with this bandgap would have the highest theoretical water splitting efficiency (63.1%).

While Pyrite quantum dots are a promising material for solar water splitting, the major disadvantage is the further decreased stability in the presence of H_2O and O_2 compared to bulk-like FeS_2 nanocrystals. Further work on the inverse micelle synthesis should be directed towards addressing this problem by investigating the growth of core-shell nanostructures. The shell of the nanostructure could consist of a surface passivating overlayer, which would protect the nanoparticles and/or catalyse the desired reaction. This could be achieved via several routes. Firstly, the purified nanoparticles could be reincorporated into inverse micelles and then used as seed particles for a second precipitation reaction[130]–[132]. Alternatively, the nanoparticles could act as seed particles in a hot injection or a heat-up synthesis reaction mechanism. This could also be applied to nanoparticles of different sizes to perform overall water splitting in a colloidal system, in conjunction with a redox couple.

4 Optimisation and Preparation of FeS_2 Thin Films

To experiment with FeS_2(P) thin films, a necessary first step is to optimise their preparation and stability. Phase impurities and chemical and physical stability of the film are three critical variables that, if not controlled, can give rise to misleading results. This chapter, therefore, covers the steps taken to improve physical stability by increasing the strength of FeS_2 thin films adhesion to an electrode surface. Investigations on the effect of Atomic Layer Deposition (ALD) layers and co-catalysts are presented, comparing the electrochemistry of TiO_2 and Al_2O_3 overlayers and a Platinum (Pt) catalyst, to improve chemical stability. The results show a clear improvement to the stability of FeS_2 electrodes with TiO_2 overlayers whilst retaining activity. Another increase to stability is shown with deposition of a Pt co-catalyst. Annealing of FeS_2 thin films in Hydrogen, Argon and Sulphur environments is also investigated. Photoelectrochemical and XPS data of FeS_2 thin films annealed in these environments is also presented as a measure of stability increases. The optimum electrode for stability and activity was found to be one annealed in Nitrogen with a 3nm TiO_2 overlayer and a Pt co-catalyst.

4.1 Optimisation of film deposition process

Preliminary photoelectrochemistry of FeS_2 films, prepared via the spin coating method detailed in Chapter 2.7, on an Indium doped Tin Oxide (ITO) electrode highlighted a critical barrier to further investigations. When immersed in an electrolyte, FeS_2 films immediately began to deteriorate physically, and complete film lift-off occurred after only 30 minutes. The most likely reason for this film lift-off is the poor adhesion of FeS_2 nanoparticles to the ITO substrate due to the ligand shell. After the synthesis, Octadecylamine (ODA) ligands form a ligand shell around the FeS_2 nanoparticles. As this ligand is also the solvent in the synthesis, it is a reasonable assumption that this is a high-density ligand shell. When immersed in a solution, water molecules penetrate the film, wetting the ITO surface and repulsing the ODA

coated nanoparticles. No agitation is necessary for this process to result in complete film lift-off. To prevent this lift-off process from occurring, six methods were explored, as summarised in Table 4-1. If a method resulted in undesirable phases its physical stability was not tested and therefore not all methods have an associated physical stability measurement.

	Deposition method		**Annealing method**			
	MPA functionalised ITO	***As-deposited***	***Vacuum (1mbar)***	***Argon***	***Nitrogen (gas passed through liquid nitrogen condenser)***	***Nitrogen annealed***
Undesirable phases	No	No	Yes	Yes	No	Yes
Physical stability	45 minutes	30 minutes			>3 hours	

Table 4-1: Summary of methods tested to increase the adhesion of FeS_2 nanoparticles to ITO electrodes. MPA is Mercaptopropionic Acid, As-deposited is spin-coated with no additional preparation methods. The annealing methods were in; vacuum, Argon, Nitrogen (passing through a liquid nitrogen condenser) and Nitrogen annealed.

The first method investigated was whether FeS_2 nanoparticles could be fixed to the surface by first functionalising the surface of the ITO substrate with Mercaptopropionic Acid (MPA). MPA has two functional groups, a Carboxylic Acid (R-COOH) and a Thiol (R-SH) group, joined together by an aliphatic carbon chain (R). When the ITO electrode is immersed in a concentrated MPA solution, the adhesion of the COOH group onto the ITO surface is energetically more favourable than the adhesion of the SH group [133][134]. Immersing an ITO substrate would, therefore, result in a substrate with SH groups orientated outwards. Furthermore, when submerged into a solution of FeS_2 nanoparticles, a ligand exchange will occur between the SH and the amine (NH_2) on the surface of the nanoparticles. Following this, a layer of FeS_2 nanoparticles will chemically bond to the surface of the ITO substrate, potentially resulting in better adhesion of further nanoparticles to the substrate and a more

robust film. To coat the ITO substrates with MPA, the ITO surface first needed to be cleaned. The cleaning process consisted of sonication in Acetone for 30 minutes, before being dried with a flow of Nitrogen and then being sonicated again in Propan-2-ol for a further 30 minutes. This cleaning method is done to remove any organic and inorganic matter adhered to the surface from production and storage. Cleaned ITO slides were immersed in a 0.1M solution of MPA overnight to allow for the adhesion of MPA-carboxylic acid groups to the surface. The functionalised substrate is then rinsed with ultra-pure water and dried for film deposition. ATR-FTIR was used to confirm the functionalisation of ITO substrates with MPA. Figure 4-1 shows an IR absorption spectrum of a film functionalised using the above method. Absorption peaks at 2157nm, 2019nm and 1975nm correspond to those of a carboxylic acid molecule adhered to the surface of the ITO substrate.

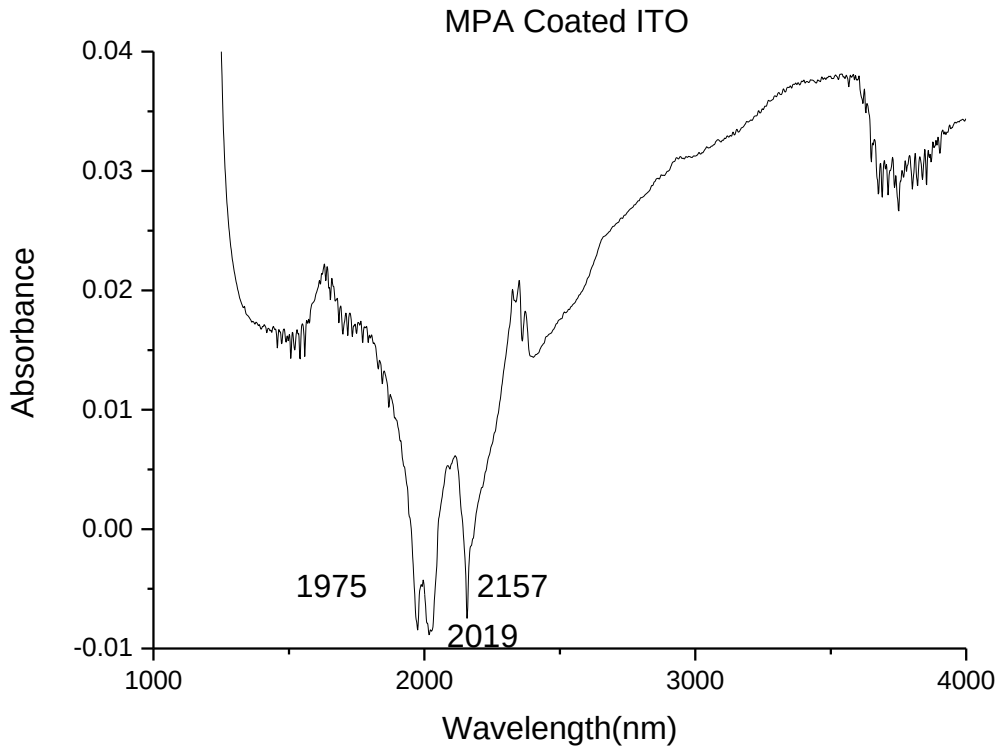

Figure 4-1- ATR-FTIR of MPA (Mercaptopropionic Acid) on ITO electrodes.

The second method is to deposit as synthesised nanoparticles onto the ITO surface and remove the ODA ligands by annealing the thin films in a furnace. This process could have the advantage of, not only improving the physical stability of the films but also, removing the high-density ligand shell that could be an additional barrier to the goal of Hydrogen evolution [135], as the shell can act as an energy barrier to electron transfer. FeS_2 is susceptible to oxidation, especially if there is water present [136]. Two methods were explored to prevent the oxidation of FeS_2 under different annealing conditions, by limiting or removing Oxygen and water contamination from the atmosphere in which the annealing is performed. Firstly, films were annealed in a low vacuum of $1 \cdot 10^{-2} mbar$, in sealed Borosilicate (Pyrex) tubes. Sealing the FeS_2 thin films under vacuum was done using a Schlenk line connected to a Nitrogen supply and an oil pump. A Pyrex tube, closed at one end, was first prepared by melting one end of an open Pyrex tube using an Oxyacetylene (OA) torch. After cooling, a prepared film was inserted down the length of the tube and then a neck was produced using the OA torch, ensuring this was far enough away from the electrode as to not heat the electrode. This neck was made to aid in the sealing of the glass tube. Once cooled, the prepared tube was attached to the Schlenk line using vacuum-tight fittings. The Pyrex tube was then evacuated to $1 \cdot 10^{-2} mbar$ before being purged with Nitrogen. This was repeated three times, to ensure the removal of atmospheric contaminations, and then left under vacuum. After the pump purge cycles, the Pyrex tube was sealed by melting the glass at the neck, using an OA torch until the glass closed upon itself, allowing the tube to be drawn away without the intrusion of the atmosphere within the tube. The electrode within the Pyrex tube, under vacuum, was then annealed in a furnace at 200 °C for 24 hours, increasing by 5 °C per minute from room temperature and cooling down at the same rate.

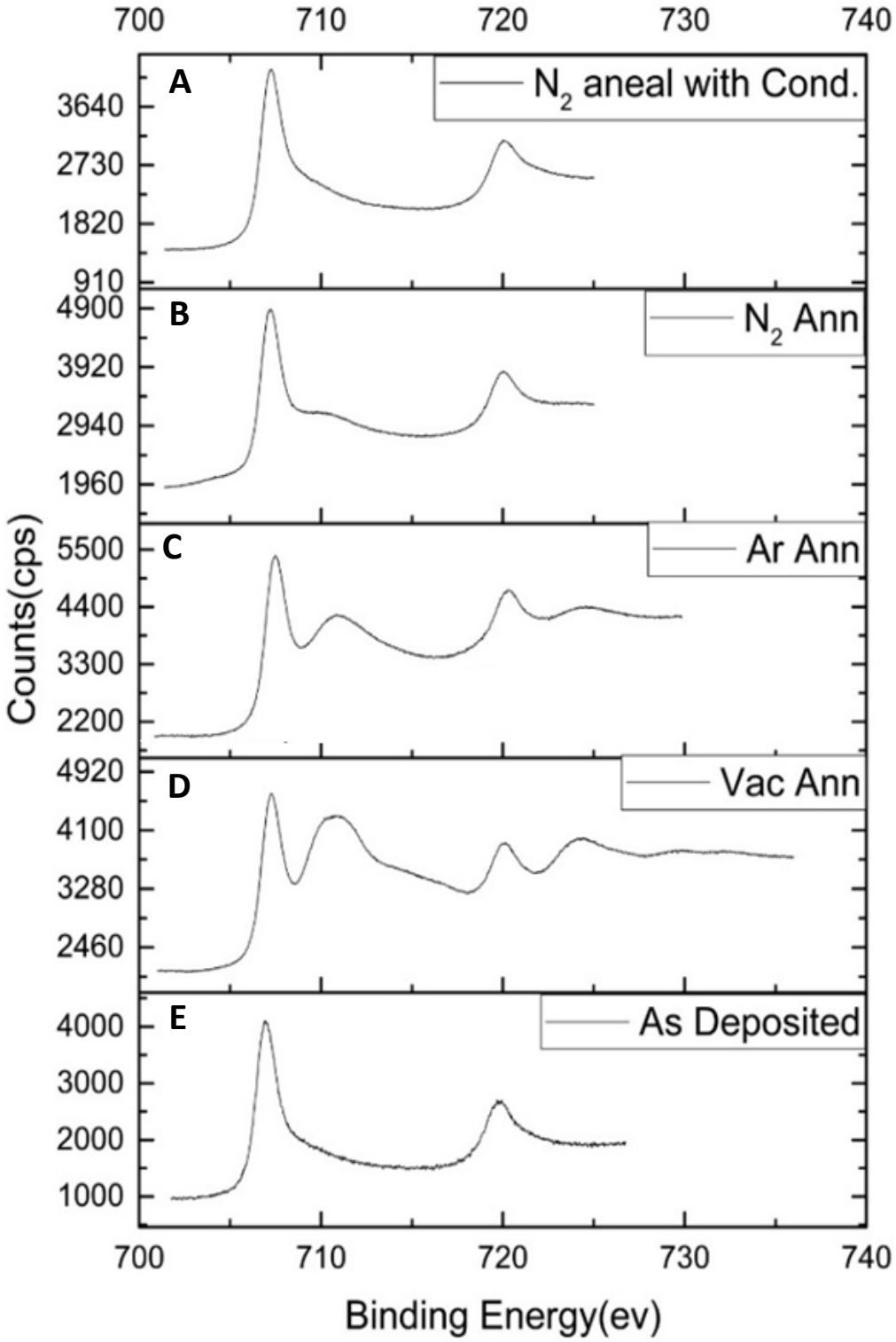

Figure 4-2- XPS of FeS_2 thin films annealed in different atmospheres. (A) Nitrogen atmosphere after passing through a liquid nitrogen condenser, (B) Nitrogen atmosphere, (C) Argon atmosphere, (D) vacuum, and (E) a sample as prepared without any further processing.

Figure 4-2D shows the XPS of films annealed in a vacuum which can be compared to that of films measured on as-deposited electrodes (Figure 4-2E). The sharp peak at 707.15eV corresponds to the binding energy of Fe $2p_{3/2}$ electrons in a Pyrite crystal structure [137]. However, there is a broader peak at 712eV. The larger FWHM of this peak indicates that it comes from Fe atoms in multiple states or amorphous in nature. The most likely candidate for this feature is multiple oxides of Fe in an amorphous structure. Annealing the electrodes in a vacuum has likely caused Sulphur to outgas from the crystal structure, leaving behind elemental Fe [138]. When the electrode has been removed from the vacuum tube, the elemental Fe has then oxidised to form multiple forms of Iron Oxide.

Another annealing method for improving the physical stability of FeS_2 films would be to anneal the electrodes in an inert atmosphere. Argon was the first inert gas chosen as a candidate for the annealing of the thin films, due to its extreme stability. Initally this method involved clamping metal caps at either end of a tube in a tube furnace. The metal caps were clapped with a rubber O-ring between the tube and the cap to seal the inside of the tube. Inlets and outlets present on the metal caps were connected to a supply of Argon, and the outlet was connected to a Silicon oil bubbler. The preliminary annealing step comprised of purging the annealing tube with Argon gas for 1.5 hours before increasing the temperature by 5 °C per minute, holding at 220 °C for six hours, and then cooling at 5 °C per minute. Once this annealing step was finished, the retrieved films had changed from a typical grey/silver Pyrite hue, to a translucent orange. It was determined from this observation that the Pyrite had been oxidised by atmospheric oxygen penetrating a poorly sealed furnace tube. To increase the control over the annealing atmosphere, a purge tube was designed and commissioned in the form shown in Figure 2-11 in Chapter 2.11. To ensure the prevention of atmospheric contamination, all fittings used were vacuum rated with a safe operating temperature up to 400 °C. The working gas entered the annealing cell via a long tube which directed the gas to the end of the tube. The inlet tube, in conjunction with the outlet being

at the opposite end, ensures proper flow of inert gas along the length of the tube without any “dead” flow regions. Following the development of the annealing cell, typical Argon annealing experiments followed the same steps as outlined previously, with the exception of the use of a purge tube rather than the metal caps. Figure 4-2C displays the XPS of a sample annealed in Argon which can be compared to that of a sample taken fresh from a synthesis (Figure 4-2E). The peak in the ‘’As-Deposited’’ sample (Figure 4-2E) at 707.15 eV corresponds to that of Fe $2p_{3/2}$ in an Iron Pyrite crystal structure. The higher binding energy tail from the same peak corresponds to defect states at the surface [139]. While interesting, a full treatment of this surface state argument is discussed in a more appropriate section, later in this chapter (Section 4.3). The second peak at around 720 eV is due to the Fe $2p_{1/2}$ state. A comparison of this spectrum with that of a sample annealed in Argon, as discussed above, shows that after annealing, a broad peak exists at a higher binding energy. This peak can be attributed to Fe in several different states of oxidation [137], along with its doublet. The peak that corresponds to Fe sitting in a FeS_2(P) crystal lattice is still present. This, coupled with the fact that XPS signals come from 3-5nm within the material, means the oxidation is confined to the outermost surface layers. If this were not the case, there would be no observable peak for Fe in Pyrite cyrstal structure in the XPS. For this limited amount of oxidation to occur, the amount of Oxygen or water contamination must be very small. A potential cause of this contamination was likely due to small fractures in the gas lines. To fix this issue, a liquid nitrogen condenser was attached in line with the current gas flow to remove any oxygen and water contamination from the gas lines. However, the temperature of liquid nitrogen is below the freezing point of Argon, therfore the working gas was switched to Nitrogen. Figure 4-2A displays the FeS_2 films annealed in Nitrogen passed through a liquid nitrogen condenser which allows for comparison with films annealed in Nitrogen gas (Figure 4-2B) and as-deposited films (Figure 4-2E). Films annealed in Nitrogen gas passed through a condenser show no increase in any peaks corresponding with Fe bound to Oxygen. Films annealed in

Nitrogen without a condenser however, do show some increase in oxide related peaks. Therefore, the optimal condition for annealing films is under Nitrogen flow with the Nitrogen passing through a liquid nitrogen condenser.

Figure 4-3 is a comparison of how films annealed under Nitrogen passed through a liquid nitogen condenser, MPA attached nanoparticles, and an as-prepared sample, behave photoelectrochemically. Throughout the thesis, any electrode or sample referred to as “as synthesised” or “as deposited” can be defined as being made using nanoparticles from a synthesis which have undergone no further treatment. Samples were prepared as discussed above and used as the working electrode within a three-electrode cell, with Ag/AgCl as the reference electrode and Pt as the counter electrode. The working electrolyte was 0.1M phosphate buffer solution at pH 7. The working electrolyte and the cell were degassed for 30 minutes under Argon flow before every measurement. The as-deposited electrodes lasted the shortest amount of time, with complete film drop off after just 30 minutes. MPA functionalised electrodes dropped off after 45 minutes. Thin film electrodes annealed in Nitrogen gas passed through a condenser lasted the entire 3 hour experiment, and were also the only electrodes to produce Hydrogen in observable quantities. As a result of this experiment, the FeS_2, thin films were stable enough to be measured for an experimentally significant period. As such, all films used following this are prepared by annealing in Nitrogen atmospheres, with the Nitrogen purified by a liquid nitrogen condenser.

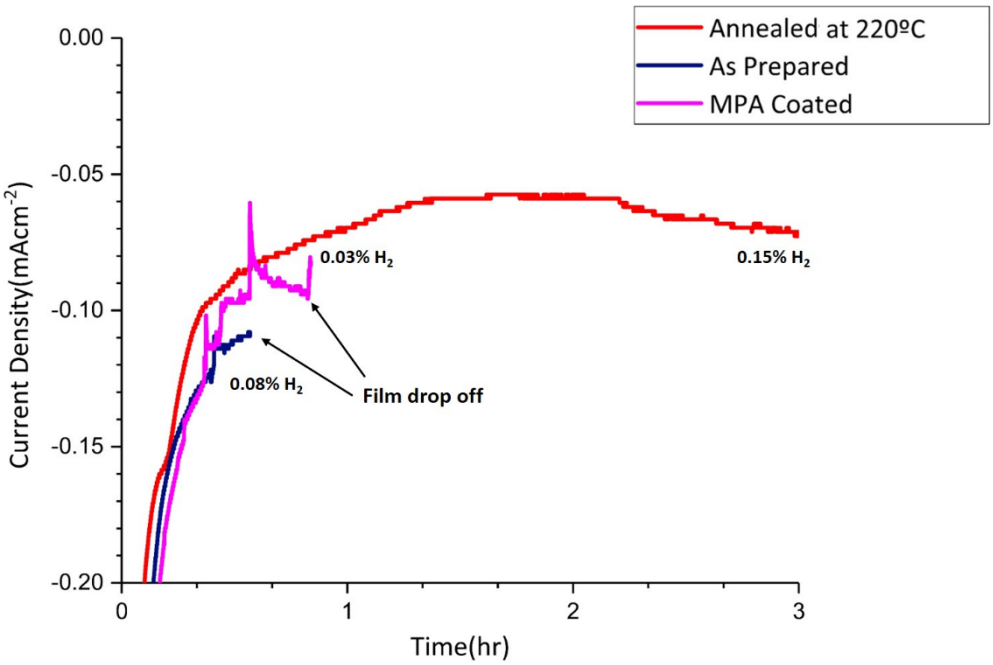

Figure 4-3- Photoelectrochemistry of FeS_2 thin films annealed at 220 °C (red), attached with MPA (pink), and drop cast as prepared (blue).

4.2 Annealing of FeS_2 electrodes

4.2.1 Hydrogen annealing

Substitution of a Hydrogen atom into a Sulphur vacancy (V_s) or reinserting a Sulphur atom could potentially be achieved through a variety of methods. For Hydrogen substitution, it is possible by immersing FeS_2(P) thin films into an H^+ rich environment, namely an acid [140]. However, to avoid unwanted reactions of highly unstable FeS_2 nanoparticles with acid, annealing the nanoparticle films in an Hydrogen atmosphere was chosen. The reaction of Hydrogen with FeS states on the surface of FeS_2 forms FeSH states, which are energetically more favourable [140].

To discern the optimal annealing conditions for FeS_2 in Hydrogen, thin film FeS_2 nanoparticle electrodes were annealed in a 5%H_2:95%Ar_2 atmosphere at 70 sccm in temperatures between 50 °C and 350 °C. Figure 4-4 compares the XRD of the thin films annealed under different temperatures. All diffractograms have been normalised to the intensity of the (200) peaks at 38 °. Samples annealed at 100°C and 150°C, compared to samples annealed at 50°C show a reduction in unwanted contaminant phases. This is notable due to the disappearance of small contaminant peaks found at 34 ° and 35 ° in the other temperature conditions. In addition to this, all diffraction peaks for samples annealed at 100 °C and 150 °C correspond to that of FeS_2 in Pyrite form. Annealing samples at 250 °C leads to the appearance of unwanted phases of Fe and S that correspond to Pyrrhotite[141]. In addition to these unwanted crystal phases, there is also a broad peak between 20 ° and 40 ° that corresponds to amorphous phases. Samples annealed at 350 °C show the addition of a higher concentration of unwanted Fe and S phases with very little of the signal from FeS_2(P) remaining. The exact determination of the predominant phase was difficult due to the large number of peaks present. However, the most likely phase is FeS_{2-x}, as the reaction of FeS_2 with the Hydrogen gas at temperatures above 150 °C is likely to involve Hydrogen reacting with Sulphur to form Hydrogen Sulphide, resulting in undercoordinated Fe.

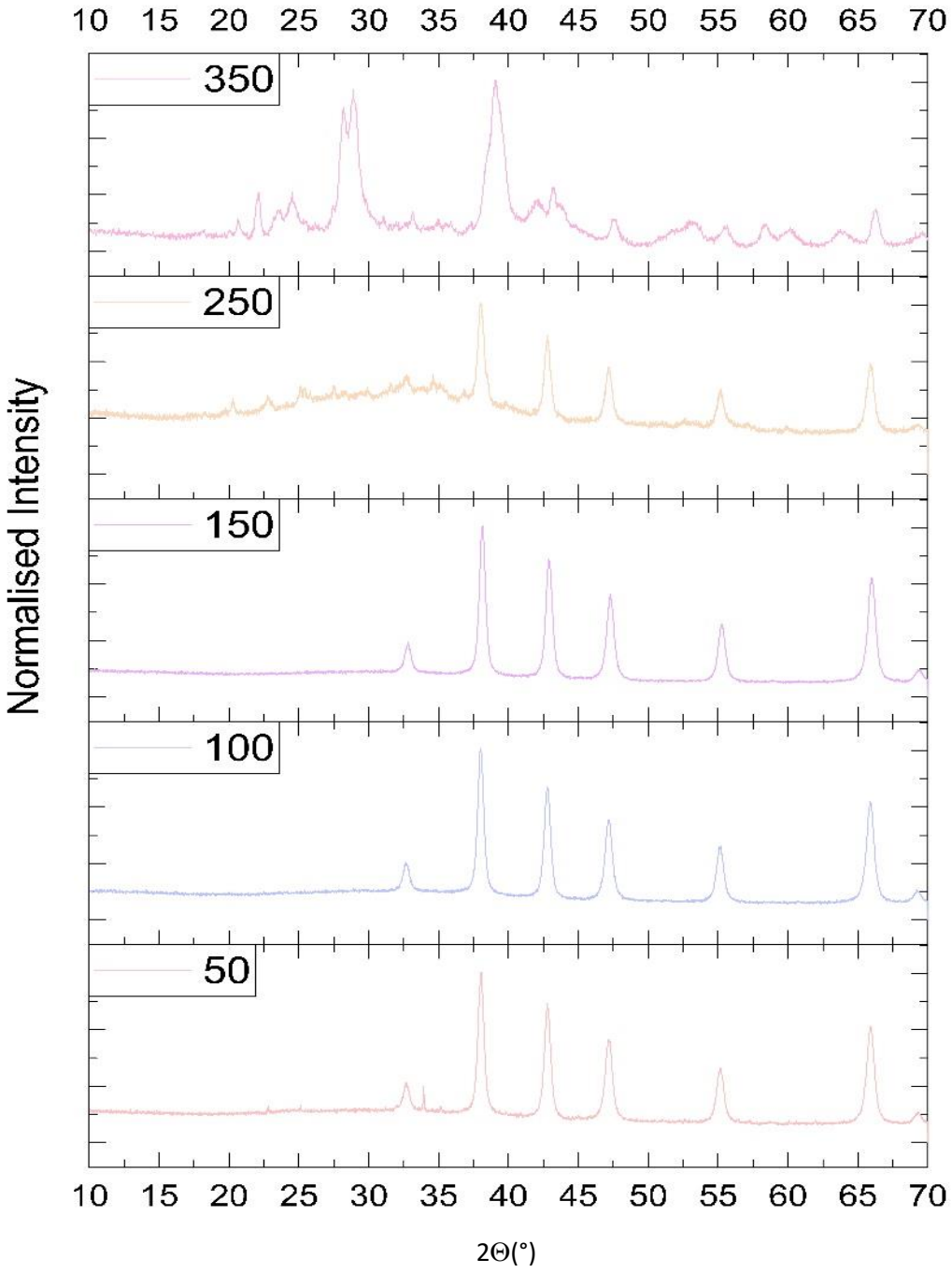

Figure 4-4- XRD of FeS_2 nanoparticle thin films annealed in 5%H_2:95%Ar_2 at; 350˚C (pink) 200˚C (yellow), 150˚C (purple), 100˚C (blue) and 50˚C (red).

4.2.2 Sulphur annealing

To reinsert Sulphur into FeS_2 V_s, it is possible to again immerse thin film electrodes into a solution, this time comprised of a Sulphur source, such as either Ammonium-, Lithium- or Hydrogen Sulphide [142]. However, an annealing process was selected similar to one proposed for repairing FeS_2 single crystal surface defects [143]. A standard Sulphur annealing experiment is described in Chapter 2.11.2. After annealing in a Sulphur environment, however, the ITO transparent conducting oxide (TCO) substrate became electrically insulating. The destruction of ITOs conductivity is due to the passivation of ITOs Oxygen defect sites that are crucial to its conductivity [144]. To find an annealing regime that would result in conductive ITO, blank ITO substrates were annealed in Sulphur conditions with varying amounts of sacrificial FeS_2 as the Sulphur source. The sacrificial FeS_2 was varied from 10 mg to 0.01 mg in order of magnitude step sizes. The result of this was a conductive ITO film at 0.1 mg of sacrificial FeS_2.

4.3 XPS of Hydrogen and Nitrogen annealed electrodes

To understand how annealing in Hydrogen and Nitrogen environments affects FeS_2 nanoparticle surfaces, XPS was performed. This section will present an argument for the differences in defect state density of annealed FeS_2 films, using XPS analysis in conjunction with previously reported models [139].

4.3.1 FeS_2 (as-deposited)

As a control, XPS was conducted on FeS_2 nanoparticles taken directly from a synthesis, as described in Chapter 2.8. The Iron signal in the XPS spectra has a response from the 2p, 2s, 3p and 3s orbitals and the Sulphur 1s, 2p and 2s, with the p orbitals splitting due to spin. However, this work will only focus on the Sulphur $2p_{1/2}$ and $2p_{3/2}$ peaks and the Iron $2p_{3/2}$ peak. The reason for only using one of the Iron 2p peaks is that both 2p peaks contain the same experimental information. However, the lower binding energy peak has a much higher

signal to noise ratio, and therefore is easier to model, as it comes from a state with a greater number of electrons. Furthermore, it is possible to separate the analysis of the two peaks in the doublet due to the large doublet separation. This is not possible for the Sulphur 2p doublet; hence both are discussed.

To minimise the amount of oxidation to the FeS_2 nanoparticles, the material was purified under an Argon atmosphere. Samples were then transferred to the XPS sample loading arm, pumped down overnight and measured the following morning. The same amount of care taken to avoid oxidation, should also be taken to avoid vacuum damage. If a sample is left in UHV for too long, the Sulphur in the FeS_2 crystal structure will begin to outgas, giving rise to anomalous readings. As such, all XPS spectra presented below were collected on samples which spent around the same amount of time (one day) in the UHV chamber.

Figure 4-5 shows a Fe $2p_{3/2}$ XPS spectrum of pristine FeS_2(P) nanoparticles, harvested directly from a synthesis. The peak centred at a binding energy of 707 eV is from fully co-ordinated Iron in an Iron Pyrite crystal structure. If the crystalline quality of the FeS_2 was poor, Fe $2p_{3/2}$ electrons would exist in a broad distribution of energy states around this value. As this is a very sharp and clear peak, it is a testament to the highly crystalline nature of the as synthesised FeS_2 pyrite nanoparticles. The small peak on the lower binding energy side of the bulk Pyrite Fe $2p_{3/2}$ peak is due to a small quantity of elemental Iron. This is possibly due to unreacted Iron from the synthesis, or potentially elemental Iron on the surface of the nanoparticles. The surface states of FeS_2 all exist at a higher binding energy to that of the bulk Pyrite Fe $2p_{3/2}$ peak, existing in two oxidation states Fe^{3+} and Fe^{2+}.

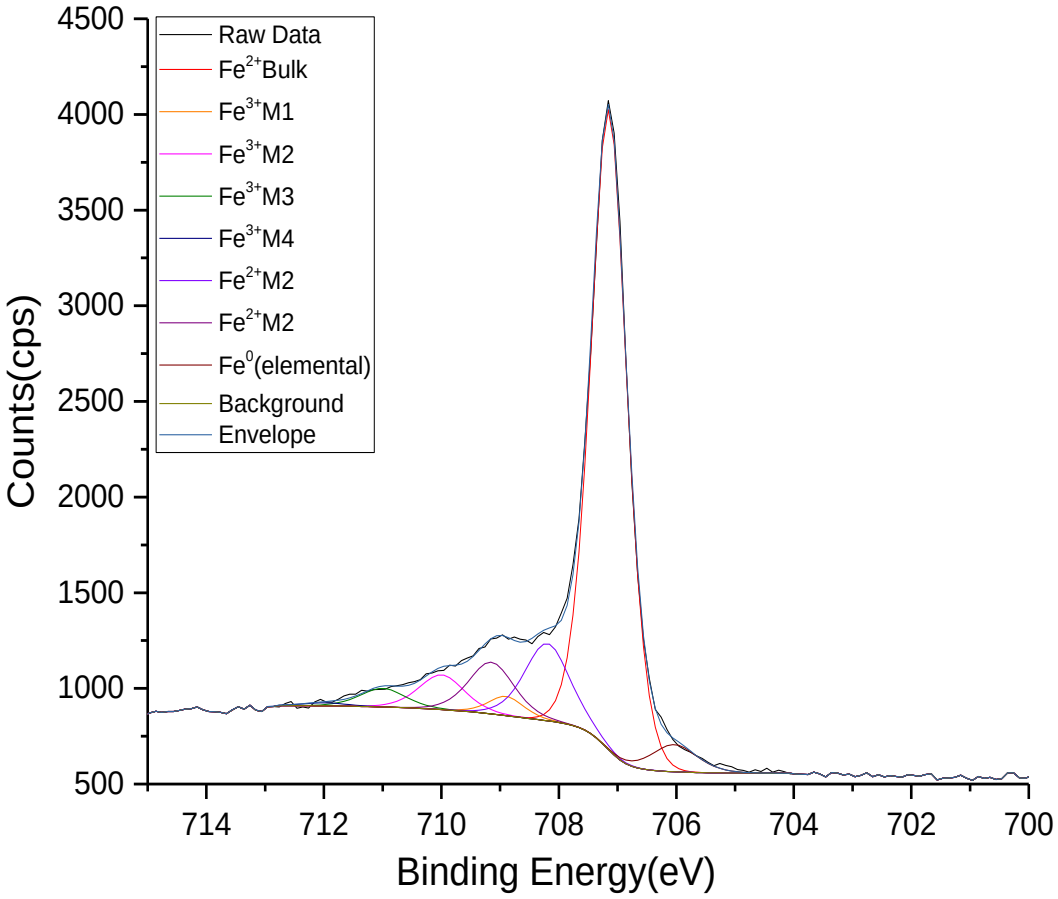

Figure 4-5 Fe $2p_{3/2}$ region of an XPS spectrum taken of pristine FeS_2 nanoparticles taken directly from a synthesis.

The result of the presence of these defect states is a broad shoulder at the higher binding energy side of the bulk Fe $2p_{3/2}$ Pyrite signal with multiple features. The oscillating nature of this broad feature indicates that it consists of signals from multiple energy states. One of the contributions to the surface state signals must come from under co-ordinated Fe^{2+} states on the surface, bonded to disulphide (Sulphur dumbbells) and monosulphide due to Sulphur defects. These states are at a higher binding energy to that of bulk Fe^{2+}, due to the reduction in nuclear screening from the removal of ligands at the surface [139]. The structure of the

signal, due to these states, is a group of three multiplets separated by 1 eV. As the element these signals originate from is the same, the FWHMs of the peaks can all be constrained to be the same in the fitting procedure. Another multiplet of four peaks is reported to come from a contribution of surface Fe^{3+} ions, separated from each other by 1 eV, with the first centred around 708.75 eV. The FWHM of the Fe^{3+} peaks were also constrained to be the same as the Fe^{2+} bulk signal. Following the iteration of fitting procedures, using casaXPS, the model was a better fit for removing the first Fe^{2+} surface multiplet, centred at 707.1 eV. The improvement to the model was negligible, however the signal from the state was observed to be small, and as it was buried under a large Fe^{2+} bulk signal, it was not possible to confirm or deny its presence. The relative amplitudes of the surface peaks were constrained to each other, based on values from previous reports [139]. The ratio of the amplitudes of the surface state peaks to the Fe^{2+} bulk peak, shown in Figure 4-5, increased compared to the reported values. The sample measured in the literature was the surface of a fractured single crystal. As the sample measured here is comprised of nanoparticles with a larger surface to volume ratio, the intensity of the signal from the surface increases, while the signal from the bulk decreases. This is because there will be a higher number of surface states relative to the bulk state in the sample reported here, compared to that in the literature. Therefore, the increase in the relative amplitude of the higher binding energy states in this sample is another confirmation that they are likely to be surface states. This shows that as synthesised FeS_2 nanoparticles intrinsically have Fe defect states, without any further modification.

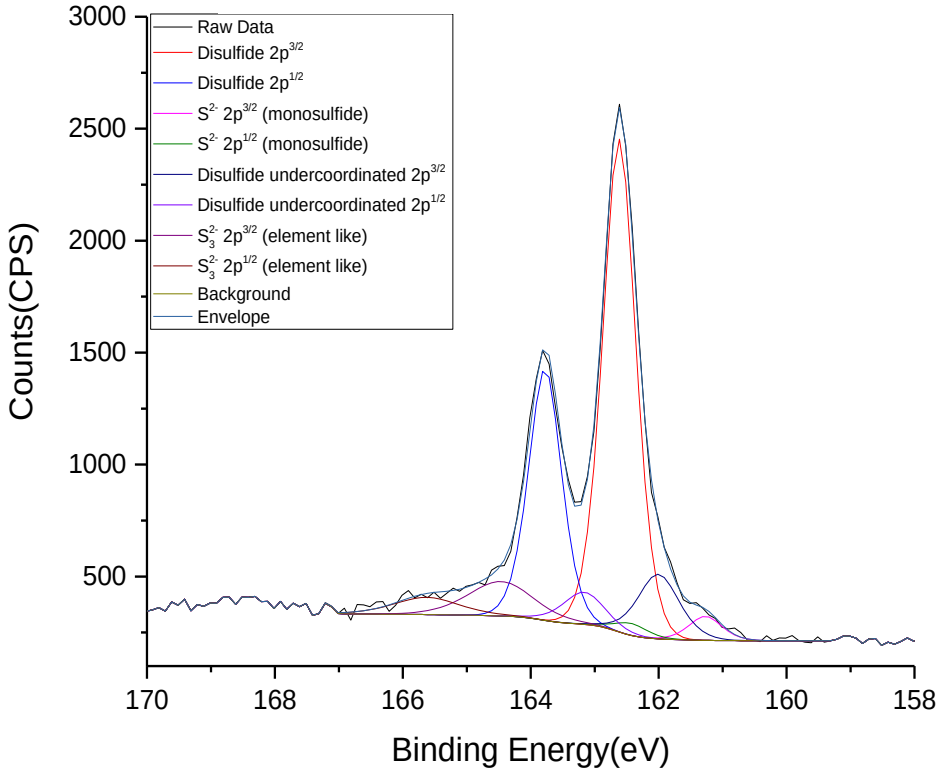

Figure 4-6- S 2p region of an XPS spectrum taken of pristine FeS_2 nanoparticles taken directly from a synthesis.

Figure 4-6 shows a Sulphur 2p spectrum taken by XPS of pristine FeS_2(P) nanoparticles harvested directly from a synthesis. The peaks at 162.6eV and 163.8eV correspond to fully co-ordinated bulk Sulphur in Pyrite form, denoted in Figure 4-6 as disulphide 2p. As for the Fe signal, the low FWHM of the signal is representative of the highly crystalline nature of the sample. The other doublet signals present in Figure 4-6 represent the Sulphur surface states of FeS_2. The Sulphur surface states on FeS_2s surface should take one of three forms. The first is shown in Figure 4-6 as S^{2-} 2p (monosulphide). This state is a result of fractured Sulphur-Sulphur dumbbells on the surface of FeS_2, where the resulting Sulphur is still bound to an

Iron atom. The S $2p_{3/2}$ signal from this state is centred at 161.1eV. The second surface state is denoted as disulphide under co-ordinated in Figure 4-6, and results from a Sulphur atom still bound to another Sulphur and an Iron, but not surrounded by a full number of ligands. The S $2p_{3/2}$ signal for this state is at 162eV (Figure 4-6). The third surface Sulphur state is denoted in Figure 4-6 as S_3^{2-} 2p (element like), the origin of which is uncertain. It may potentially have arisen due to a Sulphur-Sulphur bond being ruptured, followed by the transfer of an electron to another already formed Sulphur monomer. The resulting S^0 may have been able to react with underlying disulphide to produce S_3^{2-} with very little activation energy. Binding energies of polysulphides have a large range, approximately 2eV, hence this peak is fitted both with multiple doublet peaks or a broad single peak[145]. In this case, the model used a doublet, with a peak separation of that of elemental Sulphur. The FWHM of the monosulphide and under co-ordinated disulphide peaks were constrained to be the same as that of the bulk Sulphur signal. However, the FWHM of the element-like Sulphur surface states were not constrained as they were a representation of Sulphur in multiple states. As with the Fe XPS spectrum, the ratio of the amplitude of the surface states to that of the bulk can be taken as an approximation of the defect state density.

4.3.2 FeS_2 (N_2 and H_2 annealed)

Figures 4-7 and 4-8 show the XPS of the Fe 2p and S 2p peaks of FeS_2 thin films annealed in a Nitrogen atmosphere, after ALD of 3nm of TiO_2. Initially, the model that was developed using as synthesised FeS_2 nanoparticles was used to analyse the Fe $2p_{3/2}$ spectrum shown in Figure 4-7. The sharp peak at a binding energy of 707 eV corresponded with that of Fe in bulk FeS_2(P) crystal structure. However, the broad feature at a higher binding energy does not fit features expected for an elevated defect state density. The model was altered to include several Iron Oxide components, which showed a slight improvement. The best fit however was a single broad peak which envelops the binding energies for all forms of Iron Oxide[146]. This would physically make sense, as the majority of the oxidation will have come from the

ALD process. No form of Iron Oxide will have been preferentially selected for during this oxidation process, therefore all would be present, and are [137]. In addition to this, the crystallinity of the Iron Oxide would be negligible, if not amorphous. Consequently, the XPS signal from Iron in this form would be very broad.

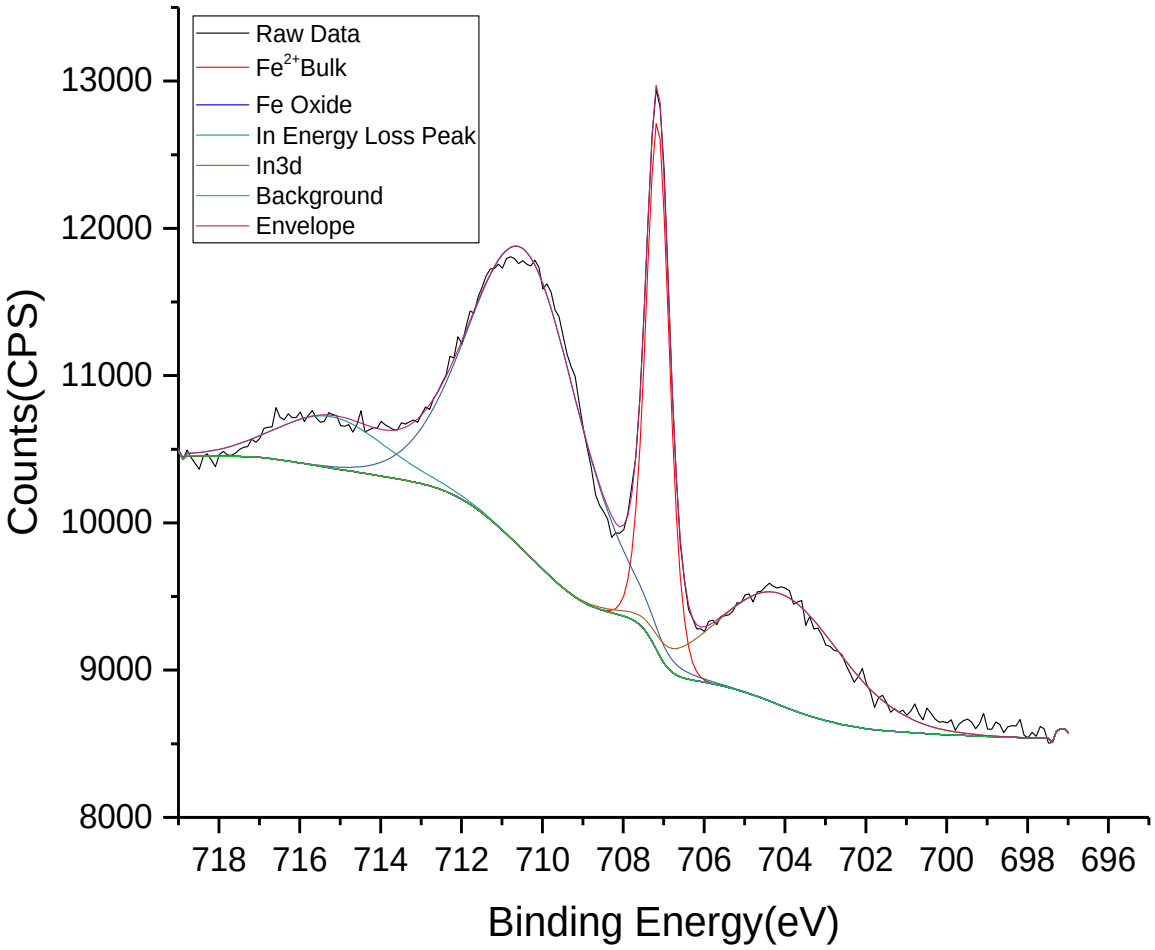

Figure 4-7 Fe $2p_{3/2}$ region of an XPS spectrum taken of a Nitrogen annealed FeS_2 thin film after ALD.

There are two additional peaks present in the XPS spectrum in Figure 4-7 which are not present in the pristine sample (Figure 4-5). The first is at a lower binding energy to the Fe

$2p_{3/2}$ bulk signal, and corresponds to a signal from the 3d core structure of Indium [147][148]. This signal originated from the ITO TCO substrate the FeS_2 nanoparticles were deposited on. Related to this, the broad peak at a higher binding energy is an energy loss peak from the Indium. The reason Indium is not present in the first measurement (Figure 4-5) is that the pristine FeS_2 nanoparticles were measured using Carbon tape as a substrate. Due to signals from oxidation that occur through the ALD process, in addition to the signals from the Indium in the substrate, the Fe XPS spectrum is not useful for defect state density estimation.

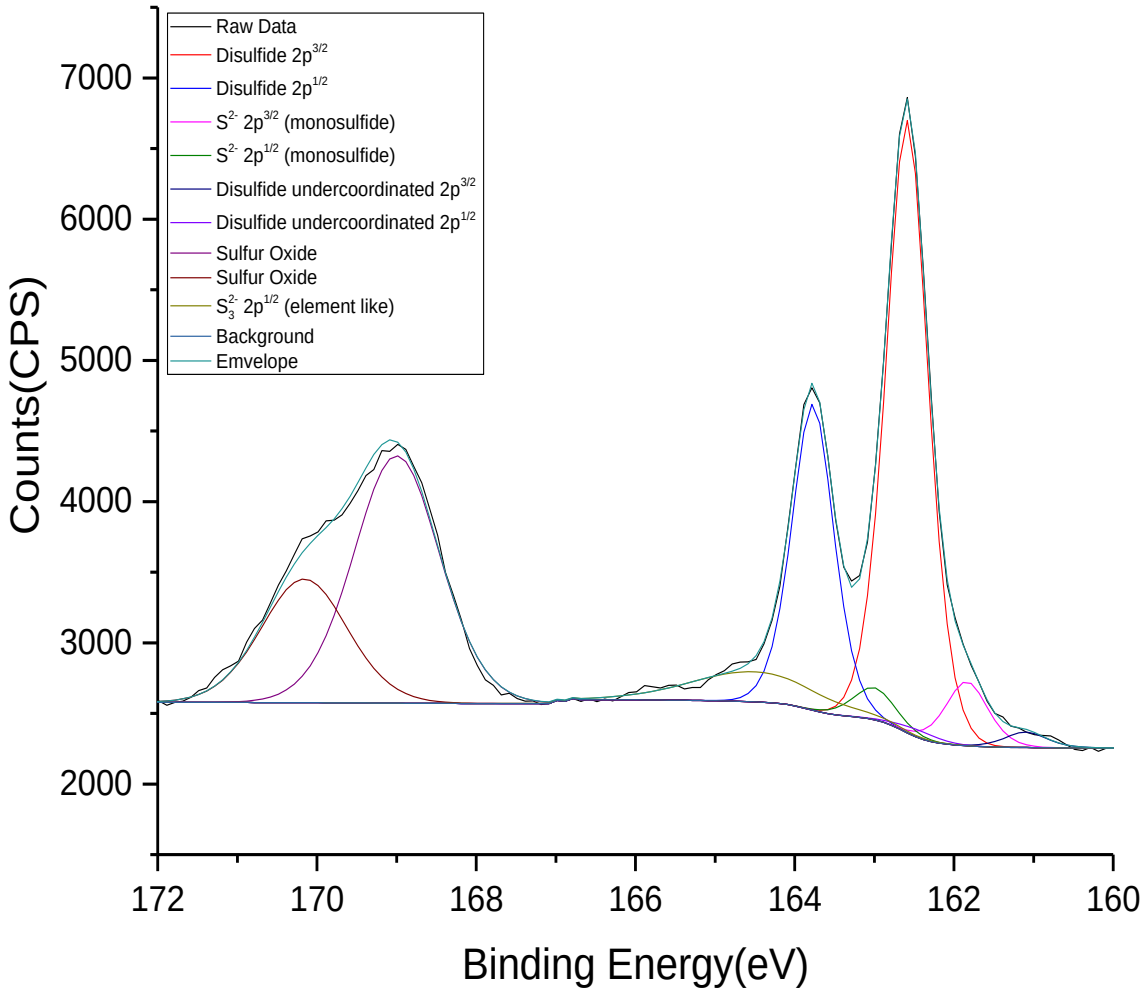

Figure 4-8 S 2p region of an XPS spectrum taken of a Nitrogen annealed FeS_2 thin film after ALD.

Figure 4-8 shows the S 2p spectrum of a FeS_2 thin film annealed in a Nitrogen atmosphere. The process to adopt the model developed on a pristine sample of FeS_2 is the same here as

for previous XPS analysis, with two exceptions. Firstly, the signal corresponding to elemental Sulphur needed to be changed to a broad representation. Potentially, this could indicate that the annealing, and subsequent ALD process, altered the crystallinity and surface structure of elemental Sulphur. In addition to this, a large Sulphur Oxide feature is now present at a higher binding energy of 175eV[149]. This is likely caused by the ALD process, as in the case for the Fe spectrum. However, the signals from the defect states of monosulphide and under co-ordinated disulphide are still present in the same form as the pristine FeS_2. This is also the case for thin film electrodes annealed in Hydrogen atmospheres, as shown in Figure 4-9A and B.

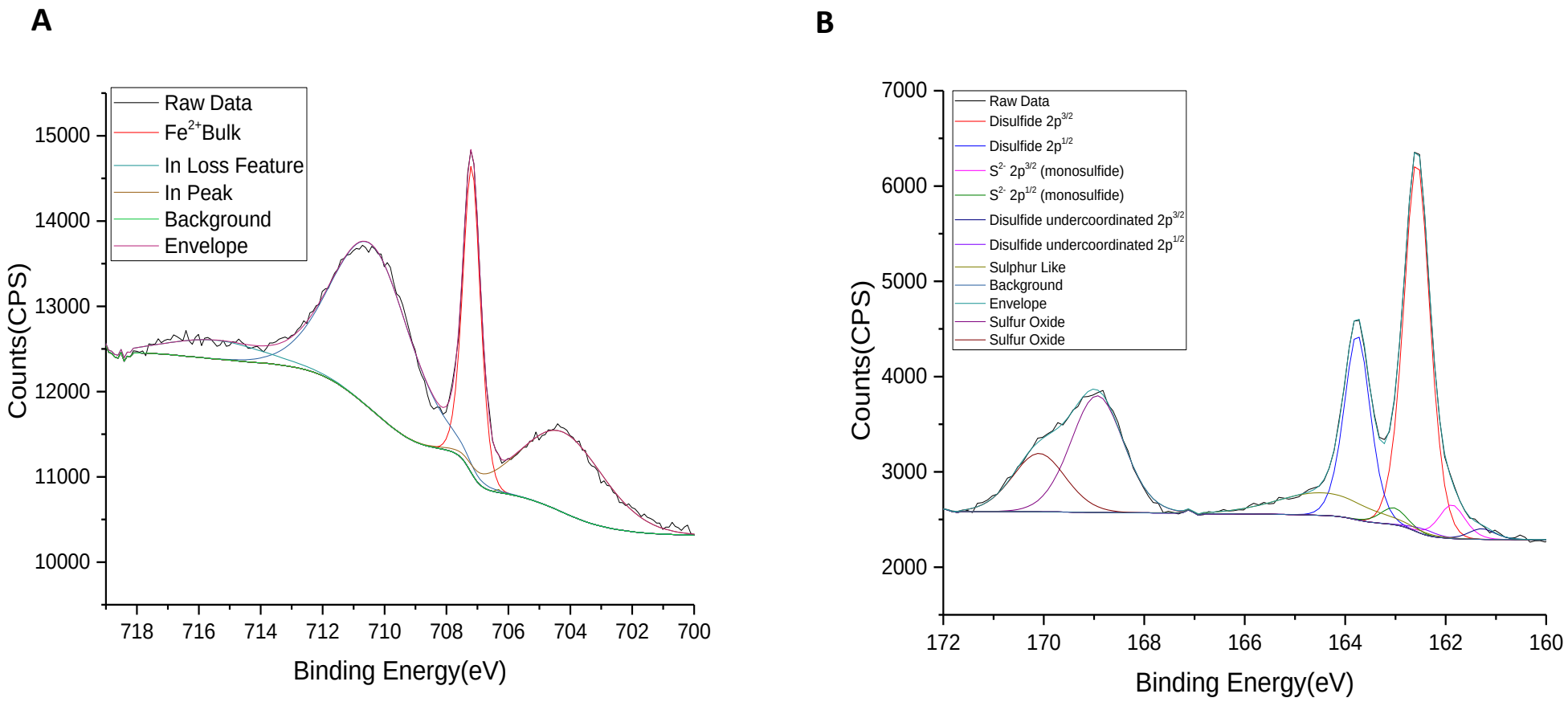

Figure 4-9 (A) Fe $2p_{3/2}$ region and (B) S 2p region of an XPS spectrum taken of a Hydrogen annealed FeS_2 thin film after ALD.

To determine if there was an increase in the defect state density relative to that of the bulk, the ratio of the area of the 2p peaks for the bulk and defect states were calculated. Figure 4-10 shows how the ratios of under-coordinated disulphide (Figure 4-10A) and monosulphide (Figure 4-10B) defects vary with respect to bulk like Sulphur states.

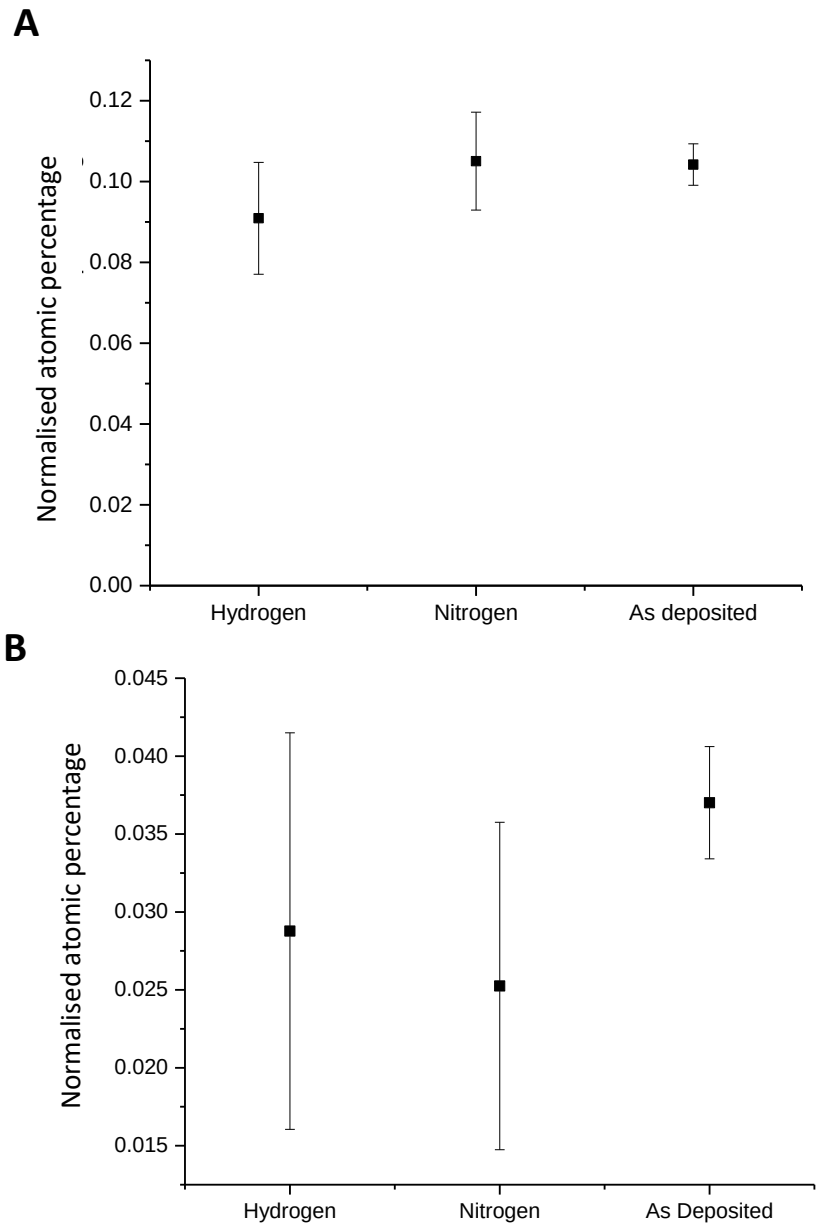

Figure 4-10 Graphical representation of the ratio of, (A) disulphide under co-ordinated and (B) monosulphide, Sulphur states to bulk like Sulphur states for Hydrogen, Nitrogen and As-Deposited electrodes.

No definitive conclusions can be drawn as the errors on measurements like this are often large. However, a trend is present for both annealing atmospheres as the density of monosulphide defect states is reduced after annealing. This is as expected, as the elevated temperature would remove the singly-bound Sulfur atoms more easily. For the under co-ordinated Sulphur defects, the density is unchanged for the Nitrogen annealing process. However, for the Hydrogen annealing, there are less under co-ordinated disulphide Sulphurs. This would suggest Hydrogen was stripping Sulphur from the FeS_2 nanoparticles outermost surface layers. The intention of the Hydrogen annealing was to substitute a Hydrogen atom into the Sulphur defect of a FeS_2 defect site. If this had happened with no unwanted side reactions, there would be no observable difference to the Nitrogen annealed sample. However, instead of benignly sitting in a Sulphur defect state, it appears the Hydrogen has removed Sulphur from the surface. This is futher confirmed by a decreased performance of the Hydrogen annealed electrode towards photoelectrochemical Hydrogen production, as seen in Chapter 5.

4.4 XPS of Sulphur annealed electrodes

As mention in previous sections (Section 4.2.2), the process developed to anneal FeS_2 thin films in a Sulphur atmosphere removed the conductive properties of ITO substrates. As a result, it was only possible to investigate the potential improvements to the FeS_2 thin films using XPS. As argued in the above sections, any process that removes the high concentration of Sulphur defects should result in improved photoelectrochemical Hydrogen production, and photocurrent density.

4.4.1 FeS_2 (Sulphur annealed)

The model developed to analyse the as synthesised nanoparticles was applied to XPS data taken on Sulphur annealed electrodes (Figure 4-11). However, an adaptation was made to include the Sulphur Oxide peaks, and the element-like Sulphur defect was changed to one

broad peak. The addition of peaks that correspond to an element-like Sulphur, not bound to Fe, was also necessary. This contribution likely comes from excess Sulphur deposited during the Sulphur annealing process. More importantly, however, is the complete removal of any signal corresponding to the monosulphide and under co-ordinated disulphide defect states. As such, further development of this Sulphur annealing process would likely yield positive improvements to FeS_2(P) photoelectrochemical performance. Unfortunately, due to time constraints, this could not be researched for this thesis.

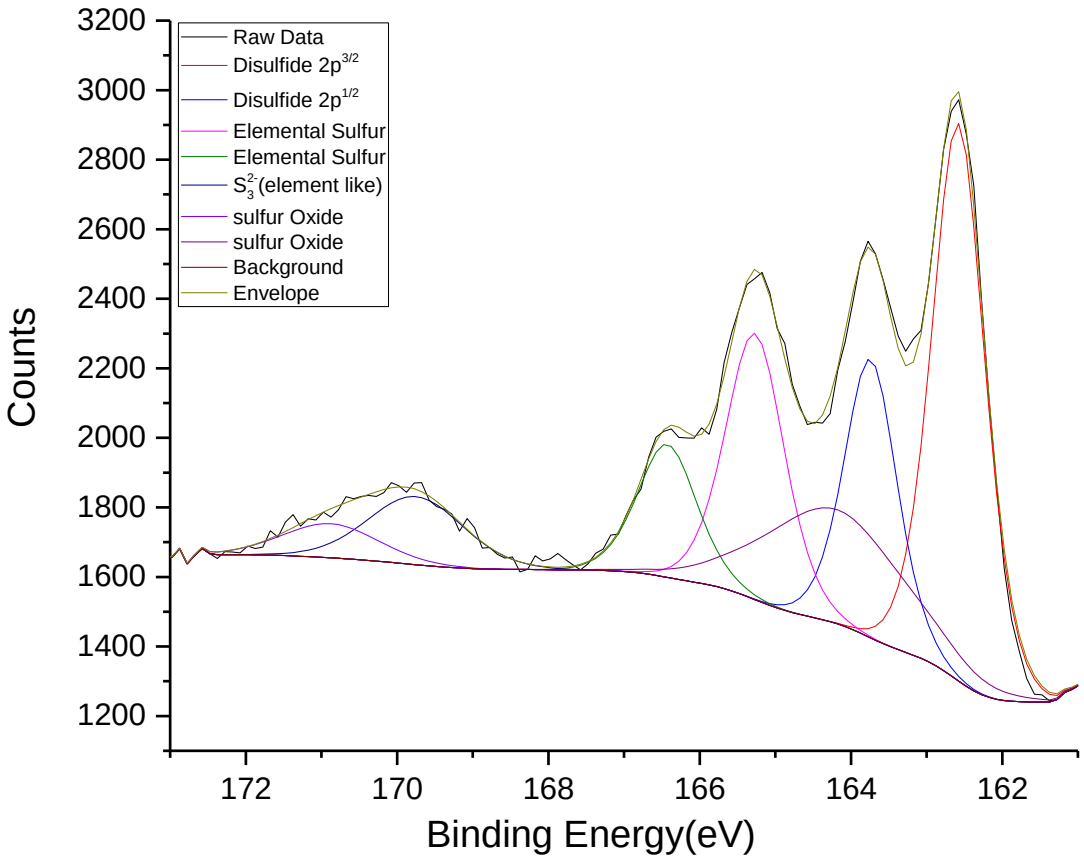

Figure 4-11-S 2p spectrum of an FeS_2 electrode annealed in a Sulphur atmosphere followed by ALD.

4.5 Atomic layer deposition (ALD) of protective overlayers

In the previous section, the problem of the physical instability of FeS_2 electrodes on ITO was discussed. In Figure 4-3, the current density from the optimum annealed electrode (red) decayed over time. Despite observing a current density over the full three hours, there was still a noticeable, gradual drop in current density over the first hour of the experiment. This decay in current density was due to unwanted side reactions, resulting in the deterioration of the electrodes surface. This proceeded either via the conduction band minimum or valence band maximum, or via mid-gap surface states. This was dependant on the presence of Oxygen and water at the interface. This chemical instability of the electrode is another critical barrier to overcome for FeS_2 to be utilised industrially.

ALD of protective over-layers, to chemically stabilise a material, is a widely researched option for protecting unstable semiconductor absorber materials for photoelectrochemical applications [150][151][152]. ALD deposits materials layer by layer and is, therefore, able to deposit layers of materials with nanometer precision. The ideal over-layer would be suitably thick, as to avoid pinholes in the layer. The bandgaps of the semiconductor absorber and the protection layer should also be aligned as to improve charge transfer to the surface [153]. Using the above criterion, two over-layer materials were selected; Al_2O_3 with a large bandgap and high stability in neutral pH solutions[154], and TiO_2 which, although less stable than Al_2O_3, has a smaller bandgap thus a more preferential band alignment.

4.5.1 Al_2O_3 over-layers on FeS_2 thin film electrodes

Whilst ALD of protective over-layers is well studied, the application of the technique to stabilise FeS_2(P) is not. As such, the optimum thickness for the deposition of Al_2O_3 was unknown. Due to the large bandgap, the material would have to be as thin as possible to maximise electron transfer into the electrolyte. FeS_2 thin film electrodes produced from nanoparticles, via the methods discussed in Chapter 2.6, are also porous. Therefore, four

methods of ALD deposition of Al_2O_3 are subsequently investigated photoelectrochemically. The methods were designed to assess which deposition method was more suitable to deposit a continuous layer of Al_2O_3 on the porous electrode. To this end, two different thicknesses of Al_2O_3 with two different hold times are investigated. Here, the hold time refers to the time the Al_2O_3 precursors are left in contact with FeS_2 thin films at each deposition cycle.

The deposition of Al_2O_3 is similar to the deposition of TiO_2, as discussed in Chapter 2.8. The precursor for the Al was electronic grade Trimethylamonium (TMA) (SAFC Hitech). For deposition cycles without a hold step, the process was a 25 ms dose of TMA, followed by a 10 second purge, then a 20 ms water treatment, followed by a 10 second purge. The process was then repeated the desired number of times to achieve the desired thickness. During the process, the chamber was under ultra-high vacuum and purged with a flow of Argon at 100 sccm (standard cubic centimetres per minute). For deposition cycles with a hold step, there was a 25 ms dose of TMA as before, however, it was instead followed by a two second exposure. The chamber was then purged by pumping for 10 seconds. The sample was then dosed with water for 30 ms and exposed for a further two seconds, followed by another 10 second purge via pumping. Again, this cycle is repeated to achieve the desired thickness. The differences between electrodes with and without hold steps therefore, are the time the Al precursor spends in contact with FeS_2 in the chamber. The reasoning for the extended hold step is to give extra time for the Al precursor to penetrate the porous FeS_2 film. Figure 4-12 shows the photocurrent density of FeS_2 electrodes under constant illumination, with an Al_2O_3 passivation layer deposited under different conditions.

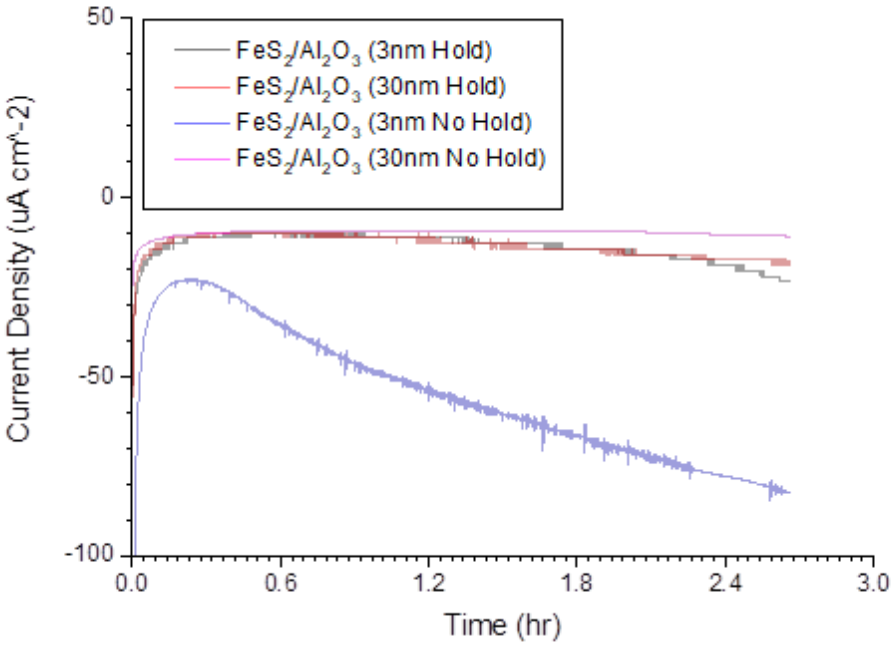

Figure 4-12 Photoelectrochemistry of FeS_2 thin films with different thicknesses of Al_2O_3 over-layers with and without an extended hold step in the deposition process.

FeS_2/Al_2O_3 (30nm hold) and (30nm no hold) both perform on a similar level, however the electrode with the hold step has a slightly higher current density. This increase in current density is likely to be due to a higher amount of surface to electrolyte contact area, as the Al_2O_3 over-layer penetrate deeper into the pores during the hold step. FeS_2/Al_2O_3 (3nm hold) performs on the same level as FeS_2/Al_2O_3 (30nm hold), however in the last 30 minutes the current density of the FeS_2/Al_2O_3 (3nm hold) starts to increase. Their initial performance simiarlity is likely due to the fact they both have a hold step, and hence the same surface to electrolyte contact area. However, the thinner over-layer (3nm hold) either has pin holes or is destroyed quicker than the thicker one, resulting in an increase in current density in the last 30 minutes. The increase in current density is likely coming from electrons taking part in FeS_2 decomposition reactions. The similarity in current density indicates that the potential barrier to electron transfer into the electrolyte is already too high, even at 3nm. Finally,

FeS_2/Al_2O_3 (3nm no hold) had the highest current density which is likely due to the surface not being adequately protected by the ALD layer of Al_2O_3.

Figures 4-13A and B show high-resolution Scanning-TEM Bright Field and High Angle Annular Dark Field (HAADF) images of cross-sections of a film deposited with 3nm of Al_2O_3 with a hold step. From these images, the porous nature of the film can be seen, with cavities being formed by the loose packing of the nanoparticles. Figures 4-13C-G show EDS maps of a section of the FeS_2 thin films highlighted by the red square in Figures 4-13A and B. Figure 4-13C shows the EDS map of all elements present in the film. The signal due to Copper (Cu) is from the grid that supports the Carbon film. Gallium (Ga) is incorporated into the sample during the ion milling process carried out to manufacture the cross-section of the film. Chromium, Platinum and Gold are present in the protective over-layers which support the fragile cross-section of the thin film. The signal from the Indium edge is from the Indium in the ITO substrate, scattered across the sample in the ion milling process. Figure 4-13F shows the atomic percentage thin film map of Aluminium (Al) within the boxed red section in Figure 4-13A and B.

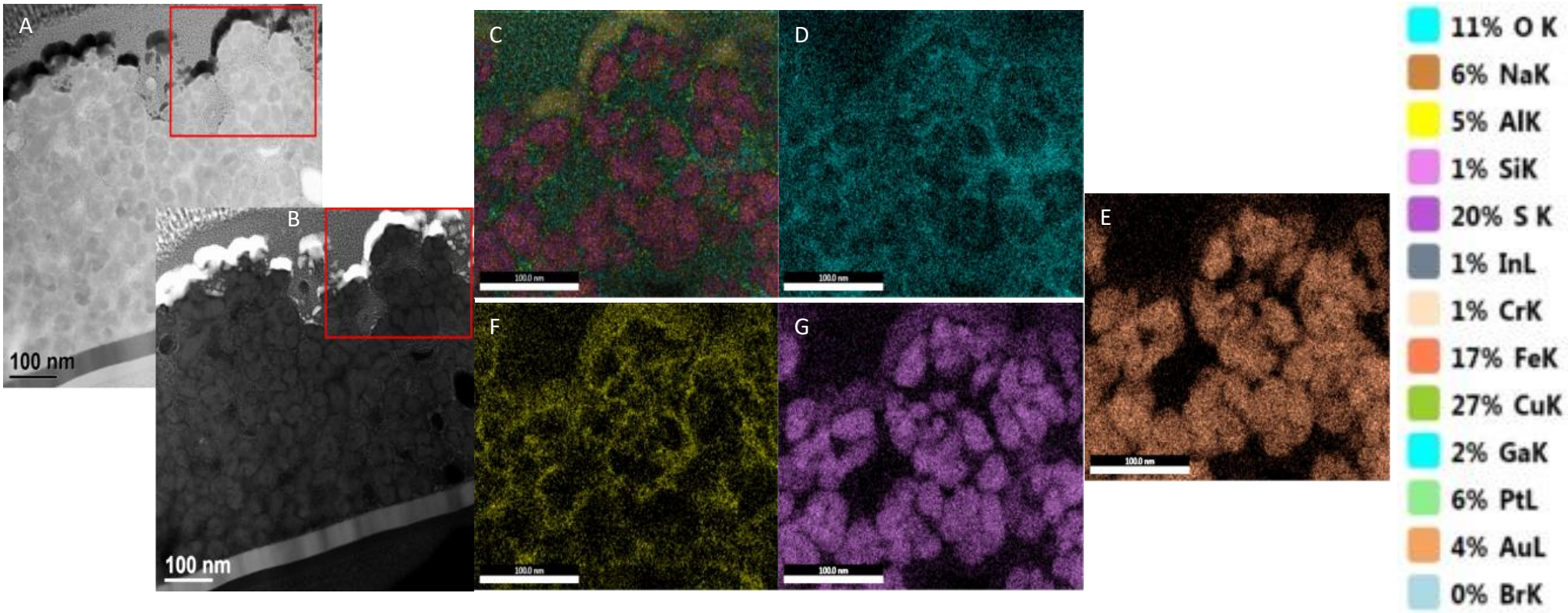

Figure 4-13(A) High-resolution Scanning-TEM Bright Field image of a cross-section of a FeS_2 thin film after ALD of 3nm of Al_2O_3 (B) High-resolution Scanning-TEM HAADF image of a cross-section of a FeS_2 thin film after ALD of 3nm of Al_2O_3(C) EDS map of section of FeS_2 film highlighted by the red box in (A) and (B), displaying all elements observed (D) Elemental map of the distribution of Oxygen (E) Elemental map of the distribution of Iron (F) Elemental map of the distribution of Aluminium (G) Elemental map of the distribution of Sulphur. Colour coded key for elemental representation is featured on the right-hand side of the figure.

The distribution of the Aluminium within the image suggests that the ALD process coats the individual nanoparticles with a layer of Al_2O_3. However, it is not possible to distinguish if the film is continuous or whether there are pinholes present, meaning the surface might not be completely passivated. Figures 4-13E and G show the atomic percentage thin film elemental map of Iron and Sulphur respectively. The images confirm that the particles seen in the high-resolution images are indeed composed of Fe and Sulphur. The above photoelectrochemistry and cross-sectional Scanning-TEM has proven that even ultra-thin layers of Al_2O_3, under the right deposition conditions, are enough to passivate FeS_2s surface. However, the current density under Hydrogen evolution conditions is very low (Figure 4-12).

4.5.2 TiO_2 ALD over-layers on FeS_2 electrodes

Due to the low current density achieved by Al_2O_3, another stable material was needed to passivate the FeS_2 electrode surface. The material chosen was TiO_2, due to its preferential band alignment. As with Al_2O_3, it is necessary to ascertain the optimum thickness of TiO_2 to passivate the electrodes surface, but also allow for electron transfer through the solid/electrolyte interface. Figure 4-14 compares FeS_2 thin film electrodes at -0.19 bias vs. RHE with a surface passivation layer of 30nm TiO_2 and 3nm TiO_2. To ensure any photocurrent measured was not due to TiO_2, a long-pass filter was used, with a cut off wavelength at <450nm. Both deposition methods were conducted using a hold step as discussed in the previous section (Section 4.5.1). As it was determined that the hold step increased the passivation of the surface of the electrodes, no experiments were conducted on TiO_2 deposited electrodes without a hold step. Figure 4-14 shows that FeS_2 thin films with a 30nm TiO_2 over-layer had no current density across the full three-hour measurement. Again, this shows that whilst the electrodes are now chemically stable, they show no proclivity towards Hydrogen evolution. FeS_2 electrodes coated with 3nm of TiO_2 showed a current density over the duration of the experiment, which was two orders of magnitude higher than the comparable Al_2O_3 electrode shown in Figure 4-12. There is a broad feature present for the

3nm TiO_2 coating which is not present for the 30nm coating (Figure 4-14). This is likely caused by incomplete surface coverage of the 3nm TiO_2 over-layer. If there is not full surface coverage, there would be exposed FeS_2 surface that would be able to react with water. These side reactions would cause an increase in the current density observed. As the reaction of the exposed surface continues, there would be a build-up of decomposition products resulting in a passivation layer and a decrease in observed current density.

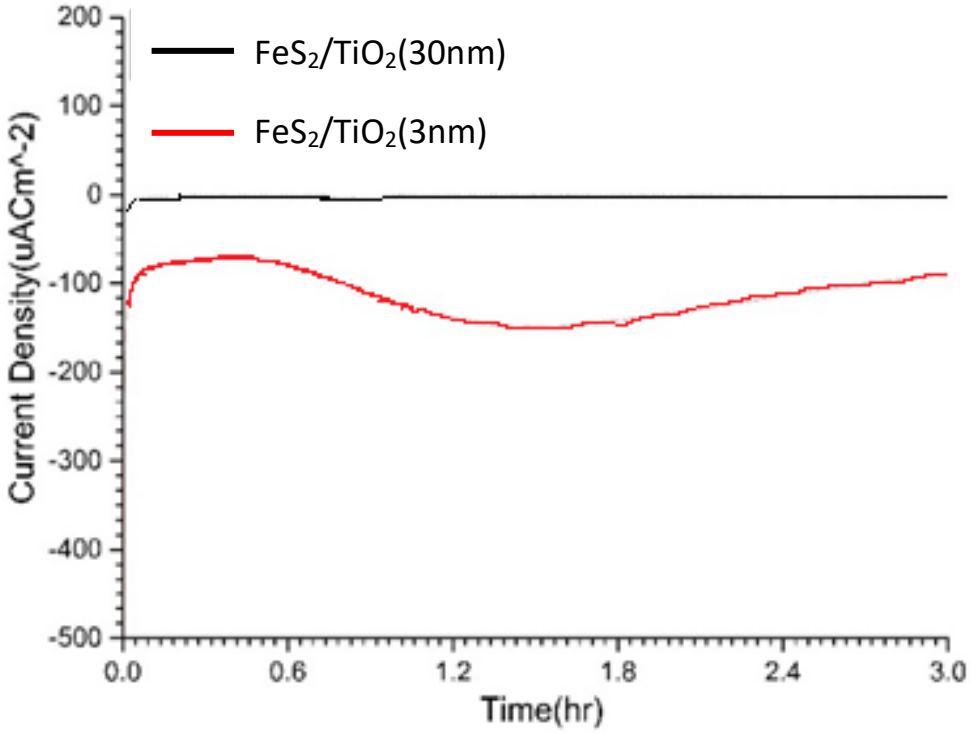

Figure 4-14-Chronoamperometry of FeS_2 electrodes with an over-layer of 30nm of TiO_2 (black) and 3nm of TiO_2 (red)

4.6 Electrochemical deposition of a Pt co-catalyst

The main reason for FeS_2 thin film electrodes becoming non-functioning is likely to be a reaction between exposed surface FeS_2 with water in the electrolyte. Another reaction occurring at the surface is the Hydrogen evolution reaction (HER). If the rate of HER can be increased, then the percentage of electrons going to decomposition reactions will relatively decrease. To determine the effect of Platinum (Pt) deposition on the stability and electrochemistry of FeS_2 thin films, linear sweep voltammetry was performed under illumination. For the measurement, the electrolyte and reference electrode were a pH 7 0.1M phosphate buffer solution and Ag/AgCl (saturated). The photoelectrochemical cell was degassed, and the sample left under illumination for five minutes before starting the experiment. The scan speed was 10 mV $second^{-1}$, and the potential was varied from 0 to -1V vs. Ag/AgCl (saturated) (0.69V to -0.39V vs RHE). Pt was deposited electrochemically following the procedure outlined in Chapter 2.10. Figure 4-15 compares the linear sweep voltammetry for FeS_2 electrodes with and without Pt deposited.

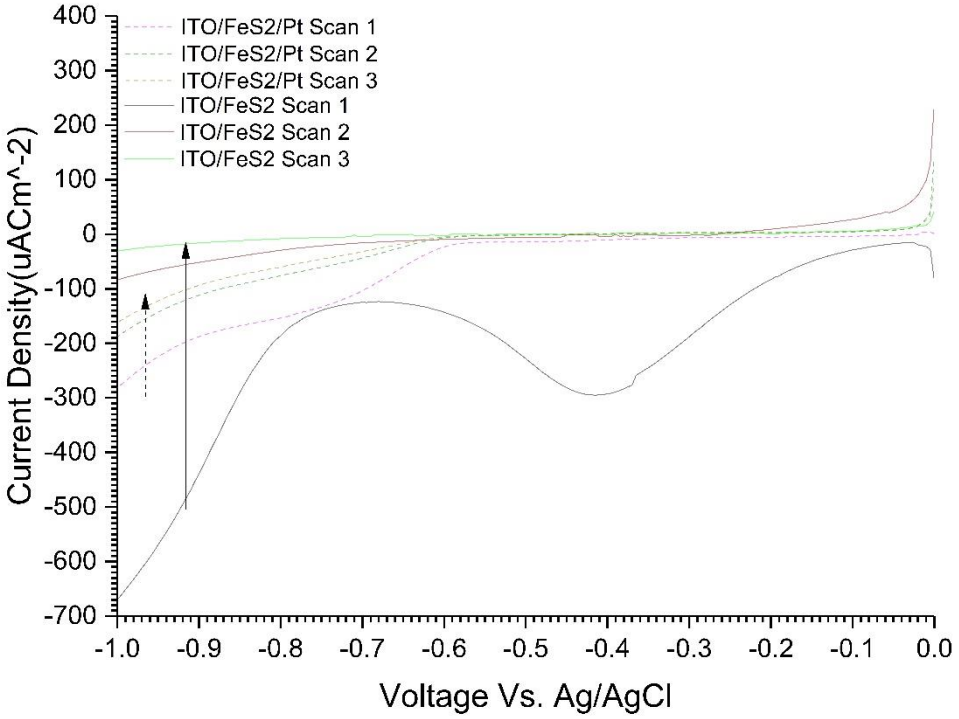

Figure 4-15- Comparison of linear sweep voltammetry of FeS_2 electrodes with (dotted) and without (solid) Pt under illumination.

Dotted lines represent FeS_2 deposited with Pt, and solid lines represent bare FeS_2. Multiple scans were taken to identify any improvements to stability. The first scan for the bare FeS_2 electrodes shows a very broad feature at -0.42 V, a feature not present in the first scan of FeS_2 deposited with Pt. The origin of this feature is uncertain, but is likely a result of a reaction with the surface of FeS_2. A potential candidate for this surface reaction would be the FeS_2 surface states reacting with water, via pinholes in the TiO_2 layer. The peak is not present after Pt depostion as this could block these pinholes. The onset current for what is likely to be Hydrogen evolution is also shifted from -0.8 to -0.59 V with the deposition of Pt, due to Pt lowering the overpotential required to drive the reaction. There are two important observations to be drawn from this voltage range in Figure 4-15. Firstly, the peak current density achieved by the FeS_2 and FeS_2/Pt electrodes, is higher for the electrode without Pt. Secondly, following successive scans, by the third scan, the FeS_2/Pt electrode has retained

much more of its peak current density than the bare FeS_2. The conclusion from the latter point is that the FeS_2/Pt electrode is much more stable. This also explains the first point; the bare FeS_2 electrode has a higher current density in this region, as a significant portion of the electron transfer across the surface is going towards a decomposition reaction. This reaction is likely to be water reacting with FeS_2 to dissolve Sulphur as SO_4, leaving behind elemental Fe (see Figure 1-6 in Chapter 1 for Pourbaix diagram). Overall, with the excpetion of the unknown origin of the broad peak at -0.42V, Figure 4-15 shows that Pt deposition improves the stability of a FeS_2 electrode and shifts the onset potential towards Hydrogen evolution.

To further understand the origin of the improved photocurrent density and stability, cross-sectional STEM was performed in conjunction with EDS mapping. Figure 4-16A and B show high-resolution bright and HAADF TEM images, respectively, of a cross-section of a Pt deposited thin film. Figure 4-16C shows an EDS map corresponding to the same region of the cross-section displayed in Figure 4-16A and B. The green pixels in the image correspond to signals interpreted to be from Pt. In Figure 4-16B, the bright material corresponds to one with a higher density, most likely Pt, which is also shown by the dark spots in Figure 4-16A. The change from light to dark for Pt is due to the change in imaging modes. This conclusion is confirmed by the false colour Pt elemental map in Figure 4-16C. There is, however, also signal that corresponds to Pt above where the Pt should be, which has occurred due the method used to prepare the cross-section samples. When the cross-sectional samples were produced, Pt was deposited via an electron beam as small nanoparticles. This is evident as these appear as small dots, rather than the large clusters that can be seen due to the electrochemically deposited Pt (Figure 4-16C). Another conclusion to draw from Figure 4-16 is that the Pt would offer additional surface coverage, separating the FeS_2 nanocrystals further from the working electrolyte, in a photoelectrochemical cell. Therefore, the increase in stability mentioned above would result from increased surface passivation, as well as the Pt offering a competitive reaction pathway for electrons.

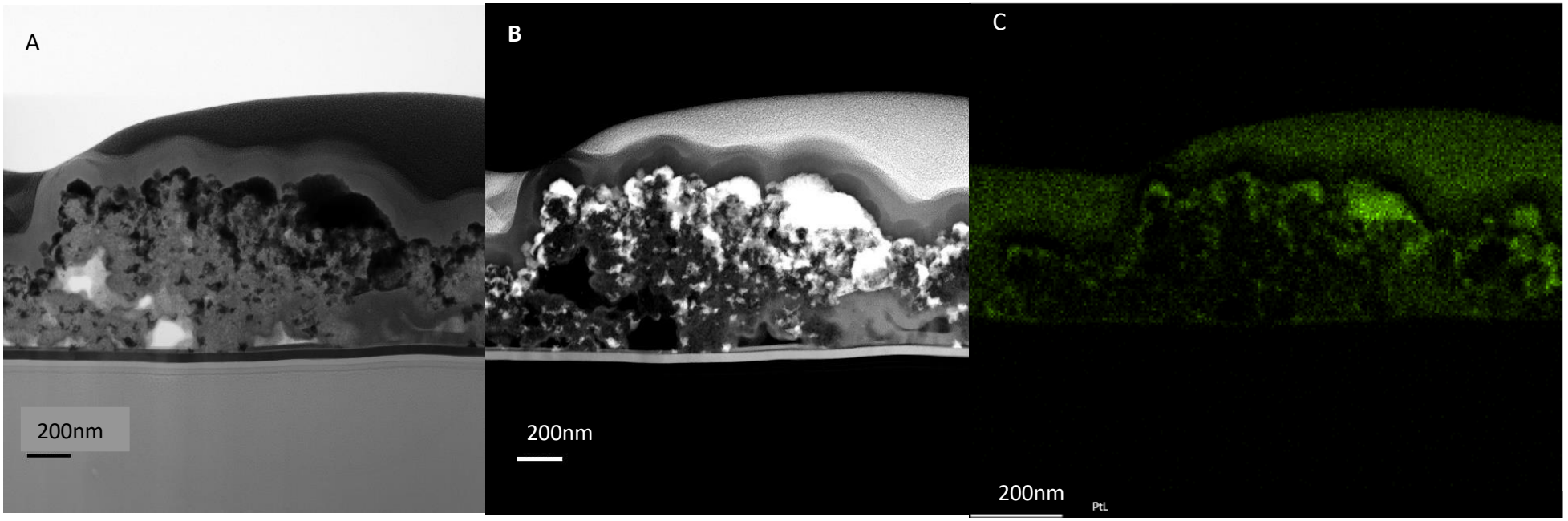

Figure 4-16 (A) High-resolution Scanning-TEM bright field image of a section of FeS_2/TiO_2 (3nm)/Pt thin film. (B) High-resolution Scanning-TEM HAADF image of a section of FeS_2/TiO_2 (3nm)/Pt thin film. (C) Pt thin film elemental map of high-resolution images.

4.7 Conclusions and further work

In this chapter the chemical and physical stability of FeS_2 was investigated under different annealing conditions, protective over-layers and a Pt co-catalyst. The main aims of the chapter were to investigate what preparation, and subsequent modification, techniques could improve the stability of FeS_2 thin film electrodes. The physical stability of the thin film, with regards to the adhesion to an ITO substrate, was improved via an annealing step. The annealing step was then further optimised to prevent the oxidation of the FeS_2 nanoparticles during annealing. These steps have taken the operational lifetime of the as prepared FeS_2 thin films from 15 minutes to at least three hours.

The ALD of protective over-layers on FeS_2 surfaces was then investigated, with the most effective passivation method being a 3nm ALD over-layer of TiO_2. The chemical stability of the FeS_2 electrodes have been improved by the optimisation of the ALD of a passivating over-layer. Two materials for passivating the surface were tested, Al_2O_3 and TiO_2. TiO_2 proved be the preferential protective over-layer material as, although less stable than Al_2O_3, Al_2O_3 showed very little observable activity. Further deposition of a Pt co-catalyst proved to offer more stability, by improving the rate of the HER, thereby competing with decomposition reactions for electron transfer. Stability was further increased by an increase in surface passivation.

The effect of annealing electrodes in Nitrogen and Hydrogen atmospheres on the surface chemistry of FeS_2 has also been investigated. Hydrogen and Nitrogen annealed thin films show a trend to a decreasing number of monosulphide Sulphur vacancies. However, these results need to be improved with repeat measurements, due to significant errors from poor statistics. In addition to this, XPS of electrodes annealed in Hydrogen, for increasing lengths of time, would also confirm if the process is creating Sulphur defects. XPS results also showed the absence of any signal due to secondary phases of Fe and S. A study of the surface of the

material at a synchrotron source would also increase understanding, as the energy of the exciting photons could be varied to make the measurement more surface sensitive.

The work presented in this chapter has resulted in some further questions. Firstly, when conducting cross-sectional Scanning-TEM, it was only possible to measure the chemical presence of Ti and Al to determine surface coverage. The inability to observe the actual film thickness was due to the lack of access to suitable preparation equipment. While it was not possible to directly observe the presence of the over-layer, it may be possible with a higher resolution Scanning-TEM. The only materials accessible during this investigation of over-layers were Al_2O_3 and TiO_2, however investigations of a suitable over-layer could be taken further. If an oxide with a narrower bandgap, and a conduction band minimum below that of FeS_2 is deposited, a thicker over-layer could be used. This would allow, not only a better charge separation, and therefore a larger photocurrent, but also would result in a more stable electrode. Finally, the nature of the improvement to the stability of the thin film after Pt deposition, is only theorised to be an improvement due to a more competitive reaction pathway. Transient Absorption Spectroscopy (TAS) investigations of FeS_2 thin films with and without Pt, under steady-state illumination, would indicate whether this is true.

Another potential method for increasing the stability of FeS_2 nanoparticles to drive a water-splitting reaction, is to remove the material from the electrolyte completely. One of the main problems for FeS_2 as an absorber in a photoelectrochemical cell, is its instability in an aqueous environment. In an operational cell, the most suitable place for FeS_2 may reside outside the cell completely. This could be either as part of a solar cell or as part of a regenerative photoelectrochemical cell utilising a non-aqueous electrolyte, both of which would apply bias to the photoelectrochemical cell, driving the water-splitting reactions. In this situation, there would still be problems to be overcome [155], but chemical instability would no longer be an issue.

5 *Photoelectrochemistry of FeS_2 after Annealing in H_2 and N_2*

A limiting factor for photocurrent density for Iron Pyrite is its defect state chemistry, predominantly the intrinsically high density of Sulphur defect states (V_s) [156]. These defect states trap electrons facilitating recombination of electron-hole pairs. The reason the defect states in FeS_2 cause a problem is not only their high density, but also that energetically they are located within the bandgap [157][78][77]. To improve FeS_2s photocurrent density under working conditions, and potentially its stability, its defect states should be removed. Substituting a V_s for Oxygen or Hydrogen will remove the Sulphur vacancy component from FeS_2s bandgap, without creating more inter-gap states [158][159]. This chapter focuses on the difference in electrochemistry of Hydrogen and Nitrogen annealed electrodes. Sulphur electrodes annealed via the method described in Chapter 2.11.2 could not be included. Unfortunately, at this stage, it was identified that the FeS_2 thin films annealed in Sulphur were non-conductive. Due to malfunctioning equipment, it was impossible to repeat the experiments to include photoelectrochemistry of Sulphur annealed electrodes. The efficiencies of the electrodes annealed in different environments are compared to the current state-of-the-art for photoelectrochemical solar fuels.

The purpose of the annealing steps, described in Chapter 4, was to alter the surface defect state energy levels to a more preferential architecture. If the V_s on the surface of the FeS_2 nanoparticles are passivated, the photocurrent density and Hydrogen evolved will both be improved. This improvement would be due to a reduction in electron traps leading to a decrease in electron-hole recombination. As discussed in Chapter 4, the stability of the electrodes has been improved. However, they are still unstable and therefore not suitable for multiple measurements. To negate the effect of variables from electrodes annealed in different atmospheres being synthesised in separate batches, a stock solution was obtained

by mixing six separate syntheses together by sonication. As the time taken to complete six syntheses was several days, it was necessary to characterise the crystal structure of the nanoparticles in the resultant stock solution, to be certain there was no material degradation or oxidation. Figure 5-1 shows Raman spectroscopy and XRD used to confirm the crystallinity and phase purity of the stock solution.

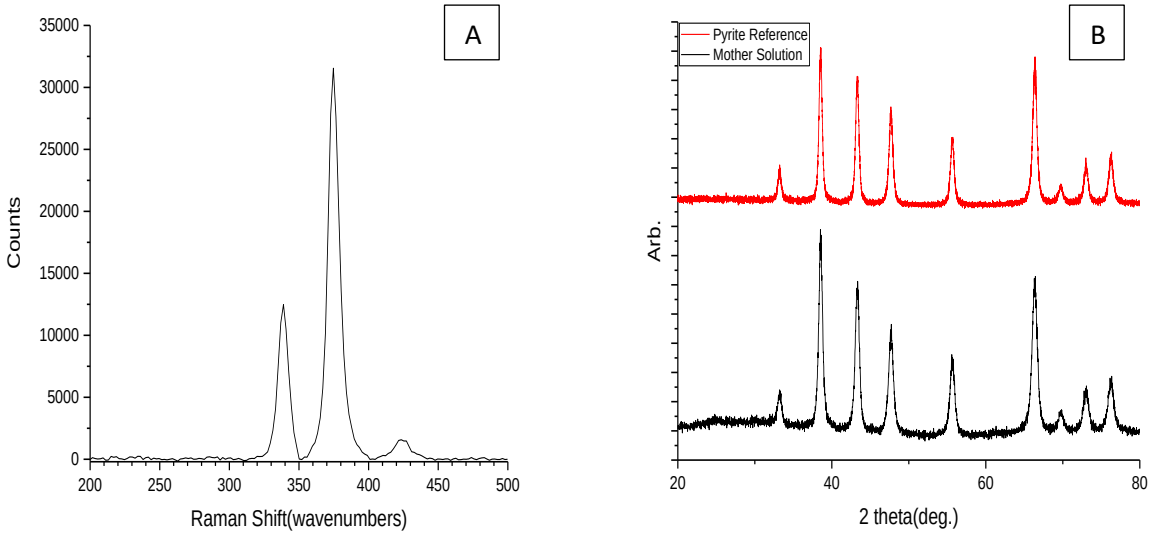

Figure 5-1-(A) Raman spectroscopy of the stock solution of FeS_2 nanocrystals under 532 nm laser excitation. (B) XRD of the stock solution of FeS_2 nanocrystals (black) compared to a reference spectrum (red) of a previous batch known to be FeS_2 Pyrite.

In Figure 5-1A the peaks showing a Raman shift of 427cm^{-1}, 379cm^{-1} and 343cm^{-1} correspond to the T_g, A_g and E_g Raman active modes of FeS_2(P) [160]. There is no presence of Raman shifts from other Iron and Sulphur phases [161]. Figure 5-1B compares XRD taken of the stock solution to a diffractogram of a material known to be FeS_2. All diffraction peaks present in the diffractogram correspond to that of FeS_2(P) [162]. After synthesis and characterisation of the material, substrates were deposited by dynamic spin coating, according to the method described in Chapter 2.7. ITO/FeS_2 electrodes were annealed in Nitrogen and Hydrogen using the method described in Chapter 2.11.1.

To confirm that FeS_2(P) thin films were still in Pyrite form after annealing and ALD, Raman spectra were taken. Figure 5-2 compares Raman spectra taken of FeS_2(P) thin films after Nitrogen and Hydrogen annealing and the deposition of 3 nm of TiO_2 via ALD. The process for the deposition of 3 nm of TiO_2 is described in Chapter 2.8. All peaks in the Raman for both Nitrogen and Hydrogen annealed samples coincide with those reported in the literature for FeS_2(P)[160].

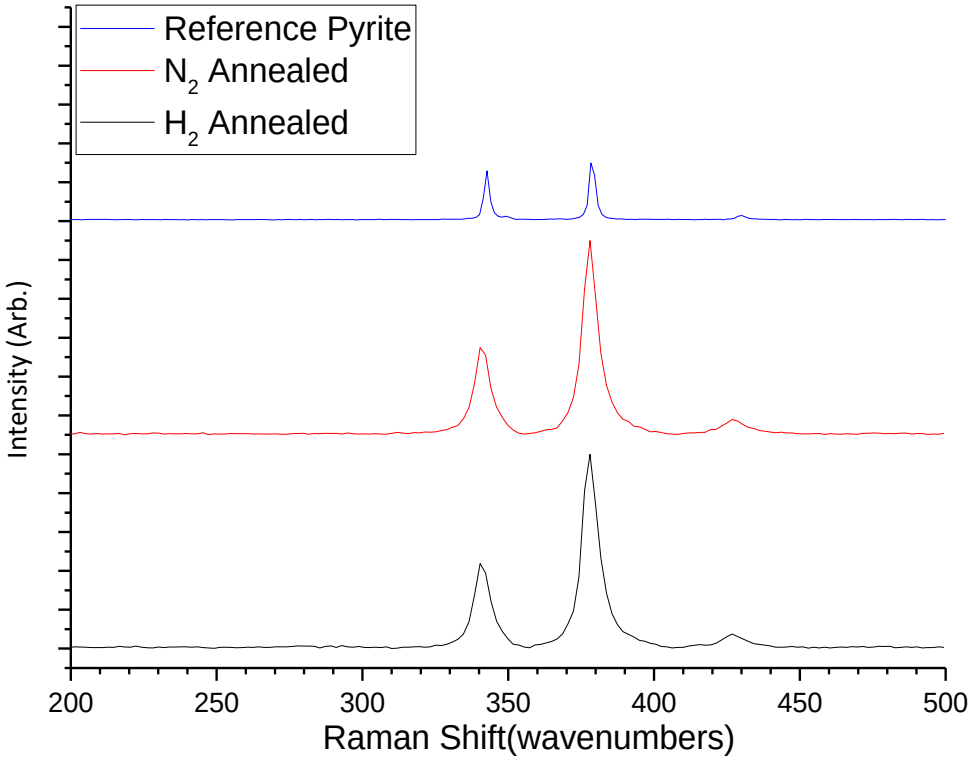

Figure 5-2-Comparison of Raman spectroscopy taken after Hydrogen annealing (black), Nitrogen annealing (red) and a reference spectra (blue) for FeS_2(P). Both Nitrogen and Hydrogen spectra were taken after ALD of 3nm of TiO_2.

To measure the photocurrent response and lifetime of the photocurrent, FeS_2 films annealed under Nitrogen and Hydrogen were measured under chopped illumination conditions. Electrodes were held at a constant bias of -0.19 V vs RHE in a working electrolyte of pH 7, 0.1M phosphate buffer solution, with a Pt counter electrode. Electrodes were illuminated by a 340 W Xe lamp with a water filter and a 450nm long-pass filter.

Figure 5-3 shows chopped illumination and constant illumination data for electrodes annealed in Hydrogen and Nitrogen atmospheres. Key values obtained by analysing the graphs in Figure 5-3 are displayed in Table 5-1. Figures 5-3A and B compare the chopped illumination from Hydrogen annealed samples and Nitrogen annealed samples, respectively. The maximum photocurrent response for Nitrogen annealed samples outperformed that of the Hydrogen annealed samples, with Nitrogen annealed samples demonstrating a photocurrent of 80 μA and Hydrogen annealed only achieving 30 μA. This decrease in photocurrent response can be attributed to an increase in surface Sulphur defect states on the FeS_2 nanoparticles, as a result of Hydrogen annealing, as discussed in Chapter 4.3. The trap states would lead to an increase in electron-hole recombination, reducing the photocurrent output of the Hydrogen annealed FeS_2 thin films. When the illumination from the Xe lamp is stopped, a slow decrease in the negative photocurrent density is observed for both Nitrogen and Hydrogen annealed electrodes. For the majority of electrodes reported, this decrease should happen on the order of μseconds to seconds [15], [163]–[165]. Therefore, ideally, the photocurrent decay should follow a square wave function under chopped illumination. However, this is not what is observed for the FeS_2 photoelectrode system, instead there are very long relaxation times. These long relaxation times, ranging from 35-130 seconds, are attributed to poor carrier transport kinetics, originating from trapped charge carriers [166]. The charge carriers trapped at the surface result in an increased bulk to surface energy barrier, due to the increased band bending from trapped charge carriers in the depletion region. This process, in turn, slows transport of photo-generated charge carriers to the surface [167]. To compare the photocurrent relaxation time of the Nitrogen and Hydrogen annealed electrodes, the decay curve is fitted using an exponential decay function. The values for the time constant of the exponential decay curve are reported in Table 5-1.

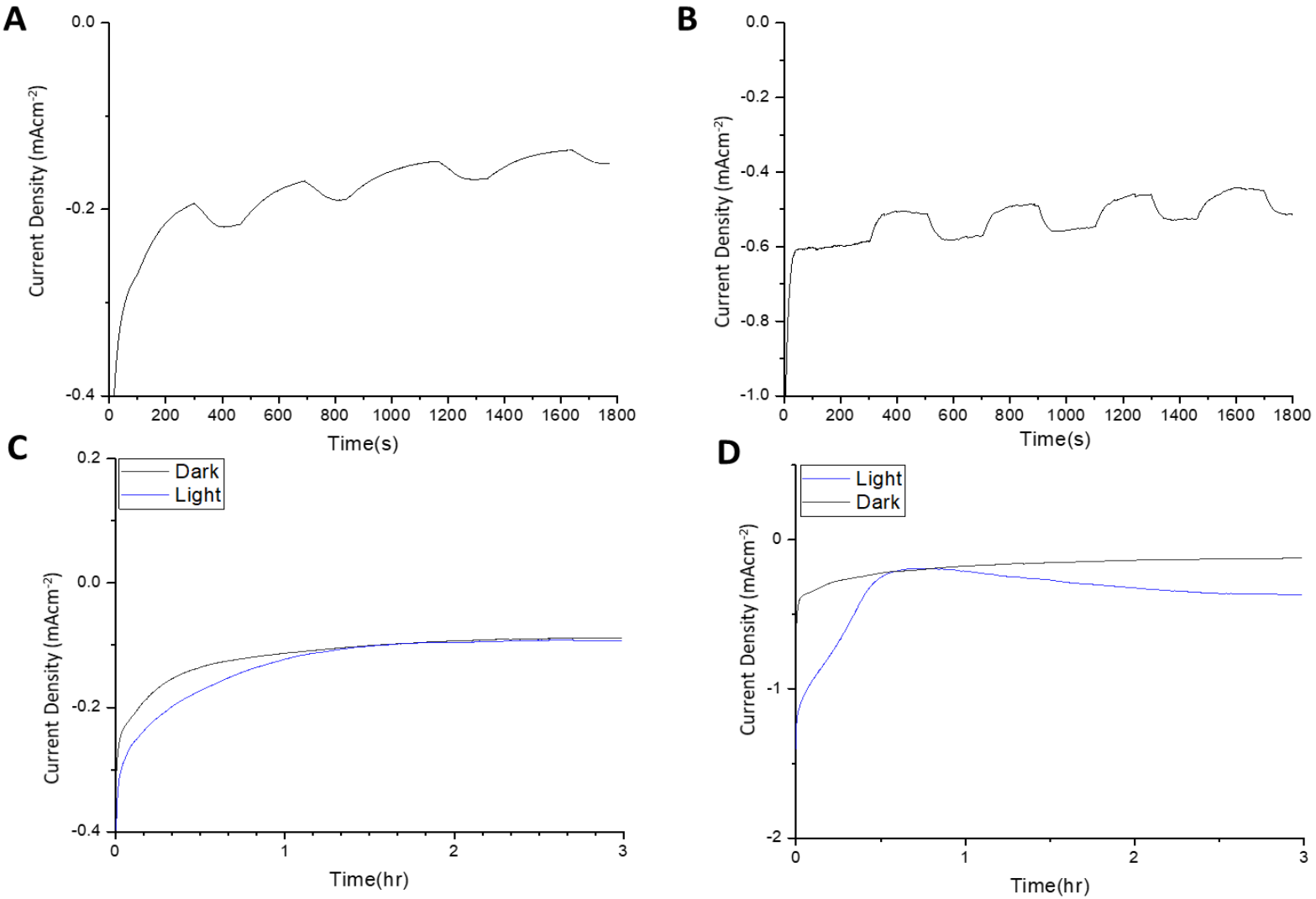

Figure 5-3- Transient illumination photoelectrochemistry of FeS_2 thin film annealed in (A) Hydrogen atmosphere, (B) Nitrogen atmosphere. Comparison of photoelectrochemistry of FeS_2 electrodes held at constant bias of -0.19 vs. RHE under light (blue) and dark (black) conditions annealed in (C) Hydrogen and (D) Nitrogen atmospheres.

Annealing atmosphere	H_2 moles produced (µm)		FE		Max photocurrent (µA)	PRT(s)
	Light	***Dark***	***Light***	***Dark***	***On***	***Chopped***
Nitrogen	10.18	4.20	0.5	0.42	80	34.00
Hydrogen	3.67	2.14	0.51	0.33	30	129.86

Table 5-1- Key values obtained via the analysis of graphs in Figure 5-3. Hydrogen values are obtained through gas chromatography. Faradaic Efficiencies (FE) are calculated using the equation for FE in Chapter 2.1. Max Photocurrent is calculated using the difference in dark and illumination conditions in chopped illumination experiments and Photocurrent Retention Time (PRT) is calculated via fitting the decay curve with a exponential decay function.

To confirm this reduced ability, the amount of Hydrogen produced by Nitrogen and Hydrogen annealed electrodes in dark and illumination conditions was measured. Table 5-1 presents the amount of Hydrogen, in µmoles, produced by Hydrogen and Nitrogen annealed electrodes. Ideally, the amount of Hydrogen produced in the dark would be zero. However, the bias potential required to allow FeS_2 to produce Hydrogen is more than that required to electrochemically drive the reaction on the Pt catalyst. Therefore, the Hydrogen production mechanism here is more of an enhancement process, rather than a reaction solely driven by light absorbed by FeS_2. Under illumination conditions, FeS_2 electrodes annealed in Nitrogen atmospheres produced 10.8 µmol of Hydrogen compared to 3.67 µmol of Hydrogen produced by Hydrogen annealed electrodes. As this is an enhancement process, the more meaningful result is the difference between Hydrogen produced under illumination and dark conditions. Nitrogen annealed electrodes produced 5.98 µmol more Hydrogen under

illumination than in the dark, compared to Hydrogen annealed electrodes producing only 1.59 µmol more.

This result shows that the Hydrogen annealing process does indeed decrease the ability of FeS_2 to drive a Hydrogen evolution reaction (HER). The values for Nitrogen leak rates were monitored as well as Hydrogen evolution. The reason this is important, is that no leak is one way, and if Nitrogen is leaking in, Hydrogen will also be leaking out. For the experiment carried out on the Hydrogen annealed electrodes, the Nitrogen leak rates were approximately four times that for the Nitrogen annealed electrodes. Unfortunately, due to the extremely low leak rate, and low-pressure differential, equations to back-calculate Hydrogen amounts yielded anomalously high values. Fortunately, the difference in Nitrogen leak rates for Hydrogen and Nitrogen annealed electrodes under different illumination conditions is small. Therefore, a comparison of the ratio between Hydrogen produced under illumination and Hydrogen produced in dark conditions would be more accurate. The ratio of Hydrogen produced in the light, compared to that produced in the dark, for Nitrogen and Hydrogen annealed electrodes is 2.42 and 1.72 respectively. This is a more accurate confirmation that annealing FeS_2 electrodes in Hydrogen reduces the photoactivity of FeS_2 thin films. The Faradaic Efficiency (FE), as defined in Chapter 2.1.5 and shown in Table 5-1, is nominally unchanged for Nitrogen and Hydrogen annealed electrodes under illumination. This means that even though the total amount of Hydrogen produced has decreased for Hydrogen annealed electrodes, the proportion of electrons transferred over the solid-liquid interface going to Hydrogen evolution is unchanged. As the majority of electrons not directed towards the HER can be attributed to unwanted side reactions, this shows that Hydrogen annealing has not compromised FeS_2s chemical stability. All reductions in activity, therefore, can be attributed to the altering of electronic structure.

5.1 Conclusions and further work

In this chapter, I have discussed the differences between the photoelectrochemistry of electrodes annealed in Hydrogen and Nitrogen atmospheres. The best performing electrode was found to be one annealed in Nitrogen with a 3 nm overlayer of TiO_2 and a Pt co-catalyst. Under illumination, the electrode demonstrated a peak photocurrent of 80 μA and produced 3.39 μmoles of Hydrogen per hour, with a FE of 0.5 at a bias of -0.19 vs. RHE. This corresponds to a peak solar-to-hydrogen (STH) conversion efficiency of 0.06%. However, the highest STH conversion efficiency for a photocathode with a single absorber layer is 18.5% [46]. Although the efficiency of the FeS_2 electrode presented here is much less than this, the results presented here are the only reported case of a photocathode with FeS_2 nanoparticles as the sole photo absorber. Previous to this, the only examples of FeS_2 on a photocathode present the material as a sensitiser to another photoactive material[168].

One downside of investigating the improvements to FeS_2s photoelectrochemistry with the electrochemical method described in this chapter, was the amount of work necessary to first stabilise it in water (as discussed in Chapter 4). Whilst stabilisation of FeS_2 in aqueous conditions is an important obstacle to be overcome, FeS_2 reacts with water in electrochemical experiments which may cause anomalous results. A better method for the investigation of annealing effects on the photoelectrochemistry of FeS_2, would be to perform the measurements in non-aqueous environments. This would remove the possibility of decomposition reactions that may interfere with the experiment. As such, further experimentation with FeS_2 could benefit from performing the experiments in non-aqueous solvents, with sacrificial electron scavengers whose decomposition can be detected, for example, methylene blue. This would allow for easier de-convolution of electrochemical effects due to different annealing environments and reactions between FeS_2 and H_2O.

Whilst a step towards the use of FeS_2 as a photocathode in solar water splitting has been made, much more could be done to increase its efficiency. Firstly, as shown in the XPS in Chapter 4, Hydrogen annealing does not significantly alter FeS_2s defect state chemistry. Sulphur annealing, however, did show improvements to the relative concentration of defect states on FeS_2s surface. Therefore, experiments to assess any improvements to the photoelectrochemistry of FeS_2 after Sulphur annealing would be worthwhile. As FeS_2 is comprised of earth-abundant elements, even a small increase to its efficiency could make it an alternative candidate for some industrial applications of Hydrogen production, where cost is a higher priority than efficiency. Secondly, the FeS_2 quantum dots synthesized in Chapter 3, in conjunction with Sulphur annealing, which decreases defect state density, have the potential to improve FeS_2s photoelectrochemistry. The increase in bandgap from quantum confinement (shown in Chapter 3), would increase the theoretical efficiency achievable with a FeS_2 photocathode. The increase in defect state density, due to the increased surface to volume ratio, could be counteracted by Sulphur annealing. The increased bandgap of FeS_2 due to quantum confinement would allow for thicker over-layers of TiO_2, which would also improve charge separation. With FeS_2 quantum dots on the cathode side, it would also be possible to have Fe_2O_3 as a photoanode to drive overall water splitting reaction.

6 Conclusions and Recommendation for Future Work

The aim of this thesis was to understand and provide solutions for the three significant problems with FeS_2 as a photocathode, in a photoelectrochemical water splitting cell. These problems were; a bandgap too small to drive unbiased water-splitting reactions, a high density of defect states and instability in aqueous solutions. While these problems are difficult to overcome, the potential benefits that would occur from overcoming them are significant. FeS_2 is comprised of cheap earth-abundant materials and has a high absorption coefficient, meaning only 100 nm of material is needed to absorb 95% of the incident solar spectrum in the visible range. Therefore, if the problems with FeS_2 could be overcome, it would make a very promising candidate for a photocathode material in a solar fuels cell.

Chapter 3 of this thesis focuses on finding a solution to the first of the three problems outlined above; the bandgap of FeS_2, which is too small to drive the water-splitting reaction without external bias. To increase the bandgap of a material one direction which can be taken is to synthesise the material in a form which exhibits quantum confinement. One of the benefits of this method is to increase the surface area per gram of photoactive material, which could help to increase the activity per gram of a photocathode. Two different synthetic routes to FeS_2 quantum dots were developed. One route used an inverse micelle synthesis where nano-sized water droplets are stabilised in an oil phase using surfactants. Salts are then dispersed in the water phase and the reaction is confined to the size of the inverse micelles. The second route used a heat-up synthesis where precursors are mixed at room temperature and heated up. The reaction is then refluxed for a defined amount of time, in this example, one and a half hours. Both synthetic methods produced FeS_2 quantum dots, with an absorption spectrum corresponding to particles 3.5 nm in diameter. The bandgap of particles of this size was approximately 1.5eV, which also corresponds with the bandgap associated with the highest possible theoretical efficiency for solar-to-hydrogen conversion

(discussed in Chapter 2). One problem with utilising these methods to broaden FeS_2s bandgap is that, 3.5nm FeS_2 nanoparticles are very unstable in the presence of Oxygen and water. This increased instability leads to processability problems in constructing electrodes for photoelectrochemical testing. Another problem with quantum confinement is the increased surface to volume ratio. The result is an increase in the ratio of surface defect states to fully co-ordinated Iron and Sulphur atoms. This could potentially have negative implications for the photoelectrochemistry of the FeS_2 quantum dots, for example decreased stability. To improve the processability and stability of FeS_2 quantum dots, future work should focus on further modifications to the inverse micelle synthesis. Subsequent steps could be added to the inverse micelle synthesis to grow shells of a different material around a core of FeS_2. If this material was stable in atmospheric conditions, it would make FeS_2 quantum dots more processable. On top of this, another material could be deposited which could be catalytically active. As the size of the inverse micelle is dependent predominantly on the molar ratio of water to surfactant, the size of the micelles and hence the thickness of the over-layer can be precisely controlled.

Chapter 4 focuses on two of the three problems, how to decrease the density of FeS_2 defect states and increase its stability in the presence of aqueous solutions. Methods of electrode preparation were investigated, as one initial problem was the physical instability of FeS_2 thin films in solution. To increase the physical stability, annealing the prepared electrode in a vacuum and inert atmosphere was investigated. In addition to this, attaching FeS_2 chemically to the surface of ITO slides using Mercaptopropionic Acid was also investigated. The results showed FeS_2 films annealed in dried Nitrogen were the most physically stable films, lasting three hours. The improvements to chemical stability from the deposition of different over-layers of Al_2O_3 and TiO_2 were also investigated. The deposition conditions were optimised for Al_2O_3 and applied to the deposition of TiO_2. The findings pointed to TiO_2 providing the optimum balance of corrosion protection and retention of activity of the FeS_2(P) thin films.

We also examined the effect of the deposition of a Pt catalyst on the stability and activity of the thin film electrodes. Pt was deposited electrochemically, via an already published method [109]. The deposition of Pt increased both the stability of the electrodes, as well as the activity. The activity increase was due to the reduction in the required overpotential for the Hydrogen evolution reaction, however the reason for the stability increase could be due to one of two options. One reason could be increased surface passivation, due to the Pt deposition. Alternatively, the Pt catalyst could be providing a competing reaction pathway for the photogenerated electrons. This would reduce the number of electrons available to the corrosion reaction. The increase in the stability of the thin film electrodes is likely to be due to a mix of both scenarios. Further work in stabilising FeS_2 thin films should focus on finding a more suitable protective overlayer. TiO_2 was implemented here as a necessity, however, a passivating overlayer with a conduction band minimum below that of FeS_2(P) would be more suitable. This preferential band alignment would provide improved charge separation and allow for thicker over-layers to be deposited. Thicker over-layers would lead to an increase in the overall stability of a FeS_2 thin film photoelectrode. FeS_2s defect state chemistry was investigated by annealing electrodes in different annealing atmospheres. There was also a secondary goal of investigating whether the changes to defect state chemistry could be directly measured with XPS. The annealing of electrodes in Hydrogen and Nitrogen atmospheres was optimised. An annealing cell was developed to keep the annealing atmosphere inert, and a protocol for using the available Nitrogen lines was also developed to stop the introduction of atmospheric contaminants. The optimum Sulphur annealing atmosphere was also investigated. The photoelectrochemistry of the Nitrogen and Hydrogen annealed electrodes was compared, showing Hydrogen annealing to have detrimental effects on activity and stability. Electrodes annealed in Sulphur atmospheres could not be tested photoelectrochemically due to the Sulphur annealing process removing the conductivity of ITO. The defect states of FeS_2(P) electrodes annealed in Hydrogen,

Nitrogen and Sulphur environments were compared to each other. Due to the large statistical variation within the results, further work is needed. There was, however, a trend that suggested Hydrogen annealing resulted in a lower density of sulphur defects, although, due to the low activity, this is likely due to removing Sulphur, not passivating the defects. Nitrogen annealing also reduced the amount of dangling Sulphur bonds on the surface, but retained the density of surface disulphides. This is due to the outgassing of dangling Sulphur bonds requiring less energy than a disulphide. XPS on Sulphur annealed electrodes showed the removal of both types of Sulphur surface defect states.

Additional research should investigate the effect of inserting Oxygen into the Sulphur defect sites. This alteration would remove the inter-bandgap energy states [169], which are the cause of FeS_2s poor efficiency[80]. Three ways this could be attempted, are annealing in Oxygen environments, Oxygen plasma treatment or laser annealing. Annealing in Oxygen environments could be optimised at different temperatures, annealing times and Oxygen partial pressures. Oxygen plasma treatment could also be optimised using different powers and treatment times. Laser annealing to incorporate Oxygen into defect states has already been demonstrated for WSe_2 [170]. In this thesis, the annealed electrodes were tested in aqueous systems, as this was the reaction the electrodes were being optimised for. However, to test if the defect states were reducing the recombination rate of photogenerated holes, as a proof of concept, it is not necessary to test in aqueous conditions. The material can instead be tested in non-aqueous environments, reducing a chemical with a lower energy reduction potential. The work carried out here on Sulphur annealing could also be taken further. Substituting a more stable TCO for ITO would result in conducting FeS_2 thin films after Sulphur annealing which could be tested photoelectrochemically.

Chapter 5 compares the photoelectrochemistry of FeS_2 electrodes annealed in Hydrogen and Nitrogen environments, coated with a 3nm ALD layer of TiO_2 and an electrochemically

deposited Pt co-catalyst. FeS_2 photocathodes annealed in Nitrogen outperformed those annealed in Hydrogen, proving Hydrogen annealing to have a negative effect on FeS_2 with regards to driving a Hydrogen evolution reaction. TiO_2 coated electrodes had an overall efficiency of 0.06%, producing 3.39 µmol per hour at a bias of 0.19 V vs. RHE. Transient photoelectrochemistry showed long relaxation times for the photocurrent in both Hydrogen and Nitrogen annealed electrodes, as well as large dark currents. Long relaxation times are most likely due to trapping states caused by a large density of defect states. The large dark currents will predominantly be due to a reaction of FeS_2 with the electrolyte. To improve the efficiency of this material a combination of Sulphur annealing, to remove defect states, and/or larger protective over-layers could be used. This thesis has already outlined a suitable way to Sulphur anneal FeS_2 electrodes, with XPS suggesting the process removes Sulphur defect states. However, a suitable conductive substrate needs to be used as the Sulphur annealing process also removed ITOs conductivity. For thicker protective over-layers there are two potential directions. Firstly, instead of using bulk like FeS_2 nanoparticles, nanoparticles small enough to exhibit quantum confinement can be used. The increased bandgap would result in a shift in the conduction band minimum above that of TiO_2. The change in band alignment would mean thicker layers of TiO_2 could be used, resulting in a more stable electrode. Secondly, a material could be used in the protective over-layer which has a conduction band minimum below that of FeS_2. This would result in the same favourable band alignment discussed above. The method that would result in the highest efficiency, however, would be the first of these, as increasing the bandgap of FeS_2would also remove the need for an applied bias during photoelectrochemistry. As well as this, as discussed in previous chapters, increasing FeS_2s bandgap to 1.5eV, would mean it has the optimum bandgap for driving water splitting reactions.

Bibliography

[1] U. Energy Information Administration, “International Energy Outlook 2018 (IEO2018),” 2018.

[2] C. MacFarling Meure *et al.*, “Law Dome CO_2, CH_4 and N_2O ice core records extended to 2000 years BP,” *Geophys. Res. Lett.*, vol. 33, no. 14, p. L14810, 2006.

[3] D. Lüthi *et al.*, “High-resolution carbon dioxide concentration record 650,000–800,000 years before present,” *Nature*, vol. 453, no. 7193, pp. 379–382, 2008.

[4] “Title: World Nuclear Performance Report 2016 Produced by: World Nuclear Association,” 2016.

[5] O. Eriksson, Eriksson, and Ola, “Nuclear Power and Resource Efficiency—A Proposal for a Revised Primary Energy Factor,” *Sustainability*, vol. 9, no. 6, p. 1063, 2017.

[6] M. K. Hubbert, “Nuclear Energy and the Fossil Fuel,” 1956.

[7] M. Dittmar, “The end of cheap uranium,” *Sci. Total Environ.*, vol. 461–462, pp. 792–798, 2013.

[8] A. A. Harms, D. R. Kingdon, K. F. Schoepf, and G. H. Miley, *Principles of Fusion Energy*. WORLD SCIENTIFIC, 2000.

[9] K. Tokimatsu *et al.*, “Studies of breakeven prices and electricity supply potentials of nuclear fusion by a long-term world energy and environment model,” *Nucl. Fusion*, vol. 42, no. 11, pp. 1289–1298, 2002.

[10] T. Tanabe, “Introduction of a Nuclear Fusion Reactor,” in *Tritium: Fuel of Fusion Reactors*, Tokyo: Springer Japan, 2017, pp. 3–25.

[11] E. and I. S. Department for Business, “UK Energy Statistics, Q1 2018 Trends in the use of renewable energy,” no. June, pp. 1–14, 2018.

[12] E. Kabir, P. Kumar, S. Kumar, A. A. Adelodun, and K.-H. Kim, “Solar energy: Potential and future prospects,” *Renew. Sustain. Energy Rev.*, vol. 82, pp. 894–900, 2018.

[13] J. Tsao, B. E. Science, N. Lewis, and G. Crabtree, “Solar FAQs,” pp. 1–24, 2006.

[14] D. M. Lemoine, D. M. Kammen, and A. E. Farrell, “An innovation and policy agenda for commercially competitive plug-in hybrid electric vehicles,” *Environ. Res. Lett.*, vol. 3, no. 1, p. 014003, 2008.

[15] J. Luo, L. Steier, M. K. Son, M. Schreier, M. T. Mayer, and M. Grätzel, “Cu2O Nanowire Photocathodes for Efficient and Durable Solar Water Splitting,” *Nano Lett.*, vol. 16, no. 3, pp. 1848–1857, 2016.

[16] E. E. Barton, D. M. Rampulla, and A. B. Bocarsly, “Selective Solar-Driven Reduction of CO_2 to Methanol Using a Catalyzed p-GaP Based Photoelectrochemical Cell,” *J. Am. Chem. Soc.*, vol. 130, no. 20, pp. 6342–6344, 2008.

[17] J. Wei *et al.*, “Directly converting CO2 into a gasoline fuel,” *Nat. Commun.*, vol. 8, p. 15174, 2017.

[18] Element Energy Ltd., “Carbon Low Growth At Vehicles,”, 2016.

[19] A. C. Nielander, M. R. Shaner, K. M. Papadantonakis, S. A. Francis, and N. S. Lewis, “A taxonomy for solar fuels generators,” *Energy Environ. Sci.*, vol. 8, no. 1, pp. 16–25, 2015.

[20] J. Shen, Y. Hu, C. Li, C. Qin, and M. Ye, “Pt–Co supported on single-walled carbon nanotubes as an anode catalyst for direct methanol fuel cells,” *Electrochim. Acta*, vol. 53, no. 24, pp. 7276–7280, 2008.

[21] M. Schreier, J. Luo, P. Gao, T. Moehl, M. T. Mayer, and M. Grätzel, “Covalent Immobilization of a Molecular Catalyst on Cu2O Photocathodes for CO2Reduction,” *J. Am. Chem. Soc.*, vol. 138, no. 6, pp. 1938–1946, 2016.

[22] K. Ueda *et al.*, “Photoelectrochemical oxidation of water using BaTaO2N photoanodes prepared by particle transfer method,” *J. Am. Chem. Soc.*, vol. 137, no. 6, pp. 2227–2230, 2015.

[23] N. P. Dasgupta, C. Liu, S. Andrews, F. B. Prinz, and P. Yang, “Atomic layer deposition of platinum catalysts on nanowire surfaces for photoelectrochemical water reduction,” *J. Am. Chem. Soc.*, vol. 135, no. 35, pp. 12932–12935, 2013.

[24] B. D. James, G. N. Baum, J. Perez, and K. N. Baum, “Technoeconomic Analysis of Photoelectrochemical (PEC) Hydrogen Production,” vol. 22201, 2009.

[25] D. Liang *et al.*, “Efficient H2production in a microbial photoelectrochemical cell with a composite Cu2O/NiOxphotocathode under visible light,” *Appl. Energy*, vol. 168, pp. 544–549, 2016.

[26] Gunawan *et al.*, “Platinum and indium sulfide-modified CuInS2as efficient photocathodes for photoelectrochemical water splitting,” *Chem. Commun.*, vol. 50, no. 64, pp. 8941–8943, 2014.

[27] S. Kamimura, M. Higashi, R. Abe, and T. Ohno, “Fabrication of a porous ZnRh2O4 photocathode for photoelectrochemical water splitting under visible light irradiation and a significant effect of surface modification by ZnO necking treatment,” *J. Mater. Chem. A*, vol. 4, no. 16, pp. 6116–6123, 2016.

[28] E. Irtem *et al.*, “A photoelectrochemical flow cell design for the efficient CO2 conversion to fuels,” *Electrochim. Acta*, vol. 240, pp. 225–230, Jun. 2017.

[29] K. Rajeshwar, M. Kaneko, and A. Yamada, “Regenerative Photoelectrochemical Cells Using Polymer-Coated n-GaAs Photoanodes in Contact with Aqueous Electrolytes,” *J. Electrochem. Soc.*, vol. 130, no. 1, p. 38, Jan. 1983.

[30] Akira Fujishima and kenichi Honda, “Electrochemical photolysis of water at a semiconductor electrode,” *Nature*, vol. 238, p. 37, 1972.

[31] B. O’Regan and M. Gratzel, “A Low-Cost, High-Efficiency Solar-Cell Based on Dye-Sensitized Colloidal TiO_2 Films,” *Nature*, vol. 353, no. 6346, pp. 737–740, 1991.

[32] A. A. Dubale *et al.*, “A highly stable CuS and CuS-Pt modified Cu2O/CuO heterostructure as an efficient photocathode for the hydrogen evolution reaction,” *J. Mater. Chem. A*, vol. 4, no. 6, pp. 2205–2216, 2016.

[33] J. Su *et al.*, "CdTe-Based Photoanode for Oxygen Evolution from Water under Simulated Sunlight," *J. Phys. Chem. Lett.*, vol. 8, no. 23, pp. 5712–5717, 2017.

[34] S. Y. Chae, P. Sudhagar, A. Fujishima, Y. J. Hwang, and O.-S. Joo, "Improved photoelectrochemical water oxidation kinetics using a TiO_2 nanorod array photoanode decorated with graphene oxide in a neutral pH solution," *Phys. Chem. Chem. Phys.*, vol. 17, no. 12, pp. 7714–7719, 2015.

[35] J. Zhang *et al.*, "WO_3 photoanodes with controllable bulk and surface oxygen vacancies for photoelectrochemical water oxidation," *J. Mater. Chem. A*, vol. 6, no. 8, pp. 3350–3354, 2018.

[36] H. S. Han *et al.*, "Boosting the solar water oxidation performance of a $BiVO_4$ photoanode by crystallographic orientation control," *Energy Environ. Sci.*, vol. 11, no. 5, pp. 1299–1306, 2018.

[37] G. Wang *et al.*, "Enhancing and stabilizing α-Fe2O3 photoanode towards neutral water oxidation: Introducing a dual-functional NiCoAl layered double hydroxide overlayer," *J. Catal.*, vol. 359, pp. 287–295, 2018.

[38] C. Jiang, S. J. A. Moniz, A. Wang, T. Zhang, and J. Tang, "Photoelectrochemical devices for solar water splitting-materials and challenges," *Chem. Soc. Rev*, vol. 46, p. 4645, 2017.

[39] J. Han, X. Zong, X. Zhou, and C. Li, "Cu2O/CuO photocathode with improved stability for photoelectrochemical water reduction," *RSC Adv.*, vol. 5, no. 14, pp. 10790–10794, 2015.

[40] C. G. Morales-Guio, L. Liardet, M. T. Mayer, S. D. Tilley, M. Grätzel, and X. Hu, "Photoelectrochemical hydrogen production in alkaline solutions using Cu2O coated with earth-abundant hydrogen evolution catalysts," *Angew. Chemie - Int. Ed.*, vol. 54, no. 2, pp. 664–667, 2015.

[41] B. Kim *et al.*, "A highly efficient Cu(In,Ga)(S,Se)2 photocathode without a hetero-materials overlayer for solar-hydrogen production," *Sci. Rep.*, vol. 8, no. 1, p. 5182, 2018.

[42] F. Jiang *et al.*, "Pt/In_2S_3/CdS/Cu_2ZnSnS_4 Thin Film as an Efficient and Stable Photocathode for Water Reduction under Sunlight Radiation," *J. Am. Chem. Soc.*, vol. 137, no. 42, pp. 13691–13697, 2015.

[43] C. Malerba, F. Biccari, C. Leonor Azanza Ricardo, M. D'Incau, P. Scardi, and A. Mittiga, "Absorption coefficient of bulk and thin film Cu2O," *Sol. Energy Mater. Sol. Cells*, vol. 95, no. 10, pp. 2848–2854, 2011.

[44] Takeo Arai, Masatoshi Yanagida, Yoshinari Konishi, Yasukazu Iwasaki, and Hideki Sugihara, and Kazuhiro Sayama, "Efficient Complete Oxidation of Acetaldehyde into CO2 over CuBi2O4/WO3 Composite Photocatalyst under Visible and UV Light Irradiation," 2007.

[45] J. Jia *et al.*, "Solar water splitting by photovoltaic-electrolysis with a solar-to-hydrogen efficiency over 30%," *Nat. Commun.*, vol. 7, no. 1, p. 13237, 2016.

[46] W. H. Cheng *et al.*, "Monolithic Photoelectrochemical Device for Direct Water Splitting with 19% Efficiency," *ACS Energy Lett.*, 2018.

[47] C. Wadia, A. P. Alivisatos, and D. M. Kammen, “Materials Availability Expands the Opportunity for Large-Scale Photovoltaics Deployment,” *Environ. Sci. Technol.*, vol. 43, no. 6, pp. 2072–2077, 2009.

[48] H. Kobayashi *et al.*, “Development of highly efficient $CuIn_{0.5}Ga_{0.5}Se_2$-based photocathode and application to overall solar driven water splitting,” *Energy Environ. Sci.*, vol. 11, no. 10, pp. 3003–3009, 2018.

[49] P. Dias *et al.*, “Transparent Cuprous Oxide Photocathode Enabling a Stacked Tandem Cell for Unbiased Water Splitting,” *Adv. Energy Mater.*, vol. 5, no. 24, p. 1501537, 2015.

[50] L. Pan *et al.*, “Boosting the performance of Cu2O photocathodes for unassisted solar water splitting devices,” *Nat. Catal.*, vol. 1, no. 6, pp. 412–420, 2018.

[51] Y. J. Jang, Y. Bin Park, H. E. Kim, Y. H. Choi, S. H. Choi, and J. S. Lee, “Oxygen-Intercalated $CuFeO_2$ Photocathode Fabricated by Hybrid Microwave Annealing for Efficient Solar Hydrogen Production,” *Chem. Mater.*, vol. 28, no. 17, pp. 6054–6061, 2016.

[52] J. Li, M. Griep, Y. Choi, and D. Chu, “Photoelectrochemical overall water splitting with textured $CuBi_2O_4$ as a photocathode,” *Chem. Commun.*, vol. 54, no. 27, pp. 3331–3334, 2018.

[53] W. Yang, Y. Oh, J. Kim, M. J. Jeong, J. H. Park, and J. Moon, “Molecular Chemistry-Controlled Hybrid Ink-Derived Efficient Cu_2ZnSnS_4 Photocathodes for Photoelectrochemical Water Splitting,” *ACS Energy Lett.*, vol. 1, no. 6, pp. 1127–1136, 2016.

[54] C. Ros, T. Andreu, S. Giraldo, V. Izquierdo-Roca, E. Saucedo, and J. R. Morante, “Turning Earth Abundant Kesterite-Based Solar Cells Into Efficient Protected Water-Splitting Photocathodes,” *ACS Appl. Mater. Interfaces*, vol. 10, no. 16, pp. 13425–13433, 2018.

[55] D. Shin, E. Ngaboyamahina, Y. Zhou, J. T. Glass, and D. B. Mitzi, “Synthesis and Characterization of an Earth-Abundant $Cu_2BaSn(S,Se)_4$ Chalcogenide for Photoelectrochemical Cell Application,” *J. Phys. Chem. Lett.*, vol. 7, no. 22, pp. 4554–4561, 2016.

[56] J. Ge and Y. Yan, “Synthesis and characterization of photoelectrochemical and photovoltaic Cu_2BaSnS_4 thin films and solar cells,” *J. Mater. Chem. C*, vol. 5, no. 26, pp. 6406–6419, 2017.

[57] Y. Zhou *et al.*, “Efficient and Stable $Pt/TiO_2/CdS/Cu_2BaSn(S,Se)_4$ Photocathode for Water Electrolysis Applications,” *ACS Energy Lett.*, vol. 3, no. 1, pp. 177–183, 2018.

[58] W. Yang *et al.*, “Adjusting the Anisotropy of 1D Sb_2Se_3 Nanostructures for Highly Efficient Photoelectrochemical Water Splitting,” *Adv. Energy Mater.*, vol. 8, no. 14, p. 1702888, 2018.

[59] J. Tan, W. Yang, Y. Oh, H. Lee, J. Park, and J. Moon, “Controlled Electrodeposition of Photoelectrochemically Active Amorphous MoS_x Cocatalyst on Sb_2Se_3 Photocathode,” *ACS Appl. Mater. Interfaces*, vol. 10, no. 13, pp. 10898–10908, 2018.

[60] L. Zhang *et al.*, “Scalable Low-Band-Gap Sb_2Se_3 Thin-Film Photocathodes for Efficient

Visible–Near-Infrared Solar Hydrogen Evolution," *ACS Nano*, vol. 11, no. 12, pp. 12753–12763, 2017.

[61] X. Sheng, L. Chen, T. Xu, K. Zhu, and X. Feng, "Understanding and removing surface states limiting charge transport in TiO 2 nanowire arrays for enhanced optoelectronic device performance," 2016.

[62] L. Santinacci, "ALD for Photoelectrochemical Water Splitting," in *Atomic Layer Deposition in Energy Conversion Applications*, Weinheim, Germany: Wiley-VCH Verlag GmbH & Co. KGaA, pp. 225–257, 2017.

[63] F. K. Shan and Y. S. Yu, "Band gap energy of pure and Al-doped ZnO thin films," *J. Eur. Ceram. Soc.*, vol. 24, no. 6, pp. 1869–1872, 2004.

[64] M. Khalid, "Tailoring of the Band Gap in Transition Metal-doped ZnO: First Principle Calculations," *Mater. Today Proc.*, vol. 2, no. 10, pp. 5246–5250, 2015.

[65] V. Biju, T. Itoh, A. Anas, A. Sujith, and M. Ishikawa, "Semiconductor quantum dots and metal nanoparticles: syntheses, optical properties, and biological applications.," *Anal. Bioanal. Chem.*, vol. 391, no. 7, pp. 2469–95, 2008.

[66] J. Patel, "Simple Non-aqueous Fabrication Route for Oleic Acid Capped Luminescent Cadmium Sulphide Quantum Dots at Relatively Low Temperature," *Soft Nanosci. Lett.*, vol. 01, no. 03, pp. 61–65, 2011.

[67] G. Müller, "Semiconductor Quantum Dots and Its Band Structure Parameters : An Introduction," *Structure*, pp. 1–42, 2004.

[68] S. Baskoutas and A. F. Terzis, "Size-dependent band gap of colloidal quantum dots," *J. Appl. Phys.*, vol. 99, no. 1, p. 013708, 2006.

[69] N. M. B. Cogan, C. Liu, F. Qiu, R. Burke, and T. D. Krauss, "Ultrafast dynamics of colloidal semiconductor nanocrystals relevant to solar fuels production,", vol. 10193, p. 101930B, 2017.

[70] D. Banjara, Y. Malozovsky, L. Franklin, and D. Bagayoko, "Defect energy levels and electronic behavior of Ni-, Co-, and As-doped synthetic pyrite," *J. Chem. Phys.*, vol. 8, no. 2, p. 25103, 2018.

[71] "List of Elements of the Periodic Table - Sorted by Abundance in Earth's crust." Available: https://www.science.co.il/elements/?s=Earth.

[72] S. Khalid, M. Azad Malik, D. J. Lewis, P. Kevin, E. Ahmed, and Y. Khan, "Transition metal doped pyrite (FeS 2) thin films: structural properties and evaluation of optical band gap energies," *J. Mater. Chem. C*, vol. 3, p. 12068, 1206.

[73] A. Ennaoui and H. Tributsch, "Iron sulphide solar cells," *Sol. Cells*, vol. 13, no. 2, pp. 197–200, 1984.

[74] P. P. Altermatt, T. Kiesewetter, K. Ellmer, and H. Tributsch, "Specifying targets of future research in photovoltaic devices containing pyrite (FeS2) by numerical modelling," *Sol. Energy Mater. Sol. Cells*, vol. 71, no. 2, pp. 181–195, 2002.

[75] E. O. Chukwuocha, M. C. Onyeaju, and T. S. T. Harry, "Theoretical Studies on the Effect of Confinement on Quantum Dots Using the Brus Equation," *World J. Condens. Matter*

Phys., vol. 02, no. 02, pp. 96–100, 2012.

[76] R. Koole, E. Groeneveld, D. Vanmaekelbergh, A. Meijerink, and C. de Mello Donegá, "Size Effects on Semiconductor Nanoparticles," in *Nanoparticles*, Berlin, Heidelberg: Springer Berlin Heidelberg, pp. 13–51, 2014.

[77] M. Cabán-Acevedo *et al.*, "Ionization of high-density deep donor defect states explains the low photovoltage of iron pyrite single crystals," *J. Am. Chem. Soc.*, vol. 136, no. 49, pp. 17163–17179, 2014.

[78] A. Krishnamoorthy, F. W. Herbert, S. Yip, K. J. Van Vliet, and B. Yildiz, "Electronic states of intrinsic surface and bulk vacancies in FeS2," *J. Phys. Condens. Matter*, vol. 25, no. 4, 2013.

[79] M. Bronold, C. Pettenkofer, and W. Jaegermann, "Surface photovoltage measurements on pyrite (100) cleavage planes: Evidence for electronic bulk defects," *J. Appl. Phys.*, vol. 76, no. 10, pp. 5800–5808, 1994.

[80] M. Cabán-Acevedo *et al.*, "Ionization of High-Density Deep Donor Defect States Explains the Low Photovoltage of Iron Pyrite Single Crystals," *J. Am. Chem. Soc.*, vol. 136, no. 49, pp. 17163–17179, 2014.

[81] W. Jaegermann and H. Tributsch, "Photoelectrochemicai reactions of FeS2 (pyrite) with t120 and reducing agents," 1983.

[82] C. Guo, X. Tong, and X. Guo, "Solvothermal synthesis of FeS2 nanoparticles for photoelectrochemical hydrogen generation in neutral water," *Mater. Lett.*, vol. 161, pp. 220–223, 2015.

[83] T. K. Trinh, N. T. N. Truong, V. T. H. Pham, H. Kim, and C. Park, "Effect of sulfur annealing on the morphological, structural, optical and electrical properties of iron pyrite thin films formed from FeS2 nano-powder," *Korean J. Chem. Eng.*, vol. 35, no. 7, pp. 1525–1531, 2018.

[84] J. P. Wilcoxon, P. P. Newcomer, and G. A. Samara, "Strong Quantum Confinement Effects In Semiconductors: Fes_2 Nanoclusters," Solid State Communication, 1996.

[85] P. Hofmann, *Solid State Physics : An Introduction*., 2008.

[86] R. F. Pierret, "Advanced Semiconductor Fundamentals," *Book*, vol. 121, no. 7, p. 221, 1987.

[87] F. K. Shan and Y. S. Yu, "Band gap energy of pure and Al-doped ZnO thin films," *J. Eur. Ceram. Soc.*, vol. 24, no. 6, pp. 1869–1872, 2004.

[88] S. K. Poznyak *et al.*, "Size-dependent electrochemical behavior of thiol-capped CdTe nanocrystals in aqueous solution.," *J. Phys. Chem. B*, vol. 109, no. 3, pp. 1094–100, 2005.

[89] R. F. Pierret, "Advanced Semiconductor Fundamentals," *Book*, vol. 121, no. 7, p. 221, 1987.

[90] L. Zhu, B. J. Richardson, and Q. Yu, "Controlled colloidal synthesis of iron pyrite FeS_2 nanorods and quasi-cubic nanocrystal agglomerates," *Nanoscale*, vol. 6, no. 2, pp. 1029–1037, 2014.

[91] J. Schneider, D. Bahnemann, J. Ye, G. Li Puma, and D. D. Dionysiou, Eds., *Photocatalysis*. Cambridge: Royal Society of Chemistry, 2016.

[92] G. M. Kontogeorgis, B. Maribo-Mogensen, and K. Thomsen, "The Debye-Hückel theory and its importance in modeling electrolyte solutions," *Fluid Phase Equilib.*, vol. 462, pp. 130–152, 2018.

[93] Z. Zhang and J. T. Yates, "Band Bending in Semiconductors: Chemical and Physical Consequences at Surfaces and Interfaces," *Chem. Rev.*, vol. 112, no. 10, pp. 5520–5551, 2012.

[94] P. Lianos, "Review of recent trends in photoelectrocatalytic conversion of solar energy to electricity and hydrogen," *Appl. Catal. B Environ.*, vol. 210, pp. 235–254, 2017.

[95] M. R. G. de Chialvo and A. C. Chialvo, "Hydrogen evolution reaction: Analysis of the Volmer-Heyrovsky-Tafel mechanism with a generalized adsorption model," *J. Electroanal. Chem.*, vol. 372, no. 1–2, pp. 209–223, 1994.

[96] P. F. Meilan and M. Garavaglia, "Rayleigh Resolution Criterion for Light Sources of Different Spectral Composition," *Brazilian J. Phys.*, vol. 27, no. 4, pp. 638–643, 1997.

[97] R. Erni, M. D. Rossell, C. Kisielowski, and U. Dahmen, "Atomic-Resolution Imaging with a Sub-50-pm Electron Probe," *Phys. Rev. Lett.*, vol. 102, no. 9, p. 096101, 2009.

[98] S. Zhou and L. Jiang, "Modern description of Rayleigh's criterion," *Phys. Rev. A*, vol. 99, no. 1, p. 013808, 2019.

[99] Y. Waseda, E. Matsubara, and K. Shinoda, *X-Ray Diffraction Crystallography*. Berlin, Heidelberg: Springer Berlin Heidelberg, 2011.

[100] R. Castaing, *Application of electron probes to local chemical and crystallographic analysis*. Pasadena CA: California Institute of Technology, 1955.

[101] J. Goldstein, D. E. Newbury, J. R. Michael, N. W. M. Ritchie, J. H. J. Scott, and D. C. Joy, *Scanning electron microscopy and x-ray microanalysis*., 2003.

[102] P. Lechner *et al.*, "Multichannel silicon drift detectors for x-ray spectroscopy,", vol. 4012, pp. 592–599, 2000.

[103] J. I. Goldstein *et al.*, *Scanning Electron Microscopy and X-ray Microanalysis*. Boston, MA: Springer US, 2003.

[104] M. Scimeca, S. Bischetti, H. K. Lamsira, R. Bonfiglio, and E. Bonanno, "Energy Dispersive X-ray (EDX) microanalysis: A powerful tool in biomedical research and diagnosis.," *Eur. J. Histochem.*, vol. 62, no. 1, p. 2841, 2018.

[105] Hyperphysics, "EDX characteristic x-ray spectrum.". Available: http://hyperphysics.phy-astr.gsu.edu/hbase/quantum/xrayc.html.

[106] L. A. Giannuzzi and F. A. Stevie, "A review of focused ion beam milling techniques for TEM specimen preparation," *Micron*, vol. 30, no. 3, pp. 197–204, 1999.

[107] J. A. Newman, P. D. Schmitt, S. J. Toth, F. Deng, S. Zhang, and G. J. Simpson, "Parts per Million Powder X-ray Diffraction.," *Anal. Chem.*, vol. 87, no. 21, pp. 10950–5, 2015.

[108] R. Smith, K. L. Wright, and L. Ashton, “Raman spectroscopy: an evolving technique for live cell studies,” *Analyst*, vol. 141, no. 12, pp. 3590–3600, 2016.

[109] C. G. Morales-Guio, S. David Tilley, H. Vrubel, M. Grätzel, and X. Hu, “ARTICLE Hydrogen evolution from a copper(I) oxide photocathode coated with an amorphous molybdenum sulphide catalyst,” 2014.

[110] K. J. Andersson, H. Ogasawara, D. Nordlund, G. E. Brown, and A. Nilsson, “Preparation, Structure, and Orientation of Pyrite FeS_2 {100} Surfaces: Anisotropy, Sulfur Monomers, Dimer Vacancies, and a Possible FeS Surface Phase,” *J. Phys. Chem. C*, vol. 118, no. 38, pp. 21896–21903, 2014.

[111] Y. Bi, Y. Yuan, C. L. Exstrom, S. A. Darveau, and J. Huang, “Air Stable, Photosensitive, Phase Pure Iron Pyrite Nanocrystal Thin Films for Photovoltaic Application,” *Nano Lett.*, vol. 11, no. 11, pp. 4953–4957, 2011.

[112] H. Qin, J. Jia, L. Lin, H. Ni, M. Wang, and L. Meng, “Pyrite FeS2 nanostructures: Synthesis, properties and applications,” *Mater. Sci. Eng. B*, vol. 236–237, pp. 104–124, 2018.

[113] B. J. Richardson, L. Zhu, and Q. Yu, “Inverted hybrid solar cells based on pyrite FeS2nanocrystals in P3HT:PCBM with enhanced photocurrent and air-stability,” *Sol. Energy Mater. Sol. Cells*, vol. 116, pp. 252–261, 2013.

[114] H. A. MacPherson and C. R. Stoldt, “Iron pyrite nanocubes: Size and shape considerations for photovoltaic application,” *ACS Nano*, vol. 6, no. 10, pp. 8940–8949, 2012.

[115] A. Douglas, R. Carter, L. Oakes, K. Share, A. P. Cohn, and C. L. Pint, “Ultrafine Iron Pyrite (FeS_2) Nanocrystals Improve Sodium–Sulfur and Lithium–Sulfur Conversion Reactions for Efficient Batteries,” *ACS Nano*, vol. 9, no. 11, pp. 11156–11165, 2015.

[116] J. M. Lucas *et al.*, “Ligand-Controlled Colloidal Synthesis and Electronic Structure Characterization of Cubic Iron Pyrite (FeS_2) Nanocrystals,” *Chem. Mater.*, vol. 25, no. 9, pp. 1615–1620, 2013.

[117] W. Li, M. Döblinger, A. Vaneski, A. L. Rogach, F. Jäckel, and J. Feldmann, “Pyrite nanocrystals: Shape-controlled synthesis and tunable optical properties via reversible self-assembly,” *J. Mater. Chem.*, vol. 21, no. 44, pp. 17946–17952, 2011.

[118] C. Wadia, Y. Wu, S. Gul, S. K. Volkman, J. Guo, and A. P. Alivisatos, “Surfactant-Assisted Hydrothermal Synthesis of Single phase Pyrite FeS_2 Nanocrystals,” *Chem. Mater.*, vol. 21, no. 13, pp. 2568–2570, 2009.

[119] S. Liu *et al.*, “Phase-pure iron pyrite nanocrystals for low-cost photodetectors,” *Nanoscale Res. Lett.*, vol. 9, no. 1, p. 549, 2014.

[120] S. Middya, A. Layek, A. Dey, and P. P. Ray, “Synthesis of nanocrystalline FeS2with increased band gap for solar energy harvesting,” *J. Mater. Sci. Technol.*, vol. 30, no. 8, pp. 770–775, 2014.

[121] T. S. Yoder *et al.*, “Iron pyrite nanocrystal inks: Solvothermal synthesis, digestive ripening, and reaction mechanism,” *Chem. Mater.*, vol. 26, no. 23, pp. 6741–6751, 2014.

[122] S. C. Hsiao *et al.*, “Facile synthesis and characterization of high temperature phase FeS2pyrite nanocrystals,” *Mater. Lett.*, vol. 75, pp. 152–154, 2012.

[123] N. E’jazi and M. Aghaziarati, “Determination of optimum condition to produce nanocrystalline pyrite by solvothermal synthesis method,” *Adv. Powder Technol.*, vol. 23, no. 3, pp. 352–357, 2012.

[124] J. Puthussery, S. Seefeld, N. Berry, M. Gibbs, and M. Law, “Colloidal Iron Pyrite (FeS 2) Nanocrystal Inks for Thin Film Photovoltaics,” *J. Am. Chem. Soc.*, vol. 133, no. 4, pp. 716-719, 2011.

[125] A. L. Patterson, “The Scherrer Formula for X-Ray Particle Size Determination,” *Phys. Rev.*, vol. 56, no. 10, pp. 978–982, 1939.

[126] H. Sharifi Dehsari, A. Halda Ribeiro, B. Ersöz, W. Tremel, G. Jakob, and K. Asadi, “Effect of precursor concentration on size evolution of iron oxide nanoparticles,” *CrystEngComm*, vol. 19, no. 44, pp. 6694–6702, 2017.

[127] J. Van Embden, A. S. R. Chesman, and J. J. Jasieniak, “The Heat-Up Synthesis of Colloidal Nanocrystals.”

[128] J. P. Wilcoxon, P. P. Newcomer, and G. A. Samara, “Strong Quantum Confinement Effects In Semiconductors: Fes_2 Nanoclusters,” Solid State Communication, 1996.

[129] M. P. Pileni, “Reverse micelles as microreactors,” *J. Phys. Chem.*, vol. 97, no. 27, pp. 6961–6973, 1993.

[130] M.-L. Wu, D.-H. Chen, and T.-C. Huang, “Synthesis of Au/Pd Bimetallic Nanoparticles in Reverse Micelles,” *Langmuir*, vol. 17, no. 13, pp. 3877–3883, 2001.

[131] “Sequential synthesis of core-shell nanoparticles using reverse micelles,” 2001.

[132] W. L. Zhou, E. E. Carpenter, J. Sims, A. Kumbhar, and C. J. O’Connor, “Transmission Electron Microscopy Study of Gold-Coated Iron Core-Shell and Au/Fe/Au Onion-Like Nanoparticles Synthesized using Reverse Micelles,” *MRS Proc.*, vol. 581, p. 107, 1999.

[133] S. A. Jadhav, “Self-assembled monolayers (SAMs) of carboxylic acids: An overview,” *Cent. Eur. J. Chem.*, vol. 9, no. 3, pp. 369–378, 2011.

[134] C. Yan, M. Zharnikov, A. Gölzhäuser, and M. Grunze, “Preparation and characterization of self-assembled monolayers on indium tin oxide,” *Langmuir*, vol. 16, no. 15, pp. 6208–6215, 2000.

[135] D. F. Garcia-Gutierrez, L. Patricia Hernandez-Casillas, M. V. Cappellari, F. Fungo, E. Martínez-Guerra, and D. Ixcoatl García-Gutiérrezgutiérrez, “Influence of the Capping Ligand on the Band Gap and Electronic Levels of PbS Nanoparticles through Surface Atomistic Arrangement Determination,” 2018.

[136] W. Jaegermann and H. Tributsch, “Photoelectrochemicai reactions of FeS2 (pyrite) with t120 and reducing agents,” 1983.

[137] M. Descostes, F. Mercier, N. Thromat, C. Beaucaire, and M. Gautier-Soyer, “Use of XPS in the determination of chemical environment and oxidation state of iron and sulfur samples: constitution of a data basis in binding energies for Fe and S reference compounds and applications to the evidence of surface species of an oxidized py,”

Appl. Surf. Sci., vol. 165, no. 4, pp. 288–302, 2000.

[138] X. Zhang *et al.*, "Phase Stability and Stoichiometry in Thin Film Iron Pyrite: Impact on Electronic Transport Properties," 2015.

[139] H. W. Nesbitt, "Sulfur and iron surface states on fractured pyrite surfaces," *Am. Mineral.*, vol. 83, no. 9–10, pp. 1067–1076, 1998.

[140] N. Alonso-Vante, G. Chatzitheodorou, S. Fiechter, N. Mgoduka, I. Poulios, and H. Tributsch, "Interfacial behavior of hydrogen-treated sulphur deficient pyrite (FeS2-x)," *Sol. Energy Mater.*, vol. 18, no. 1–2, pp. 9–21, 1988.

[141] J. P. R. de Villiers and D. C. Liles, "The crystal-structure and vacancy distribution in 6C pyrrhotite," *Am. Mineral.*, vol. 95, no. 1, pp. 148–152, 2010.

[142] G. Pimenta and W. Kautek, "Pyrite film formation by H2S reactive annealing of iron," 1994.

[143] K. J. Andersson, H. Ogasawara, D. Nordlund, G. E. Brown, and A. Nilsson, "Preparation, Structure, and Orientation of Pyrite FeS_2 {100} Surfaces: Anisotropy, Sulfur Monomers, Dimer Vacancies, and a Possible FeS Surface Phase," *J. Phys. Chem. C*, vol. 118, no. 38, pp. 21896–21903, 2014.

[144] Y.-J. Lin, W.-Y. Chou, S.-T. Lin, C.-F. You, and C.-L. Tsai, "Effects of Sulfide Treatment of Indium Tin Oxide on Efficiency of Polymer Light-Emitting Diodes," *Jpn. J. Appl. Phys.*, vol. 46, no. 2, pp. 647–650, 2007.

[145] J. A. Leiro, S. S. Mattila, and K. Laajalehto, "XPS study of the sulphur 2p spectra of pyrite," *Surf. Sci.*, vol. 547, no. 1–2, pp. 157–161, 2003.

[146] S. Mattila, J. A. Leiro, and M. Heinonen, "XPS study of the oxidized pyrite surface," *Surf. Sci.*, vol. 566–568, no. 1–3 PART 2, pp. 1097–1101, 2004.

[147] R. Nyholm and N. Mbrtensson, "Core level binding energies for the elements Zr-Te (2 = 40-52)," 1980.

[148] G. E. McGUIRE, G. K. Schweitzer, and and A. Thomas Carlson, "Study of Core Electron Binding Energies in Some Group Ilia, Vb, and VIb Compounds 1," 1973.

[149] C. Webb and M. Lichtensteiger, "Characterization of oxidized CdS by SIMS/XPS," *J. Electron Spectros. Relat. Phenomena*, vol. 41, no. 1, pp. 125–144, 1986.

[150] A. G. Scheuermann and P. C. McIntyre, "Atomic Layer Deposited Corrosion Protection: A Path to Stable and Efficient Photoelectrochemical Cells," *J. Phys. Chem. Lett.*, vol. 7, no. 14, pp. 2867–2878, 2016.

[151] D. Bae *et al.*, "Protection of Si photocathode using TiO2deposited by high power impulse magnetron sputtering for H2evolution in alkaline media," *Sol. Energy Mater. Sol. Cells*, vol. 144, pp. 758–765, 2016.

[152] A. Paracchino, N. Mathews, T. Hisatomi, M. Stefik, S. D. Tilley, and M. Grätzel, "Ultrathin films on copper(i) oxide water splitting photocathodes: a study on performance and stability," *Energy Environ. Sci.*, vol. 5, no. 9, p. 8673, 2012.

[153] X. Yang, R. Liu, C. Du, P. Dai, Z. Zheng, and D. Wang, "Improving Hematite-based Photoelectrochemical Water Splitting with Ultrathin TiO_2 by Atomic Layer

Deposition," *ACS Appl. Mater. Interfaces*, vol. 6, no. 15, pp. 12005–12011, 2014.

[154] N. L. Sukiman *et al.*, "Durability and Corrosion of Aluminium and Its Alloys: Overview, Property Space, Techniques and Developments," *Alum. Alloy. - New Trends Fabr. Appl.*, pp. 47–97, 2012.

[155] C. Steinhagen, T. B. Harvey, C. J. Stolle, J. Harris, and B. A. Korgel, "Pyrite nanocrystal solar cells: Promising, or fool's gold?," *J. Phys. Chem. Lett.*, vol. 3, no. 17, pp. 2352–2356, 2012.

[156] S. Shukla *et al.*, "Origin of Photocarrier Losses in Iron Pyrite (FeS2) Nanocubes," *ACS Nano*, vol. 10, no. 4, pp. 4431–4440, 2016.

[157] F. W. Herbert, A. Krishnamoorthy, K. J. Van Vliet, and B. Yildiz, "Quantification of electronic band gap and surface states on FeS2(100)," *Surf. Sci.*, vol. 618, pp. 53–61, 2013.

[158] J. Hu, Y. Zhang, M. Law, and R. Wu, "First-principles studies of the electronic properties of native and substitutional anionic defects in bulk iron pyrite," *Phys. Rev. B - Condens. Matter Mater. Phys.*, vol. 85, no. 8, pp. 1–10, 2012.

[159] J. Hu, Y. Zhang, M. Law, and R. Wu, "Increasing the band gap of iron pyrite by alloying with oxygen," *J. Am. Chem. Soc.*, vol. 134, no. 32, pp. 13216–13219, 2012.

[160] H. Vogt, T. Chattopadhyay, and H. J. Stolz, "Complete first-order Raman spectra of the pyrite structure compounds FeS2, MnS2AND SiP2," *J. Phys. Chem. Solids*, vol. 44, no. 9, pp. 869–873, 1983.

[161] C. Rémazeilles *et al.*, "Microbiologically influenced corrosion of archaeological artefacts:Characterisation of iron(II) sulfides by Raman spectroscopy," *J. Raman Spectrosc.*, vol. 41, no. 11, pp. 1425–1433, 2010.

[162] B. Yuan, W. Luan, S.-T. Tu, and J. Wu, "One-step synthesis of pure pyrite FeS 2 with different morphologies in water," *New J. Chem*, vol. 39, p. 3571, 2015.

[163] Y. Yang, D. Xu, Q. Wu, and P. Diao, "Cu2O/CuO Bilayered Composite as a High-Efficiency Photocathode for Photoelectrochemical Hydrogen Evolution Reaction," *Sci. Rep.*, vol. 6, no. 1, p. 35158, 2016.

[164] C.-Y. Lin, Y.-H. Lai, D. Mersch, and E. Reisner, "Cu2O|NiOx nanocomposite as an inexpensive photocathode in photoelectrochemical water splitting," *Chem. Sci.*, vol. 3, no. 12, p. 3482, 2012.

[165] S. Li, P. Zhang, X. Song, and L. Gao, "Photoelectrochemical Hydrogen Production of TiO $_2$ Passivated Pt/Si-Nanowire Composite Photocathode," *ACS Appl. Mater. Interfaces*, vol. 7, no. 33, pp. 18560–18565, 2015.

[166] A. Walsh *et al.*, "Ternary cobalt spinel oxides for solar driven hydrogen production: Theory and experiment," *Energy Environ. Sci.*, vol. 2, no. 7, pp. 774–782, 2009.

[167] J. C. Moore and C. V. Thompson, "A phenomenological model for the photocurrent transient relaxation observed in ZnO-based photodetector devices," *Sensors (Switzerland)*, vol. 13, no. 8, pp. 9921–9940, 2013.

[168] Y. Xin, Z. Li, W. Wu, B. Fu, and Z. Zhang, "Pyrite FeS $_2$ Sensitized TiO $_2$ Nanotube

Photoanode for Boosting Near-Infrared Light Photoelectrochemical Water Splitting," *ACS Sustain. Chem. Eng.*, vol. 4, no. 12, pp. 6659–6667, 2016.

[169] J. Hu, Y. Zhang, M. Law, and R. Wu, "Increasing the Band Gap of Iron Pyrite by Alloying with Oxygen," *J. Am. Chem. Soc.*, vol. 134, no. 32, pp. 13216–13219, 2012.

[170] J. Lu *et al.*, "Atomic healing of defects in transition metal dichalcogenides," *Nano Lett.*, vol. 15, no. 5, pp. 3524–3532, 2015.

[171] L.-J. Guo, J.-W. Luo, T. He, S.-H. Wei, and S.-S. Li, "Photocorrosion-limited maximum efficiency of solar photoelectrochemical water splitting," 2018.

[172] "Pourbaix Diagram Iron." Available: https://www.ambrasta.com/pourbaix-diagram-iron/

[173] Sigma-Aldrich, "Quantum Dots". Avaiable: https://www.sigmaaldrich.com/technical-documents/articles/materials-science/nanomaterials/quantum-dots.html

[174] A. Ausili, M. Sánchez, and J. C. Gómez-Fernández, "Attenuated total reflectance infrared spectroscopy: A powerful method for the simultaneous study of structure and spatial orientation of lipids and membrane proteins," *Biomed. Spectrosc. Imaging*, vol. 4, no. 2, pp. 159–170, 2015.

[175] D. Shishin, E. Jak, and S. A. Decterov, "Critical Assessment and Thermodynamic Modeling of the Fe-O-S System," *J. Phase Equilibria Diffus.*, vol. 36, no. 3, pp. 224–240, 2015.